

Complexity Reduction In Multiple Input Multiple Output Algorithms

Leon Gor, BE (Hons 1)

Submitted in fulfillment of the requirements for the
degree of
Doctor of Philosophy



March 2007

Thesis supervisor Prof. Michael Faulkner

Centre for Telecommunications and Microelectronics
Victoria University, Footscray Park Campus
P.O. BOX 14428 MCMC
Melbourne 8001
Australia

Declaration

I hereby declare the contents of this thesis are the results of original research and have not been submitted for a higher degree to any other university or institution. The research work presented in this thesis is carried out by me and to the best of my knowledge does not contain any previously published or written works by another person except where due reference is made in the text.

Leon Gor _____

Abstract

Wireless communication devices are currently enjoying increasing popularity and widespread use. The constantly growing number of users, however, results in the shortage of the available spectrum. Various techniques have been proposed to increase the spectrum efficiency of wireless systems to solve the problem. Multiple Input Multiple Output (MIMO) is one solution that employs multiple antennas at the transmitter and receiver. The MIMO algorithms are usually highly complex and computationally intensive. This results in increased power consumption and reduced battery lifespan. This thesis investigates the complexity – performance trade-off of two MIMO algorithms.

Space Time Block Coding (STBC) is a MIMO-based algorithm, which efficiently exploits spatial and temporal diversity. Recently, it has been specified in a number of 3G standards. However, not much attention has been paid to the implementation issues of this algorithm. One such issue, clipping of the Analog to Digital Converter (ADC) at the receiver, is described in the first part of the thesis (chapter 3). A small amount of clipping in an ADC can improve dynamic range and reduce the power consumption. However, the increased clipping distortion of the signal, can adversely affect the overall performance of the system. It will be shown in this dissertation that STBC are more sensitive to clipping, compared to the uncoded single antenna systems. Two receiver structures are considered: Direct Conversion (DC) structure, where the ADCs impose a

square clipping function, and a Log-Polar structure, where ADC induces a circular clipping function. Log-Polar receivers were found to be clipping insensitive for the given target Symbol Error Rate (SER) of $1 \cdot 10^{-3}$. This makes Log-Polar receivers an obvious choice for the system designers.

The second part of the thesis (chapter 4) addresses the complexity problem associated with the QR decomposition algorithm, which is frequently used as a faster alternative to channel inversion in a MIMO scheme. Channel tracking can be employed with QR equalization in order to reduce the pilot overhead of a MIMO system in a non-stationary environment. QR decomposition is part of the QR equalization method and has to be performed in every instance that the channel estimate is obtained. The high rate of the QR decomposition, a computationally intensive technique, results in a high computational complexity per symbol. Some novel modifications are proposed to address this problem. Reducing the repetition rate of QR decompositions and tracking R (the upper triangular matrix) directly, while holding unitary matrix Q fixed, can significantly reduce complexity per symbol at the expense of some introduced error. Additional modification of the CORDIC algorithm (a square root- and division-free algorithm used to perform QR decomposition) results in more than 80% of computational complexity savings.

Further, Minimum Mean Squared Error (MMSE) detection is applied to Least Mean Squared (LMS) based R tracking and channel tracking algorithms and then compared in complexity and performance to the Recursive Least Squares Decision Feedback Equalizer (RLS-DFE) tracking system in [1]. The R tracking scheme is shown to achieve more accurate channel estimates compared to the channel tracking scenario, but this advantage does not translate into better Bit Error Rate (BER) results due to errors on the first layer of the detector. Both LMS strategies have an inferior BER performance compared to the DFE RLS-based system of [1], and surprisingly the LMS schemes show no significant complexity improvement.

Foreword

The contents of this thesis are the results of original research and have not been submitted for a higher degree to any other university or institution. This thesis investigates the complexity issues of techniques that use the Multiple Input Multiple Output (MIMO) approach. Two major works are described in the thesis. Chapter 3 investigates the effect of clipping induced by the limited dynamic range of the receiver Analog to Digital Converter (ADC) on the Space Time Block (STBC) system. The novelty of this work highlights how physical implementation issues affect the performance of the well-known and popular Alamouti STBC algorithm. The results of this work were published in two papers

- L. Gor and M. Faulkner, "Effect of Soft Limiting in the Transmit Diversity Schemes Employing Space Time Block Coding," *The fourth international conference on modelling and simulation, Melbourne, Australia, 2002*
- L. Gor and M. Faulkner, "A/D clipping effects on STBC scheme in receivers employing direct conversion structure," *Electronics Letters* vol. 40, pp. 352-354, 2004.

In QR detection receivers that employ channel tracking, the QR decomposition operation results in a high complexity per symbol. This issue is investigated in chapter 4. The innovative

aspect of this work lies in three modifications proposed to reduce the complexity. The results are submitted for publications in

- L. Gor and M. Faulkner, "Power reduction through upper triangular matrix tracking in QR detection MIMO receivers," *Vehicular Technology Conference (VTC)*, 2006.
- L. Gor and M. Faulkner, "Channel tracking for MIMO receivers," **Applicant:** Australian Telecommunications Research Centre (ATCRC), **Patent number:** 2005905387, **Filed:** 29 September 2005

Acknowledgements

I would like to thank Prof. Mike Faulkner for his support and encouragement during these four years of hard and interesting work. His undying inspiration and motivation has helped me through the ups and downs of the rough terrain of the research path. I would also like to thank my friends and colleagues whose valuable advice has helped me on many occasions during these interesting times. My special thanks go to Aaron Reid, coding and information theory guru, for his valuable insights and comments on this thesis. And last but not least, my parents and close relatives who gave me a moral and emotional support during the toughest times, when I felt like quitting.

Contents

1	INTRODUCTION AND THESIS OUTLINE	1
2	BACKGROUND INFORMATION	3
2.1	Propagation Characteristics of a Radio Channel	3
2.1.1	Large-scale path loss	4
2.1.2	Small-scale variations	5
2.2	Diversity	8
2.2.1	Spatial diversity	8
2.2.2	Polarisation diversity	9
2.2.3	Time diversity	9
2.2.4	Frequency diversity	9
2.3	Concept of Information	9
2.4	Channel Capacity	10
2.5	Multiple Input Multiple Output Systems	11
2.5.1	Capacity of the Multiple Input Multiple Output system	11
2.5.2	Using MIMO capacity	13
3	SIMULATION-BASED CLIPPING ANALYSIS IN ALAMOUTI SPACE TIME BLOCK CODES	16
3.1	Chapter Outline	16
3.2	Introduction	17
3.2.1	Communication system based on STBC coding	17
3.2.2	Receiver architectures	20
3.2.3	Signal conversion	23
3.3	Clipping in SISO systems	24
3.3.1	DC receivers and square clipping	24

3.3.2	Log-Polar receivers and circular clipping	26
3.4	Clipping in Alamouti STBC Coded System	28
3.4.1	Square clipping.....	28
3.4.2	Circular clipping.....	30
3.5	Simulations and Comparisons.....	31
3.6	Conclusions	33
4	COMPLEXITY REDUCTION THROUGH UPPER TRIANGULAR MATRIX TRACKING IN QR DETECTION MIMO RECEIVERS	35
4.1	Chapter Outline	35
4.2	Introduction	36
4.2.1	IEEE 802.11 TGn channel model.....	36
4.2.2	Detection in MIMO	39
4.2.3	Review of existing MIMO channel-tracking schemes	45
4.3	Using Upper Triangular Matrix Tracking to Reduce Complexity per Symbol in a Linear ZF MIMO System	53
4.3.1	System model	53
4.3.2	Evaluation of tracking schemes.....	56
4.3.3	Saving power through QR decomposition repetition rate reduction	64
4.3.4	Threshold detection in a practical system.....	68
4.3.5	CORDIC-based QR decomposition.....	73
4.3.6	Simulation results	82
4.4	Evaluation of the two proposed strategies with VBLAST-MMSE detection and comparison with RLS based DFE scheme.....	86
4.4.1	Introduction	86
4.4.2	Evaluation of tracking schemes.....	87
4.5	Conclusions	98
5	CONCLUSIONS.....	100
5.1	Future work	102

List of Figures

Figure 1.	Multipath effect.....	5
Figure 2.	MIMO system employing multiple antennas at the receiver and transmitter	12
Figure 3.	Space Time Coded MIMO system setup	14
Figure 4.	Spatial Multiplexing system structure	15
Figure 5.	Simplified setup for 2X1 communication system based on STBC coding.....	17
Figure 6.	STBC coded system implementation based on DC receiver structure	20
Figure 7.	Block diagram of the Log-Polar receiver	21
Figure 8.	ADC broken down into a sampler and quantiser	23
Figure 9.	A conceptual example of the square clipping of a QPSK modulated signal	25
Figure 10.	Soft limiting operation of ADC in a DC receiver	25
Figure 11.	Magnitude clipping in a Log-Polar receiver employing QPSK modulation.....	27
Figure 12.	Soft limiting operation of the ADC in a Log-Polar receiver	27
Figure 13.	Simulation block diagram.....	31
Figure 14.	Lowest clip/average levels for 10^{-3} target SER, square clipping	31
Figure 15.	Sensitivity of STBC coded and SISO schemes to AWGN at 10^{-3} target SER.	33
Figure 16.	(a) Doppler spectrums used in 802.11n and Clarke's models (b) 40km/h moving object causes peak at 194 Hz. $f_c=5.25\text{GHz}$	38
Figure 17.	BER comparison, 4X4 system with channel known at the receiver and QPSK modulation.	43
Figure 18.	A generic frame structure consisting of a training preamble and D payload data symbols	45
Figure 19.	Channel MSE vs Time (symbols after training). Doppler as for 802.11n channels. The symbol period is $4\mu\text{s}$	47

Figure 20.	Autocorrelation of the channel and channel inverse for SISO, 2X2 MIMO and 4X4 MIMO channels	49
Figure 21.	MIMO-OFDM structure with QR detection and channel tracking, initial channel estimates are obtained during the training session.....	53
Figure 22.	General packet structure employed in wireless LANs.....	54
Figure 23.	Decision-directed tracking and QR decomposition for the channel-tracking case.....	56
Figure 24.	An example of the indexing, QRD performed every 3 rd symbol.....	57
Figure 25.	Decision-directed tracking and QR decomposition for the upper triangular matrix-tracking scenario	58
Figure 26.	LMS configuration for tracking the A_R matrix.....	60
Figure 27.	Comparison of tracking performance, perfect channel estimation and hence perfect Q and R is assumed at the first symbol.....	62
Figure 28.	The system model used to evaluate the channel or upper triangular matrix-tracking schemes	65
Figure 29.	MSE vs. packet length comparison of various scenarios in the presence of AWGN and $f_d=6\text{Hz}$	67
Figure 30.	Threshold detector block diagram	71
Figure 31.	MSE vs. packet length comparison using threshold detector	72
Figure 32.	Using CORDIC to obtain upper triangular matrix R and unitary Q of a 2X2 complex matrix.	75
Figure 33.	(a) Conventional CORDIC with three micro-rotations. The micro-rotation angle is approximately halved for each consecutive iteration (b) CORDIC becomes inefficient when the input angle is small.....	78
Figure 34.	Reducing number of micro-rotations to one, by considering all possible micro-rotations at each iteration.....	78
Figure 35.	The number of microrotations vs $\frac{y}{x}$ ($= \tan(\alpha)$). Zero corresponds to $\alpha= 0$ degrees and 1 corresponds to $\alpha= 45$ degrees.	81
Figure 36.	Complexity savings of the A_R tracking with modified CORDIC over the H tracking with the conventional CORDIC in 2X2 system.....	84
Figure 37.	Decision-directed tracking and Sorted QR decomposition (SQRD))for the channel-tracking case.	88

Figure 38.	Decision-directed tracking and SQRD for the upper triangular matrix-tracking scenario	90
Figure 39.	Complexity per symbol vs QR (order) update time.....	93
Figure 40.	BER comparison for the stationary channel	95
Figure 41.	Channel MSE for A_R and H tracking strategies, SNR=20dB, $fdT=1 * 10^{-3}$	96
Figure 42.	A_R and H tracking BER results, as well as the BER result from [1], SNR=20dB, $fdT=1 * 10^{-3}$	97

List of Acronyms

Acronym	Description	First used in section
ADC	Analog to Digital Converter	3.2.1
AGC	Automatic Gain Control	3.2.2.1
AWGN	Additive White Gaussian Noise	2.4
DC	Direct Conversion	3.2.1
DFE	Decision Feedback Equalizer	4.2.3.2
FFF	Feed Forward Filter	4.2.3.2
FBF	Feed Back Filter	4.2.3.2
iid	independent identically distributed	2.5.1
ISI	Inter Symbol Interference	2.1.2.3
MIMO	Multiple Input Multiple Output	2.5.1
MMSE	Minimum Mean Squared Error	4.2.2.1
MLSD	Maximum Likelihood Sequence Detection	4.2.2
OFDM	Orthogonal Frequency Division Multiplexing	2.1.2.3
SER	Symbol Error Rate	3.1
SIC	Successive Interference Cancellation	2.5.2.1
SISO	Single Input Single Output	1
SNR	Signal to Noise Ratio	2.2.1
SQRD		4.2.2.3
STBC	Space Time Block Coding	1
STC	Space Time Coding	2.5.2.1
STTC	Space Time Trellis Coding	2.5.2.1
VBLAST		4.2.2.2
VGA	Variable Gain Amplifier	3.2.2.1
WLAN	Wireless Local Area Network	4.3.1
ZF	Zero Forcing	2.5.2.1

List of principal symbols

Symbol	Description	First used in section
$\overline{L_p}$	Path loss	2.1.1
$f_d T$	Normalized Doppler frequency	2.1.2.2
M	Number of receive antennas	2.5.1
N	Number of transmit antennas	2.5.1
σ_ε^2	Quantization noise power	3.2.3
\mathbf{A}_R	Nearly upper triangular matrix	4.3
B_c	Coherence Bandwidth	2.1.2.1
C	Channel capacity	2.4
$C_{n \times n}$	n x n matrix total complexity to perform QR decomposition	4.3.5.5
C_R	Complexity of CORDIC in the rotational mode	4.3.5.5
C_V	Complexity of CORDIC in the vectoring mode	4.3.5.5
D	Dynamic range of Analog to Digital Converter	3.2.3
\mathbf{er}_H	Channel error matrix	4.3.2.1
\mathbf{er}_R	Upper triangular matrix error	4.3.2.2
f_d	Doppler frequency	2.1.2.2
H(X)	Entropy of the distribution of random variable X	2.4
\mathbf{H}	The channel matrix	2.5.1
h_i	Complex channel element	3.2.1
M_x, M_y	Mantissas of binary numbers x and y	4.3.5.4
n	Complex Additive White Gaussian noise sample/vector	3.2.1

Symbol	Description	First used in section
q	Quantization step size	3.2.3
\mathbf{Q}	Unitary matrix	4.3.1
\mathbf{q}_m	CORDIC orthogonal matrix	4.3.5.1
r	Received clipped signal element	3.3.1
\mathbf{R}	Upper triangular matrix	4.3.1
\mathbf{S}	Orthogonal coding matrix	3.2.1
s	Transmitted symbol/vector	3.2.1
$S(f)$	Doppler spectrum of 802.11n channel	4.2.1
T_c	Coherence time	2.1.2.2
V_F	Full scale range of Analog to Digital Converter	3.2.3
\mathbf{y}	Received signal/vector	3.2.1
α	Scaling coefficient	3.3.1
\mathbf{T}	Possible transmitted signal vector for ML detection	4.2.2
θ	Constellation size	4.2.2
$\mathcal{G}(\cdot)$	Hard decision operator	4.2.2.1
\mathbf{A}	Linear mapping	4.2.2.1
σ_n^2	AWGN variance	4.2.2.1
\mathbf{P}	Symbol error covariance matrix	4.2.2.1
\mathbf{H}	Extended channel matrix	4.4.1
C_H	Complexity of the channel-tracking system	4.4.2.1
C_R	Complexity of the upper triangular matrix-tracking system	4.4.2.2

1 Introduction and Thesis Outline

Wireless systems of the future must accommodate rich information content applications like high-speed Internet, live video streaming, online gaming, and so forth. The demand for these capabilities is constantly growing; in fact, according to [2] there will be 300,000 wireless hotspots by the end of 2009. Sophisticated algorithms based on Multiple Input Multiple Output (MIMO) techniques were developed to realise this great information capacity demand. These are usually highly complex, high processing power algorithms. Handheld, battery-operated devices are the primary targets of these new technologies. The increased power consumption will shorten battery life, hence the problem of reducing the processing power of these algorithms or their complexity is of paramount importance. This dissertation investigates the power and complexity issues of some of these algorithms.

The thesis is organised as follows. Chapter 2 presents all the necessary background information. The notion of channels and all the essential channel characteristics like multipath propagation and the Doppler effect are introduced. Concepts of diversity and information capacity are presented and the basic MIMO structure is reviewed. Coding to achieve diversity and Spatial Multiplexing are overviewed, which are essentially two major implementation approaches used to obtain the high capacity promised by information theory.

Alamouti Space Time Block (STBC) [3] is a popular algorithm aimed at achieving the diversity potential that MIMO offers. Implementation issues of the algorithm have attracted little attention in the literature. Chapter 3 investigates one such issue—that of signal clipping caused by the receiver's Analog to Digital Converter. The chapter first introduces STBC, then reviews the two adopted receiver hardware architectures:

1. Direct Conversion receiver that causes square clipping
2. Log-Polar receiver that induces a circular clipping

ADC clipping and quantisation effects are introduced next. The rest of the chapter compares the effect of the square and circular clipping on the STBC system and Single Input Single Output (SISO) systems in terms of performance deterioration and sensitivity.

QR equalisation techniques are often used as a quicker alternative to the matrix inversion. This technique is often employed in MIMO receivers where symbol detection involves channel matrix inversion. However, when channel tracking is employed to decrease training overheads and increase data throughput, QR decomposition (part of the QR equalisation scheme) of the channel matrix estimate is performed in every consecutive time slot. Since performing the QR decomposition is a computationally intensive process, detection will suffer a high computational complexity per symbol. The introductory part of Chapter 4 discusses the outlined problem, introduces the system model and briefly overviews the channel model used for the simulations. The remainder of the chapter proposes several novel modifications to decrease this computational burden while benefiting from channel tracking and QR equalisation.

2 Background Information

This chapter provides the necessary background information for the remaining parts of the thesis. Section 2.1 defines the propagation characteristics of the wireless channel and elaborates on the large-scale path loss and small-scale variations that cause signal fading, which include multipath and Doppler effects. Diversity, an important technique that exploits channel fading to increase the reliability of the signal, is presented in section 2.3. Section 2.4 introduces the concept of information as a measurable quantity and defines channel capacity. Finally, the last section describes the idea of Multiple Input Multiple Output (MIMO) systems and their advantages.

2.1 Propagation Characteristics of a Radio Channel

Wireless communications systems use electromagnetic waves to carry information signals from a sender to a recipient. They propagate through a space with various obstacles that are either moving or stationary and have different absorption or reflection properties. The Propagation medium can also vary in temperature, humidity, and so on. The propagation path between the sender and recipient including all the above factors is called a channel. A typical channel attenuates the signal and shifts its phase in a random manner. This effect can result in the loss of the information at the receiving side. Therefore it is important to identify the channel characteristics and take them into account when designing a communications system. The effect of the channel on the transmitted signal can be described by two major phenomena: Large-scale path loss and small-scale variations.

Large-scale path loss describes the loss of the signal strength over large distances, while fluctuations of the signal strength over small distances are characterised by small-scale variations. A detailed explanation of the two phenomena is now presented.

2.1.1 Large-scale path loss

Path loss is defined as the average loss of the received signal power at a given distance from the transmitter [4]. The average power loss is exponential with distance with its most basic representation [4]

$$\overline{L_p}[dB] = \overline{L_p}(d_0) + 10 * n * \log\left(\frac{d}{d_0}\right) \quad (1)$$

Here $\overline{L_p}(d_0)$ is the average path loss at the close-in reference distance d_0 and d is the distance between transmitter and receiver. The value exponent constant n depends on the environment. It is 2 for the free space and can go up to 6 when the receiver is inside the building with no line of sight path [5]. The path loss can vary considerably for different environments (i.e. different obstacles), with the same distance separation between transmitter and receiver. Equation (1) has to be modified to account for these random variations

$$L_p[dB] = \overline{L_p}(d_0) + 10 * n * \log\left(\frac{d}{d_0}\right) + X_\sigma \quad (2)$$

$L_p[dB]$ is a log-normal shadow path loss with distribution $X_\sigma \square N(0, \sigma^2)$. Essentially a log normal distribution statistically describes an ensemble of all possible propagation paths over the same distance.

2.1.2 Small-scale variations

Obstacles in the propagation environment can act as scatterers for the transmitted signal. They enable more than one path from the transmitter to the receiver, creating a multipath effect as shown in figure 1.

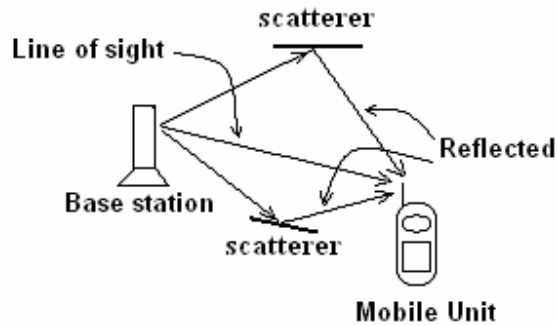


Figure 1. Multipath effect

Essentially multiple delayed copies of the same transmitted data (two reflected rays in figure) appear at the receiver. Also the amount of scatterers and their position generally changes randomly with time. The random movement of the transmitter, receiver or scatterers towards or away from each other creates a Doppler effect, causing the spectral components of the signal on various paths to shift their frequencies. This effect creates a spectral broadening. Multipath and Doppler are the major causes of signal distortion over small distances (due to the short wavelengths of the carrier frequency) [4]. The variations in the signal amplitude and phase are termed small-scale signal variations.

2.1.2.1 *Multipath effect*

The addition of the multiple copies of the transmitted waveform at the receiver can be either constructive or destructive, depending on the phase of each waveform. When destructive addition occurs it causes signal fading (the strength of the received signal is reduced).

Power delay profile [5] characterises a multipath channel. It shows the statistically averaged spread of the transmitted energy over different paths. Root Mean Squared (RMS) delay spread σ_τ describes the variations of the delay around its mean value. If the symbol time is much longer than σ_τ , (all the copies can be assumed to have equal delays), the channel will attenuate all the frequencies, equally resulting in a flat fading. However a symbol time shorter than σ_τ will result in a frequency-selective fading. Coherence bandwidth [5] is an equivalent parameter in the frequency domain. It is defined as

$$B_c \approx \frac{1}{50 * \sigma_\tau} \quad (3)$$

2.1.2.2 Doppler effect

A relative movement between a transmitter, scatterers and a receiver creates a Doppler effect. The receiver sees a positive shift in frequency when it moves towards the transmitter or a negative shift when it moves away from the transmitter. The frequency shift is defined as [4]

$$f_d = \frac{v}{\lambda} * \cos(\theta). \quad (4)$$

Here v is a positive or negative speed of the receiver relative to the stationary transmitter, λ is a carrier wavelength and the multiplication by $\cos(\theta)$ ensures that only the velocity component in the direction towards or away from the transmitter is taken. When the Doppler frequency is high the channel changes more quickly, hence fading will occur more often. Quite often it is convenient to express Doppler frequency relative to the symbol time

$$F_d T = f_d * T_s = \frac{f_d}{f_s} \quad (5)$$

T_s is a symbol time period and f_s is its reciprocal in the frequency domain. High values of $F_d T$ mean that the channel changes faster with more fades relative to the symbol time, which results in a higher symbol distortion. Coherence time T_c specifies the timeframe within which the channel impulse response is statistically time invariant [5],

$$T_c = \sqrt{\frac{9}{16 * \pi * f_d^2}} \quad (6)$$

where f_d is defined as a maximum Doppler shift.

There is a high probability that the channel will affect two symbols in totally different ways, if the time separation between the two adjacent data symbols is greater than T_c .

2.1.2.3 *Fading characteristics of the channel*

Multipath and Doppler shift affect the channel independently. The fading itself is a direct result of multipath, while the rate of fading depends on the Doppler effect. The channel is usually one of four types:

- Flat and slow fading
- Flat and fast fading
- Frequency selective and slow fading
- Frequency selective and fast fading

The channel between a stationary transmitter such as a base station and a fast-moving car or a train, for instance, exhibits fast fading properties due to the high Doppler shifts. On the other hand, offices and homes have stationary environments, resulting in time-invariant or very slow fading

channels. Wideband or frequency-selective channels cause Inter-Symbol-Interference (ISI) when the bandwidth of the information-carrying waveform exceeds Coherence Bandwidth B_c [6]. Then there is a situation when multipath components contain more than one symbol. It leads to the decision errors at the receiver after the addition of all these paths. There are various techniques that combat ISI by equalising channel response at the receiver [6]. Others, like Orthogonal Frequency Division Multiplexing (OFDM), avoid ISI by extending the data symbol with the guard interval [4] to ensure that all the delayed copies of the signal arrive within the time slot of the symbol.

2.2 Diversity

Diversity is obtained when the signal is sent along two or more statistically independent paths. If the signal along one path undergoes deep fading, there is a high probability that the signal along the other path may have a recoverable signal. The receiver then can choose either to take the strongest signal or to combine all the signals. Diversity can be exploited in space, polarisation, time or frequency domains.

2.2.1 Spatial diversity

Spatial diversity is obtained when two or more antennas are used at the receiver (receive diversity), transmitter (transmit diversity), or both. These techniques utilise the fact that if two antennas are separated by more than half a wavelength, small-scale fading affects the emitted or received signals independently [7]. The classical example of the receive diversity is a technique called maximum ratio combining [4]. Here received signals from all the paths are co-phased and then added. This ensures that the total received Signal to Noise Ratio (SNR) is higher than the SNR from each separate antenna.

2.2.2 Polarisation diversity

Electromagnetic waves travel along two orthogonal vertical and horizontal planes that can be used to obtain polarisation diversity [4]. This kind of diversity is preferred at the mobile unit, where it is unfeasible to deploy more than one antenna due to the lack of space. Polarisation diversity does not require physical separation of the antennas.

2.2.3 Time diversity

Time diversity [4] uses a repeatedly transmitted signal over the time slots that have separation longer than the coherence time of the channel. This ensures that repeated signals will undergo independent fading. This technique works well in fast fading environments but is harder to implement in a slow fading environment, where long delays have to be accommodated to establish independent fading of recurrent signals.

2.2.4 Frequency diversity

Here the same signal is transmitted on two or more frequencies whose separation is more than a coherence bandwidth of the channel. The channel then affects independently these signals in the frequency domain. OFDM can use a frequency diversity of a wideband channel with error correcting coding across independent sub-carriers to recover the symbols even if some of the sub-carriers undergo a deep fading [8].

2.3 Concept of Information

Entropy [9] describes the average information (or the amount of uncertainty) in a random variable. For a given random variable X , whose event space is spanned by the set of mutually exclusive events $[p_1, p_2, \dots, p_n]$, the entropy $H(X)$ is given by

$$H(X) = -\sum_{i=1}^n \log(p_i) * p_i \quad (7)$$

If $\log(p_i)$ has a base of two, then the information contained in X is defined in bits. $H(X)$ is a convex with the maximum occurring when all the mutually exclusive events have equal probability [9].

Conditional entropy can be interpreted as the amount of uncertainty in a random variable given the knowledge of the other random variable. If two random variables are dependent then knowledge of one of them will reduce the entropy of another one. For the two random variables X and Y , conditional entropy is described [9]

$$H(X/Y) = -\sum_{i=1}^n H(X/Y = y_i) * p(Y = i) \quad (8)$$

In other words, $H(X/Y)$ is entropy of X given every possible occurrence of Y , averaged over all the possible values Y can take.

The mutual entropy is defined as [9]

$$I(X, Y) = H(X) - H(X/Y) \quad (9)$$

Essentially, (9) defines the reduction in uncertainty of X due to the knowledge of Y .

2.4 Channel Capacity

Let X be an information source and let Y be an information sink. Then the mutual information defined in (9) is the actual amount of information about X available at the sink. The maximum value of the mutual information (distribution of X chosen to maximise the mutual information) is termed channel capacity [10].

$$C = \max(I(X, Y)), \quad (10)$$

where C is a channel capacity.

Shannon in his groundbreaking work [11] has shown that for the bandlimited system, with the information source having a Gaussian distribution and Additive White Gaussian Noise (AWGN) as a disturbance, the channel capacity C per unit bandwidth is

$$C[\text{bps} / \text{Hz}] = \log(1 + \text{SNR}) \quad (11)$$

Here $\text{SNR} = \frac{P_s}{W * N_0}$, with P_s as a signal power, W as bandwidth and N_0 as a noise power density.

Shannon has shown that channel capacity forms an upper bound for the transmission rate and that it is possible to transmit information at the rate as close to channel capacity as is desirable, with a negligible amount of error.

2.5 Multiple Input Multiple Output Systems

2.5.1 Capacity of the Multiple Input Multiple Output system

Multiple Input Multiple Output (MIMO) systems deploy multiple antennas at the transmitter as well as at the receiver. Let H be the channel matrix of $N \times M$ dimensions, where M is a number of transmit antennas and N is a number of receive antennas. For the case in figure 2, H is 3×3 . In the ideal case, each path is assumed to be statistically independent from the others. Independent data can be sent from each antenna, increasing the capacity of the system. MIMO is a very attractive setup because it offers a great increase in information capacity at the cost of increased complexity only, not increased bandwidth or power [12].

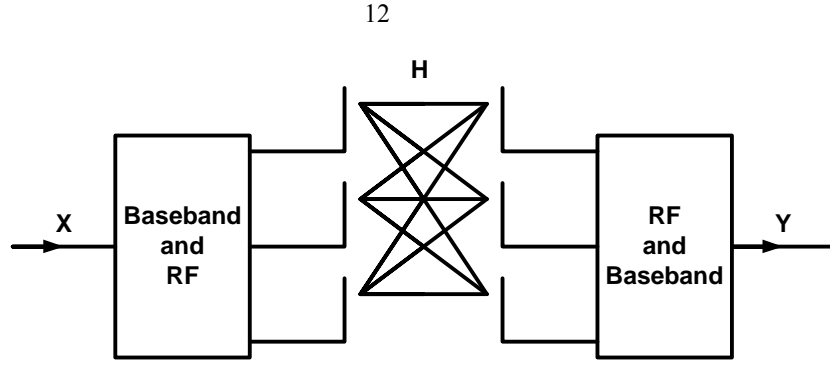


Figure 2. MIMO system employing multiple antennas at the receiver and transmitter

Capacity of the MIMO channel has been derived in [13] as

$$C_{MIMO} = \log_2 \left(\det \left[\mathbf{I}_R + \mathbf{H}^* \mathbf{Q} \mathbf{H}^H \right] \right) \quad (12)$$

where $[\]^H$ defines hermitian, \mathbf{Q} is an covariance matrix of the transmitted power and \mathbf{I}_R is an $N \times N$ identity matrix.

Assuming equal power sources [13], (12) can be presented as

$$C_{EP} [bps / Hz] = \sum_{i=1}^m \log_2 \left(1 + \frac{\rho}{M} * \lambda_i \right) \quad (13)$$

$\frac{\rho}{M}$ is the SNR per transmitting antenna, $m = \min \{N, M\}$ and λ_i is an i^{th} eigenvalue of the $\mathbf{H}^* \mathbf{H}^H$.

The main advantage, as seen in (13), is that the capacity grows linearly with m , while capacity in (11) grows only logarithmically with increased SNR.

If the channel \mathbf{H} is assumed time invariant, capacities in (12) and (13) are fixed values themselves. For the more realistic scenario, elements of \mathbf{H} are assumed to be generated by the ergodic process and Rayleigh, independent identically distributed (iid). Subsequently, capacity itself becomes a random variable [13]. If, for instance, some of the channel paths are in a deep fade,

matrix \mathbf{H} becomes ill conditioned. As a result, instantaneous capacity can drop below the rate of the system, severely increasing BER. The system designers usually aim at a capacity that has a certain fixed probability to stay above the data rate. The capacity is termed an outage capacity. Another adverse scenario occurs when channel paths become correlated (spatial correlation between antennas is the major cause). It also results in an ill-conditioned \mathbf{H} , with a drop in the capacity.

2.5.2 Using MIMO capacity

In practice there are two approaches to harness the high theoretical capacity of MIMO [14]: Spatial multiplexing for rate enhancement, and channel coding to achieve high reliability. These implementations require high complexity algorithms capable of multidimensional signal processing in real time. High complexity results in increased power consumption, which is extremely undesirable in mobile handsets. The thesis investigates the power and complexity issues of these algorithms.

2.5.2.1 Coding to enhance reliability

This method takes advantage of the additional spatial diversity that MIMO offers. Redundancy is now encoded in space (across antennas) and time, in order to combat the fading of the channel. Generally, Space Time Coding (STC) leads to signal-reliability improvement, so that even when one or more of the paths are in a fade it is still possible to obtain an error-free signal. Using spatial diversity, however, reduces the number of independent paths, which leads to a decreased maximum possible rate at the transmitter. Figure 3 shows a generalised setup for the space time coded MIMO.

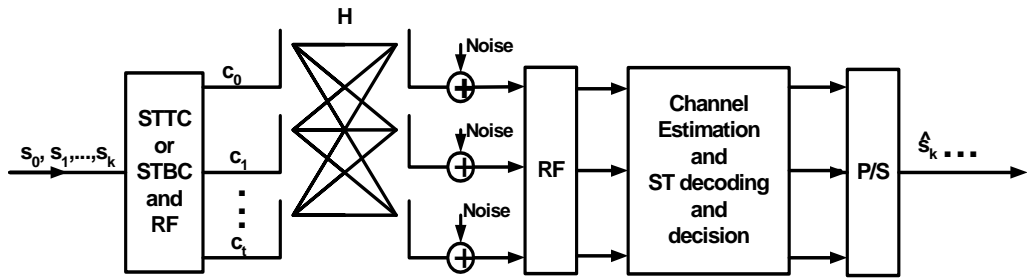


Figure 3. Space Time Coded MIMO system setup

The incoming signals s_0, s_1, \dots, s_k are mapped by a Space-Time Trellis Code (STTC) onto a codeword c_0, c_1, \dots, c_t and distributed among t antennas. At the receiver side the channel is estimated, the data is decoded and finally the original data is recovered and converted back into serial form.

STTC were developed in [15]. They provide an excellent performance at the expense of high complexity. Usually a sophisticated Viterbi type decoder is used [6]. Recently Space-Time Block (STBC) codes have emerged as an alternative type of ST codes [3]. They don't provide a coding gain (i.e. a gain in SNR over an uncoded system of the same rate) like STTC do. However, when compared to a SISO system, their BER performance improves much more quickly as SNR increases (in other words, they have a higher diversity gain). They also have a simple, low-complexity decoding technique. The low-complexity advantage has made STBC a preferred Space Time Coding technique in many practical applications, as well as accepting them as part of a 3GPP standard [16].

Chapter 3, as a contribution of this work, investigates one implementation issue of STBC: the clipping effect caused by Analog to Digital Conversion on STBC system performance.

2.5.2.1 Spatial Multiplexing

Spatial Multiplexing, shown in figure 4, relies on uncorrelated channel paths between the antennas. Generally, fewer antennas at the transmitter than at the receiver are deployed ($M \leq N$) to

increase the probability of the full rank matrix. Each antenna transmits a different symbol, making it possible to achieve high data rates.

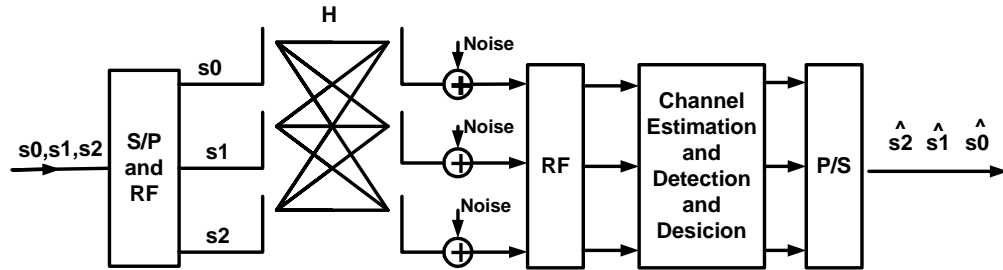


Figure 4. Spatial Multiplexing system structure

The transmission can be implemented simply by using a serial to parallel converter to distribute the signal among the M antennas. The task of channel estimation and detection at the receiver usually requires high-complexity algorithms. There are various types of detectors: Maximum Likelihood, Linear Zero Forcing (ZF), Linear Minimum Mean Square Error (MMSE) and Successive Interference Cancellation (SIC). Each has their own performance vs. complexity trade off. Chapter 4, which constitutes another major contribution of the work, deals with a number of the complexity issues associated with QR detection. This is one of the subset techniques of ZF and SIC. Chapter 4 essentially presents a method to reduce the complexity of the QR detection receiver.

3 Simulation-Based Clipping Analysis in Alamouti Space Time Block Codes

3.1 Chapter Outline

STBC codes provide higher information reliability through the wireless link compared to Single Input Single Output (SISO) uncoded systems. They achieve this by using multiple antennas at the transmitter (transmit diversity). There are various implementation issues that can affect the performance of the system. One such issue is a signal clipping caused by an ADC. In a power-conscious circuitry (such as the one in a wireless handset) ADC can be optimised to reduce the power consumption of the system at the expense of the increased clipping distortion of the signal. This chapter shows that STBC systems are more sensitive than uncoded systems to the ADC clipping. This fact has to be taken into account when optimising ADC for low power. Section 3.2.1 introduces a communication system based on a STBC. The Direct Conversion receiver and Log Polar receiver are reviewed in section 3.2.2. They are two types of receivers that can be used to implement STBC systems. The relevant properties of an ADC that affect the system performance are described in section 3.2.3. Section 3.3 introduces the phenomenon of the square and circular clipping occurring in a Direct Conversion receiver and in a Log-Polar receiver respectively. The effect of a square and circular clipping on STBC is theoretically shown in section 3.4. Target SER of

10^{-3} was chosen for simulation results in section 3.5. There, the lowest possible clipping levels (for given SER) were shown for SISO and STBC Multiple Input Single Output (MISO) schemes.

3.2 Introduction

3.2.1 Communication system based on STBC

Space Time Block codes [3] use multiple antennas and time as a coding domain. For a system with two transmit antennas, one receive antenna (2X1) and two symbols s_0 and s_1 the orthogonal coding matrix S is

$$S = \begin{bmatrix} s_0 & s_1 \\ s_1^* & -s_0^* \end{bmatrix} \quad (14)$$

with rows representing space and columns representing time domains, respectively.

A simplified block diagram of the Multiple Input Single Output (MISO), 2X1 STBC system is presented in figure 5.

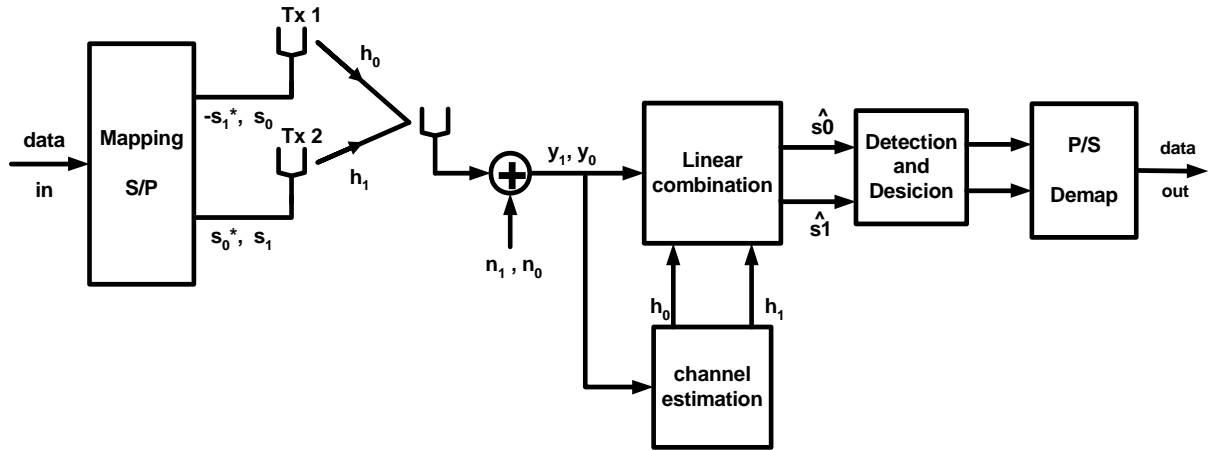


Figure 5. Simplified setup for 2X1 communication system based on STBC

First the data is mapped according to modulation (BPSK, M-PSK or M-QAM). The complex data is then arranged according to the format expressed in (14). At the first time slot, the first row of

(14) is transmitted, and at the second time slot, the second row of (14) is transmitted (see figure 5). Channel responses h_0 and h_1 are then estimated (block "channel estimation" in figure 5). The final received signal including channel response and complex noise can be written as

$$\begin{aligned} y_0 &= s_0 * h_0 + s_1 * h_1 + n_0 \\ y_1^* &= s_0 * h_1^* - s_1 * h_0^* + n_1^* \end{aligned} \quad (15)$$

where y_0 and y_1 are the received signals at two consecutive time slots. Two-channel responses h_0 and h_1 are assumed to be stationary during these two time slots. They are independent random Rayleigh distributed variables with zero mean and variance of one and are given by

$$h_0 = |h_0| e^{j\angle h_0}, \quad h_1 = |h_1| e^{j\angle h_1}$$

Noise variables n_0 and n_1 are two independent random Rayleigh distributed variables with zero mean and variance depending on signal to noise ratio. They can be represented as follows

$$n_0 = |n_0| e^{j\angle n_0}, \quad n_1 = |n_1| e^{j\angle n_1}.$$

We can rewrite (15) in a matrix form as

$$\begin{bmatrix} y_0 \\ y_1 \end{bmatrix} = \begin{bmatrix} h_0 & h_1 \\ h_1^* & -h_0^* \end{bmatrix} * \begin{bmatrix} s_0 \\ s_1 \end{bmatrix} + \begin{bmatrix} n_0 \\ n_1 \end{bmatrix} \quad (16)$$

with channel matrix \mathbf{H} given as $\mathbf{H} = \begin{bmatrix} h_0 & h_1 \\ h_1^* & -h_0^* \end{bmatrix}$.

The linear combiner (figure 5) recovers symbols s_0 and s_1 by multiplying the received signals in (16) by the conjugate-transpose of the channel matrix. It can be written as

$$\begin{bmatrix} \hat{s}_0 \\ \hat{s}_1 \end{bmatrix} = \mathbf{H}^* * \begin{bmatrix} y_0 \\ y_1 \end{bmatrix},$$

$$\begin{bmatrix} \hat{s}_0 \\ \hat{s}_1 \end{bmatrix} = \begin{bmatrix} h_0^* & h_1 \\ h_1^* & -h_0 \end{bmatrix}^* \begin{bmatrix} y_0 \\ y_1 \end{bmatrix}; \quad (17)$$

$$\begin{bmatrix} \hat{s}_0 \\ \hat{s}_1 \end{bmatrix} = \begin{bmatrix} |h_0|^2 + |h_1|^2 & 0 \\ 0 & |h_0|^2 + |h_1|^2 \end{bmatrix}^* \begin{bmatrix} s_0 \\ s_1 \end{bmatrix} + \begin{bmatrix} h_0^* * n_0 + h_1 * n_1^* \\ h_1^* * n_0 - h_0 * n_1^* \end{bmatrix} \quad (18)$$

Equations (17) and (18) show the advantage of the orthogonal coding. There is no need for a channel matrix inversion in order to force off-diagonal components to zero in (18). Multiplication by the conjugated transposed channel matrix is sufficient to separate the symbols.

Linear combination is followed by detection (usually ML, MMSE or ZF), hard decision, parallel to serial conversion and finally symbol de-mapping to obtain the binary data.

In practical RF systems a number of distortions are added to the signal before it is STBC decoded. One of these is a clipping distortion caused by the Analog to Digital Converter. The ADC forms an integral part of any receiver that uses digital signal processing [17]. The next section will introduce two types of receivers:

- Direct Conversion (DC) receiver [18], the most common receiver architecture in use today. It uses two ADCs located on the Imaginary and Quadrature arms of the receiver
- Log-Polar receiver is an alternative receiver structure to a DC structure [19]. The complex envelope signal recovery is performed in a polar format. One ADC is used to digitise the phase of the signal, obtained from the hard clipped envelope and another ADC digitises the log-magnitude of the received signal

3.2.2 Receiver architectures

3.2.2.1 Direct Conversion receiver structure

Figure 6 shows the simplified Direct Conversion (DC) receiver structure.

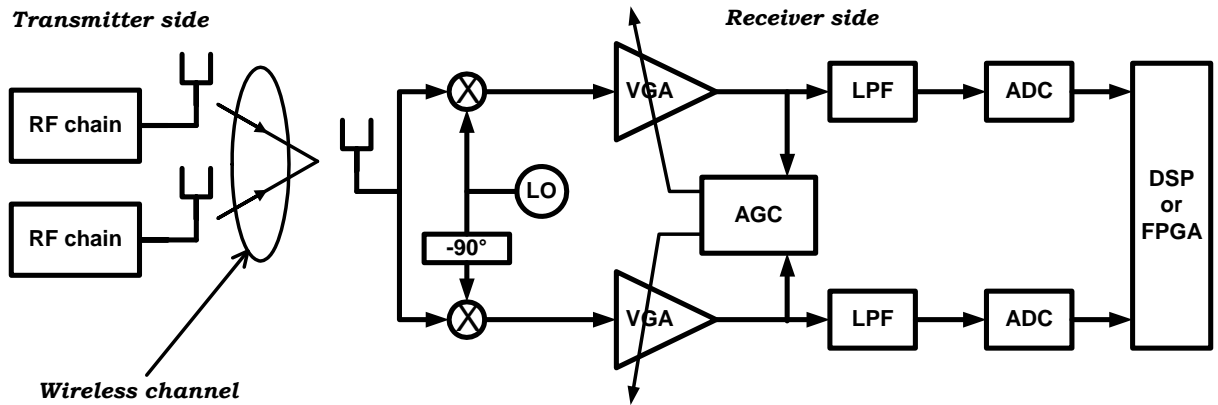


Figure 6. STBC system implementation based on DC receiver structure

The coded signal is transmitted from the two antennas. The inphase branch is formed when the Local Oscillator (LO in figure 6) is mixed with the input signal, effectively down converting it. The Local Oscillator waveform is shifted 90° and mixed with the input waveform to form a quadrature branch.

Mixers are followed by the Variable Gain Amplifiers (VGAs), the gain of which is controlled by the Automatic Gain Control (AGC). The AGC causes weak signals to be amplified so that ADC that follows later in the receiving chain can digitise this signal with the acceptable resolution. The AGC also reduces the gain of VGA so that the strong signals are attenuated, preventing the magnitude of the signals to exceed the maximum amplitude that ADC can handle.

Low Pass Filters (LPF in the figure above) are used as anti-aliasing filters. ADCs that follow digitise Inphase and Quadrature signal components (ADC blocks in figure 6). ADCs introduce a quantisation noise among the host of other types of non-linearity [20]. Also, despite the AGC

control, white noise can drive the instantaneous amplitude of the signal above the maximum voltage level that ADC can handle. Then ADC gets saturated and clips the signal, causing a distortion. Finally digital signal processing is applied to the digitised discrete signal.

An effect of clipping from the two independently operating ADCs on the STBC system is investigated in this work.

3.2.2.2 Log-Polar receivers

In the non-stationary environment the distance between the transmitter and the receiver changes randomly with time. The signal often has a large magnitude swing (large dynamic range). It is much harder then for AGC in a Direct Conversion receiver to keep the signal amplitude within the desired range and prevent ADC from saturation.

Paul Wilkinson of Ericsson[®] has proposed to use a Log-Polar receiver structure for the described scenario [19]. It uses logarithmic amplifiers to increase the acceptable range of the input signals at the expense of the introduced signal distortion. Figure 7 shows the schematic diagram of the receiver.

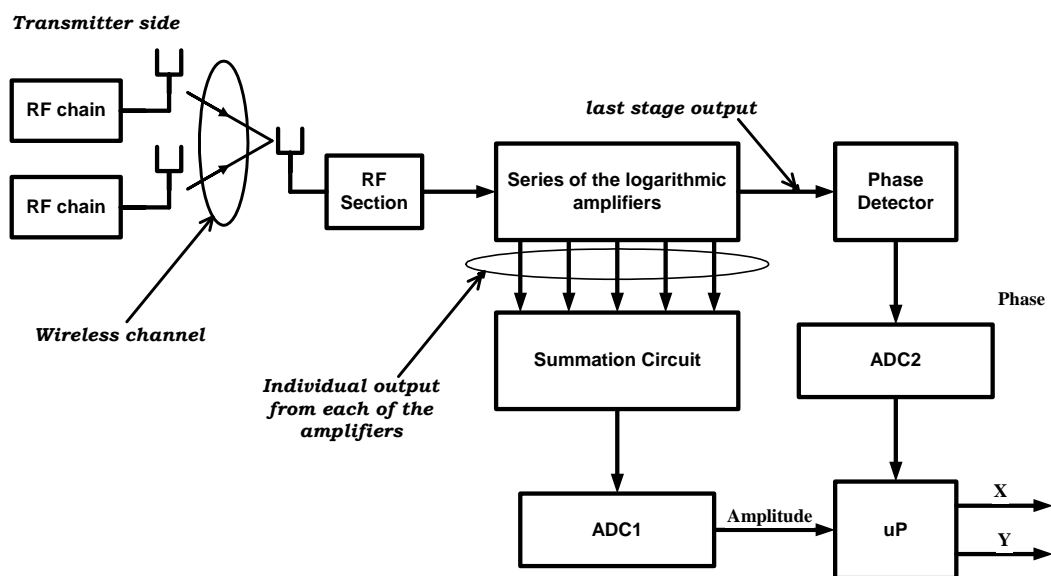


Figure 7. Block diagram of the Log-Polar receiver

After the RF stage, the signal passes through a series of logarithmic amplifiers. Each amplifier is designed to saturate every 1dB (relative to the input voltage) increase in the voltage level. The last amplifier in the chain is saturated first, followed by the preceding amplifier and so on. Thus the maximum possible input signal level is limited by the number of the amplifier stages. The outputs of the individual amplifiers are summed to obtain the total log-magnitude value of the signal. The logarithmically processed signal enables ADC1 in figure 7 to accommodate large swings in the amplitude of the incoming signal. The downside, however, is that the signal becomes exponentially distorted (the signal is compressed harder as its amplitude grows). The digitised signal magnitude is then fed into a microprocessor. The output of the last amplifier is also applied to a phase detector, which then extracts the phase information out of the received signal (the phase value is retained even when the signal is hard clipped due to the amplifier saturation). The phase value is converted into a digital form by the second ADC (ADC2) and is also fed into a microprocessor. The task of the microprocessor is to convert the Polar representation of the signal into the Cartesian one. This receiver structure is most suitable for the phase-modulated schemes (like M-PSK), where the introduced distortion of the magnitude of the signal does not affect the system performance.

The clipping effects of the ADC1 onto QPSK modulated STBC systems are studied in this work.

3.2.3 Signal conversion

Figure 8 shows the equivalent representation of ADC

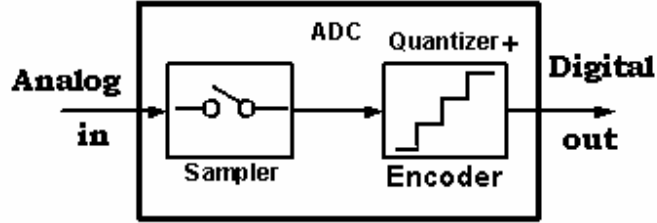


Figure 8. ADC broken down into a sampler and quantiser

ADC consists of two major parts. First, the input analog waveform has to be sampled at a frequency at least twice as high as the bandwidth of the input waveform to avoid aliasing [21]. Then incoming samples are quantised into discrete levels and binary encoded. For an ADC with A bits and full-scale range V_F , q – the size of the quantisation step is given by

$$q = \frac{V_F}{2^A - 1} \approx \frac{V_F}{2^A} \quad (19)$$

Signal quantisation induces a quantisation error ε in the system. It has a uniform distribution in the range $\pm \frac{q}{2}$. Then its power σ_ε^2 can be calculated

$$\sigma_\varepsilon^2 = \int_{-\frac{q}{2}}^{\frac{q}{2}} \varepsilon^2 * p(\varepsilon) d\varepsilon; \quad (20)$$

$$\sigma_\varepsilon^2 = \frac{1}{q} \int_{-\frac{q}{2}}^{\frac{q}{2}} \varepsilon^2 d\varepsilon = \frac{q^2}{12}$$

where $p(\varepsilon)$ denotes a probability distribution function of ε .

The dynamic range of an ADC is defined as the ratio between the maximum to minimum levels the ADC can accept. With the maximum level as V_F , the minimum level as q , the dynamic range D is

$$D = \frac{V_F}{q} = \frac{V_F}{\left(\frac{V_F}{2^A}\right)} = 2^A; \quad (21)$$

$$D[dB] = 20 * \log(2^A)$$

The more bits the ADC has, the higher its dynamic range; that is, the wider the range of signal amplitudes it can handle.

Reducing the dynamic range will reduce the power consumption of the ADC at the expense of increased quantisation noise. The maximum voltage level V_F can subsequently be lowered to counteract the increased quantisation noise. However, there is then an increased risk of signal clipping by the ADC, because it is more likely that the maximum signal amplitude can exceed V_F . The signal, distorted by the clipping, impairs the overall performance of the system. It is possible to optimise the ADC power consumption by choosing the lowest number of bits and the lowest V_F for certain Symbol Error Rate (SER).

The rest of the chapter comprises novel work that investigates the performance deterioration of the Alamouti STBC structure employing two transmit and one receive antennas in the presence of ADC clipping in DC and Log Polar receivers for 10^{-3} target SER.

3.3 Clipping in SISO systems

3.3.1 DC receivers and square clipping

A conceptual example of a square clipping in a DC receiver is shown in figure 9.

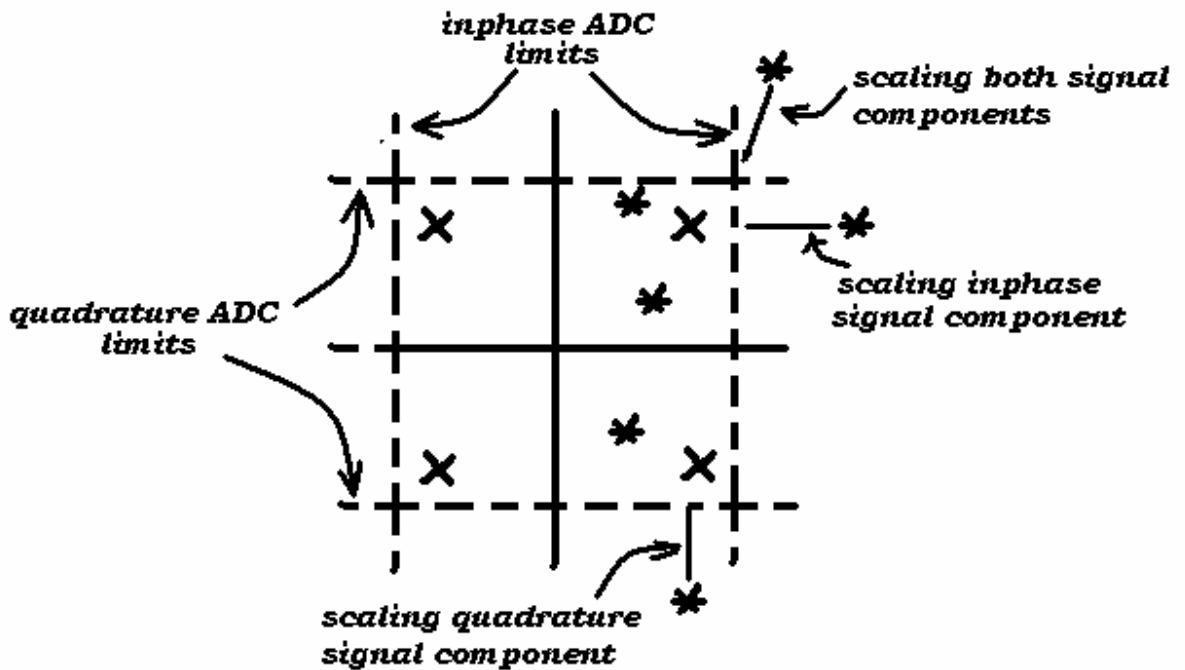


Figure 9. A conceptual example of the square clipping of a QPSK modulated signal

The square region in figure 9 is formed by the maximum acceptable signal amplitudes of the inphase and quadrature ADCs. Inside this bounded region four original signal constellations are shown ("X"es in the figure). The received signal (represented by stars in figure 9) outside of this region is scaled (or clipped) by ADCs. The soft limiting operation of each ADC is shown in the figure below

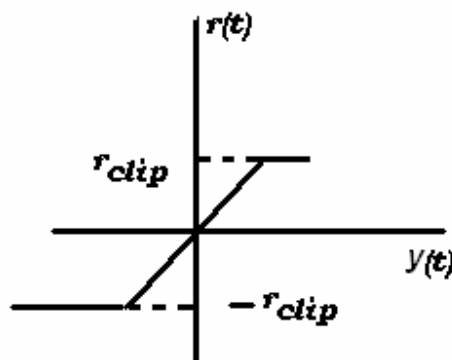


Figure 10. Soft limiting operation of ADC in a DC receiver

At any time instant t , clipping either the inphase or quadrature branch of the complex signal can be represented as follows:

$$r(t) = \begin{cases} y(t), & |y(t)| < r_{clip} \\ \alpha * y(t), & |y(t)| \geq r_{clip} \end{cases} \quad (22)$$

$$\alpha = \frac{r_{clip}}{|y(t)|}$$

In (22) and in figure 10, $y(t)$ is a received signal before the clipping and $r(t)$ is a signal after the clipping. Following the definition in (22), the scaling coefficient α has the following properties:

$$\alpha = \begin{cases} 1, & |y(t)| < r_{clip} \\ \frac{r_{clip}}{|y(t)|}, & |y(t)| \geq r_{clip} \end{cases} \quad (23)$$

Two ADC converters operate independently on inphase and quadrature parts of the complex input signal. Then the received signal can be shown as:

$$\begin{aligned} r &= \alpha_r * (s_r * h_r - s_i * h_i + n_r) + j * \alpha_i * (s_r * h_i + s_i * h_r + n_i); \\ r &= [\alpha_r * (s_r * h_r - s_i * h_i) + j * \alpha_i * (s_r * h_i + s_i * h_r)] + (\alpha_r * n_r + j * \alpha_i * n_i) \end{aligned} \quad (24)$$

In (24) reference to time is omitted; $s = s_r + js_i$ is a transmitted symbol; $h = h_r + jh_i$ is a sample of the complex i.i.d channel; $n = n_r + jn_i$ represents a complex noise snapshot; α_r and α_i are clipping coefficients of the inphase and quadrature branches respectively.

3.3.2 Log-Polar receivers and circular clipping

A conceptual example of a circular clipping in a Log-Polar receiver is shown in figure 11.

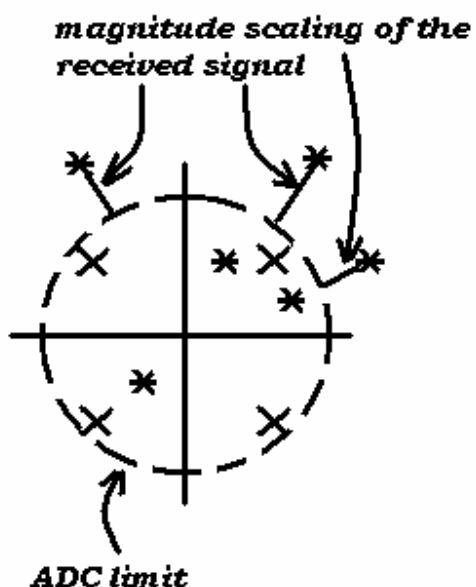


Figure 11. Magnitude clipping in a Log-Polar receiver employing QPSK modulation

The full-scale range of ADC1 in figure 7 forms a circular boundary on the Cartesian plane in figure 11. The ADC clips (or scales) all the complex signals whose magnitude exceeds this boundary. The soft clipping operation of this ADC is presented in figure 12

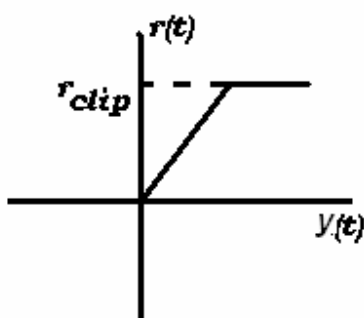


Figure 12. Soft limiting operation of the ADC in a Log-Polar receiver

The definition of the clipping coefficient for the circular clipping case is identical to (23) and (24). Then the received clipped signal can be written as

$$r = \alpha * (s * h + n) \quad (25)$$

Here, reference to time is omitted; both the real and imaginary components of r are scaled equally by α .

The next section will use the defined scaling coefficient to investigate clipping effects in the DC and Log-Polar receivers that employ STBC.

3.4 Clipping in Alamouti STBC System

3.4.1 Square clipping

The clipped form of the STBC signal is represented by

$$\begin{aligned} r(t_0) &= \alpha_{0r} * \text{Re}(s_0 * h_0 + s_1 * h_1 + n_0) + j * \alpha_{0i} * \text{Im}(s_0 * h_0 + s_1 * h_1 + n_0) \\ r(t_1) &= \alpha_{1r} * \text{Re}(s_0 * h_1^* - s_1 * h_0^* + n_1^*) + j * \alpha_{1i} * \text{Im}(s_0 * h_1^* - s_1 * h_0^* + n_1^*) \end{aligned} \quad (26)$$

In (26) α_0 is a scaling coefficient at time slot zero and α_1 is a scaling coefficient at time slot one.

Defining:

$$\begin{aligned}
\rho_{0r} &= \alpha_{0r} * |h_0|^2 + \alpha_{1r} * |h_1|^2, \quad \rho_{0i} = \alpha_{0i} * |h_0|^2 + \alpha_{1i} * |h_1|^2; \quad \frac{n!}{r!(n-r)!} \\
\rho_{1r} &= \alpha_{1r} * |h_0|^2 + \alpha_{0r} * |h_1|^2, \quad \rho_{1i} = \alpha_{1i} * |h_0|^2 + \alpha_{0i} * |h_1|^2; \\
d\alpha_r &= (\alpha_{0r} - \alpha_{1r}), \quad d\alpha_i = (\alpha_{0i} - \alpha_{1i});
\end{aligned} \tag{27}$$

Then, after multiplying by transposed-conjugated channel matrix and further defining,

$$\begin{aligned}
k_0 &= \text{Re}(h_0^* * h_1) * (d\alpha_r * s_{1r} + j * d\alpha_i * s_{1i}) - \text{Im}(h_0^* * h_1) * (d\alpha_r * s_{1i} + j * d\alpha_i * s_{1r}) \\
k_1 &= \text{Re}(h_0 * h_1^*) * (d\alpha_r * s_{0r} + j * d\alpha_i * s_{0i}) - \text{Im}(h_0 * h_1^*) * (d\alpha_r * s_{0i} + j * d\alpha_i * s_{0r})
\end{aligned} \tag{28}$$

Symbol estimates then can be presented

$$\begin{aligned}
\hat{s}_0 &= (\rho_{0r} * s_{0r} + j\rho_{0i} * s_{0i}) + k_0 + (h_0^* * n_{0c} + h_1 * n_{1c}^*) \\
\hat{s}_1 &= (\rho_{1r} * s_{1r} + j\rho_{1i} * s_{1i}) + k_1 + (h_1^* * n_{0c} - h_0 * n_{1c}^*)
\end{aligned} \tag{29}$$

Here n_{0c} and n_{1c} represent the Inphase Quadrature clipped noise in time slots zero and one respectively.

STBC uses time as a coding domain. As a result of the coding, the two consecutive STBC samples become orthogonal. Clipping in the time domain will affect coding by breaking orthogonality between the samples. The terms k_0 and k_1 represent cross-talk terms, showing the degree of orthogonality loss due to the clipping. These cross-talk terms will cause an additional error when the signal passes through the threshold detector. The cross-talk terms will disappear if the clipping is identical in the two consecutive time slots.

3.4.2 Circular clipping

The STBC signal, affected by the circular clipping, can be written as

$$\begin{aligned} r_{i0} &= \alpha_0 * (s_0 * h_0 + s_1 * h_1 + n_0) \\ r_{i1} &= \alpha_1 * (s_0 * h_1^* - s_1 * h_0^* + n_1^*) \end{aligned} \quad (30)$$

As in the case for square clipping, the top line defines the signal at the first time slot and the second line at the second time slot.

Defining

$$\begin{aligned} \rho_{0r} &= \alpha_0 * |h_0|^2 + \alpha_1 * |h_1|^2; \\ \rho_{1r} &= \alpha_1 * |h_0|^2 + \alpha_0 * |h_1|^2; \\ d\alpha_r &= (\alpha_0 - \alpha_1). \end{aligned} \quad (31)$$

Since only the magnitude is clipped, k_0 and k_1 in (28) can be rewritten to suit the circular clipping case

$$\begin{aligned} k_0 &= d\alpha * (h_0^* * h_1) * s_1 \\ k_1 &= d\alpha * (h_0 * h_1^*) * s_0 \end{aligned} \quad (32)$$

Finally, the symbol estimates are presented as

$$\begin{aligned} \hat{s}_0 &= \rho_0 * s_0 + k_0 + (h_0^* * n_{0c} + h_1 * n_{1c}^*) \\ \hat{s}_1 &= \rho_1 * s_1 + k_1 + (h_1^* * n_{0c} - h_0 * n_{1c}^*) \end{aligned} \quad (33)$$

Here the cross-talk terms k_0 and k_1 also appear, due to the orthogonality loss in the coding.

3.5 Simulations and Comparisons

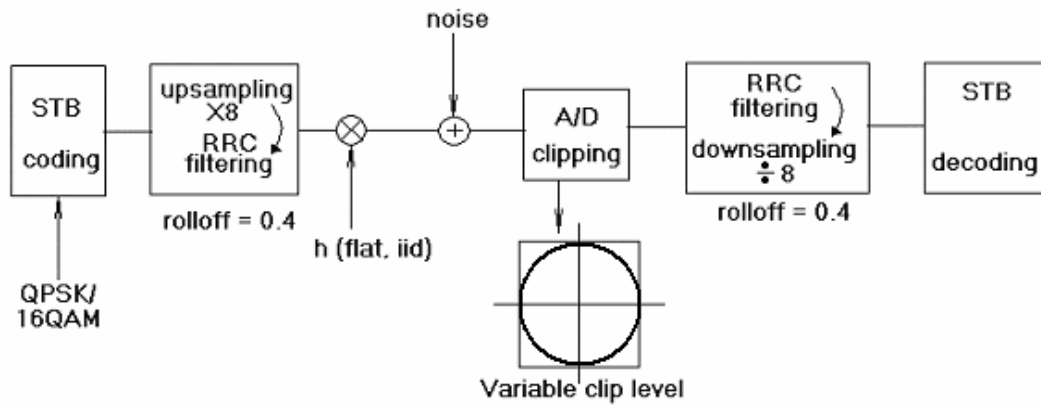


Figure 13. Simulation block diagram

Figure 13 shows the block diagram and specifies all the necessary parameters used to produce the simulation results. The channel is ideally estimated at the receiver, and assumed to be flat fading, having complex Gaussian Independent Identically Distributed (i.i.d) samples. All the clip values are taken relative to the received signal Root Mean Square (rms) value (without the noise).

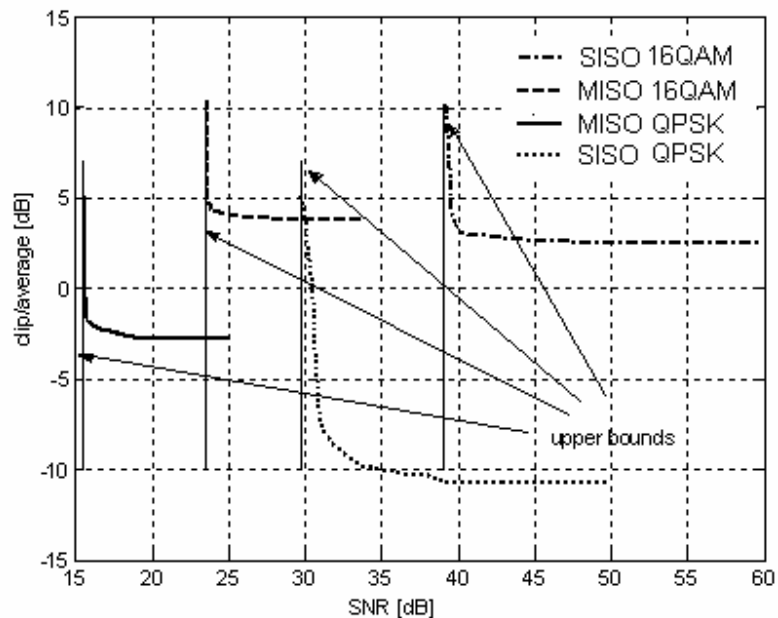


Figure 14. Lowest clip/average levels for 10^{-3} target SER, DC receiver, square clipping

Figure 14 shows the lowest possible clipping levels at different SNR values, while maintaining target 10^{-3} SER for square clipping: STBC QPSK, STBC 16QAM, SISO QPSK and SISO 16QAM. For all four schemes, inter-symbol-interference (ISI) caused by Root Raised Cosine (RRC) filters is one of the error contributors besides AWGN. For STBC schemes, however, the cross-talk noise is another major contributor of the error. This is the reason for the STBC signal clip floor being 1dB higher than the clipping floor of the SISO scheme for 16QAM modulation. This difference expands to 7dB for the QPSK system, as depicted in figure 14. STBC systems perform 15 dB better when compared to SISO schemes for the same clipping levels. This is true for both constellation densities used for this research.

For the circular clipping scenario (STBC system with QPSK modulation), the unrealistically low clipping level of -30dB was found to induce a symbol error rate of $3 \cdot 10^{-4}$, way below the target SER of 10^{-3} . The Log-Polar receiver structure is essentially clipping insensitive at this particular target SER.

Figure 15 compares the sensitivity of STBC and SISO schemes in the presence of square clipping.

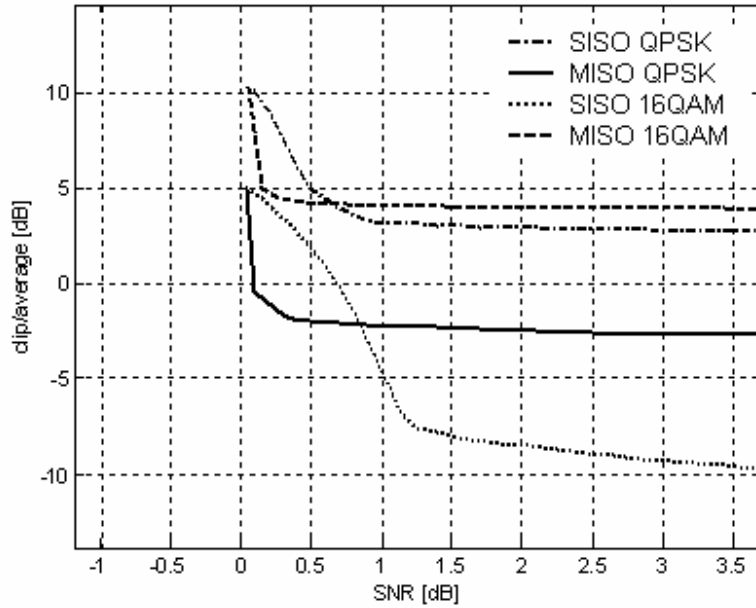


Figure 15. Sensitivity of STBC and SISO schemes to AWGN at 10^{-3} target SER, DC receiver, square clipping.

This plot is built by lining up the upper bounds of all schemes to zero. The amount of SNR required for every scheme to achieve its clip floor can be defined as the noise sensitivity of the scheme.

It takes about 0.5 dB of change in SNR for the STBC system to achieve its clip floor (QPSK and 16QAM). This value is 1dB for SISO 16QAM and about 9dB for SISO QPSK. It is also important to note in figure 15 that from 0 to 0.5 dB for 16QAM and from 0 to 0.7 dB for QPSK, STBC schemes have lower clip levels, making them superior to SISO schemes within this SNR range.

3.6 Conclusions

Space Time Block codes provide higher transmission reliability in the wireless environment compared to the SISO systems. In practical receivers, however, a number of distortions are added to the signal before it is STBC decoded. One form of ADC clipping was investigated in this work. Two

receiver structures were considered: the DC receiver structure that employs two ADCs on the inphase and quadrature branches and the Log-Polar receiver that recovers the complex envelope in the polar form. It has one ADC to digitise the magnitude and another one to digitise the phase of the received signal. The two independently operating ADCs in a DC receiver induce a square clipping, while an ADC that digitises the signal magnitude in a Log-Polar receiver causes a circular clipping on the Cartesian plane.

STBC rely on orthogonal coding to separate individual symbols. It was shown that ADC clipping leads to breaking the code orthogonality. As a result, cross-talk interference can adversely affect the performance of the system. For the square clipping case, simulations have confirmed that STBC schemes have a higher clip floor and are more sensitive to AWGN than SISO systems. For receiver designers this means that they must increase signal back off into ADC by 7 dB for QPSK and 1 dB for 16QAM with Alamouti STBC scheme.

The Log-Polar receiver, however, was found to be clipping insensitive for the target SER of 10^{-3} . For the phase-modulated systems, like MPSK, where the logarithmic distortion of the magnitude does not affect the performance of the system, the Log-Polar receiver is an obvious choice for the system designer.

4 Complexity Reduction through Upper Triangular Matrix Tracking in QR Detection MIMO Receivers

4.1 Chapter Outline

QR equalisation is a computationally intensive process often required for MIMO detection. When the QR equalisation is used with channel tracking, QR decomposition (part of a QR equalisation process) has to be performed at every instance the new channel estimate is obtained. This will result in a high computational complexity per symbol. This chapter proposes a technique that reduces the number of operations in MIMO systems in the described scenario. A non frequency-selective channel such as that found in Orthogonal Frequency Division Multiplex (OFDM) systems is assumed. We propose to reduce the frequency of QR decompositions while continuing to track the channel H . The Q and R matrices are held fixed for a number of symbol periods between adjacent QR decompositions. This will result in a complexity reduction at the expense of a growing equalisation error caused by the outdated Q and R . We further suggest tracking the upper triangular matrix, while holding the unitary matrix Q fixed, instead of tracking the channel H . The R matrix loses its upper triangular form with time because of the fixed Q . It is shown, however, that this modification will result in a slower equalisation error growth, allowing a further decrease in frequency of the QR decompositions. When used with SIC-MMSE detection, however, the upper

triangular matrix tracking does not show any BER advantage over the channel-tracking scenario and also results in a higher computational complexity. Both LMS channel tracking schemes are then compared with the RLS-DFE tracking system of [1]. The equalizer coefficients (inverse channel) exhibit higher dynamics than the channel and suggest the possibility of using lower complexity tracking schemes. Both LMS strategies had an inferior BER performance compared to the DFE RLS-based system, and surprisingly the LMS schemes showed no significant complexity improvement. The work has been published in [72]. The chapter is organised as follows.

Section 4.2 introduces the 802.11n channel model, reviews existing detection and estimation techniques in MIMO, explains the importance of tracking in MIMO systems and formulates the problem.

Section 4.3 describes two tracking strategies and compares their performance based on the MSE of the channel-estimate metric. The section also reviews the application of the CORDIC algorithm to QRD and highlights potential modifications that can be exploited when the target matrix is nearly upper triangular.

The BER performance of both channel and upper triangular matrix tracking strategies with SIC-MMSE detection is presented in section 4.4.

Finally, section 4.5 draws the conclusion to the chapter.

4.2 Introduction

4.2.1 IEEE 802.11 TGn channel model

Simulations in section 4.3 are based on the IEEE 802.11 TGn channel model [22, 23]. This wideband channel model has been developed for the MIMO indoor environment and uses a cluster approach [22] where the multipath components arrive at the receiver grouped in clusters. Spatial correlation between antennas is assumed. Characteristics like antenna spacing, power angular

spectrum, angle spread, mean angle of departure and arrival determine the degree of correlation [22].

Channel models are developed for the standard indoor A-F environments (for instance, A is flat fading, B is residential, etc.). This model uses the following formula to describe the Doppler spectrum of the signal

$$S(f) = \frac{1}{1 + 9 * \left(\frac{f - f_c}{f_d} \right)^2} \quad (34)$$

The Doppler frequency f_d was experimentally determined to be 6Hz for the indoor environment [22]. This model assumes near-stationary transmitters and receivers and moving scatterers. An example could be an office environment, where the access point and notebooks are stationary and walking people are scatterers. The F environment was selected for this work because it had the highest Doppler spread. It includes one fast-moving scatterer at 40km/h. Practically, this can be a car moving outside the office window.

Figure 16a compares the Doppler spectrum of the 802.11n models A to E to Clarke's model [4]. The frequency spectrum from the right of the carrier frequency f_c is plotted for both cases. Clarke's model assumes the highest Doppler component of 6Hz. Figure 16b shows the channel F spectrum with the extra peak caused by the additional moving object.

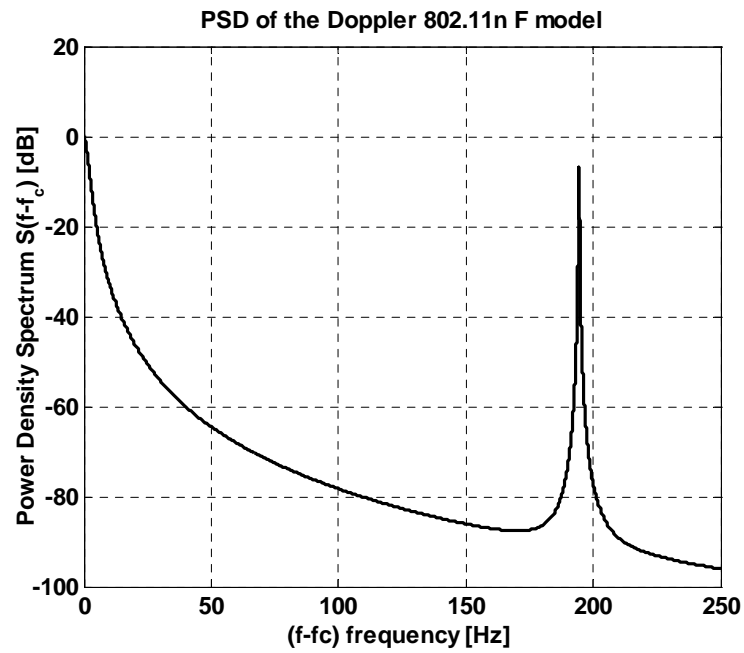
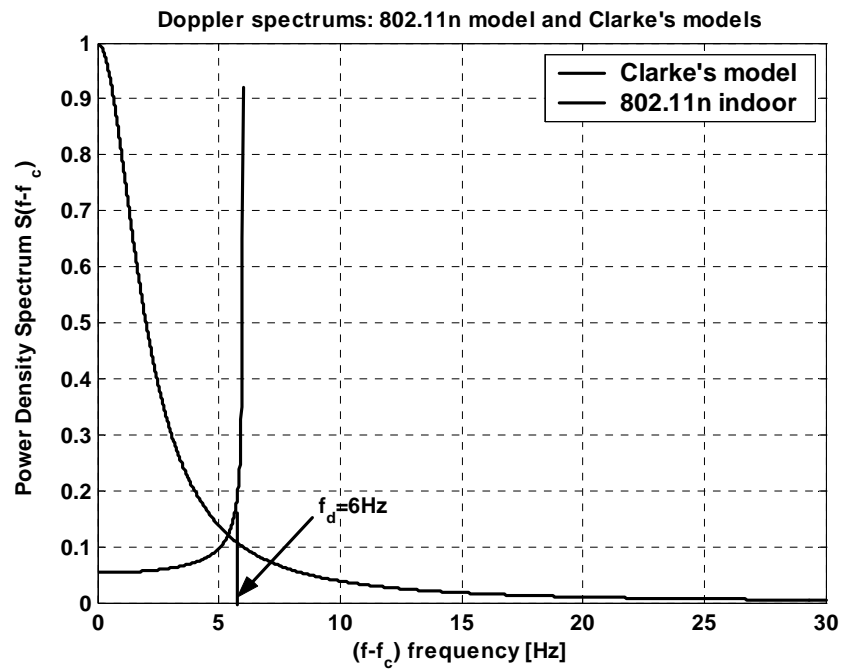


Figure 16. (a) Doppler spectra used in 802.11n and Clarke's models (b) 40km/h moving object causes peak at 194 Hz. $f_c=5.25\text{GHz}$.

It can be observed from figure 16a that unlike Clarke's model, where most of the power spectrum is contained in the frequency components close to f_d , most of the power spectrum in 802.11n is retained around the carrier frequency f_c . Also the 802.11n curve is truncated at f_{\max} of five times the Doppler frequency (30KHz in our case). In the case of channel F (figure 16b) the moving cluster causes a significant amount of energy at 194Hz.

4.2.2 Detection in MIMO

MIMO systems offer high theoretical information capacities. Spatial multiplexing is used to achieve these high capacities, as stated in chapter 2. There are various ways to perform symbol detection in spatial multiplexing systems, and this sub-section will describe some of them.

The received baseband $N \times 1$ signal vector \mathbf{y}_i at i^{th} time instant can be expressed as

$$\mathbf{y}_i = \mathbf{H}\mathbf{s}_i + \mathbf{n}_i \quad (35)$$

where \mathbf{H} is an $N \times M$ channel matrix assumed known at the receiver, \mathbf{s}_i is $M \times 1$ transmitted signal vector, \mathbf{n}_i is an $N \times 1$ additive WGN vector where each element is distributed as $\square N(0, \sigma_n^2)$.

For the constellation of size θ , the set of all possible constellation symbols is defined as $K_\theta = \{s_1, s_2, \dots, s_\theta\}$.

The optimum Maximum Likelihood Sequence Detector (MLSD) [6] finds Euclidean distances between the received signal vector \mathbf{y}_i and all the possible sequences of transmitted symbol vectors distorted by the channel. Then the symbol vector, corresponding to the minimum distance is chosen as an estimate of the transmitted symbol vector $\hat{\mathbf{s}}_i$.

$$\hat{\mathbf{s}}_i = \arg \min_{T \in K_\theta^M} (|\mathbf{y}_i - \mathbf{H}\mathbf{T}|) \quad (36)$$

where K_{θ}^M is a space of all the available sequences.

There are θ^M possible sequences that MLSD has to consider to make a choice. The complexity increases exponentially with the number of antennas, which severely restricts its use in practical systems. Less complex, suboptimum detectors are described in the following sub-sections.

4.2.2.1 Linear detectors

Linear detectors obtain the estimate of the transmitted symbol via linear mapping $\hat{\mathbf{s}}_i = \mathcal{G}(\mathbf{A}\mathbf{y}_i)$ where $\mathcal{G}(\cdot)$ denotes a hard decision and \mathbf{A} is chosen according to the two following criteria:

1. ZF criteria [24]: $\mathbf{A} = \mathbf{H}^{-1}$. Symbol estimate is then

$$\hat{\mathbf{s}}_i = \mathbf{A}\mathbf{y}_i = \mathbf{H}^{-1}\mathbf{H}\mathbf{s} + \mathbf{H}^{-1}\mathbf{n} \quad (37)$$

Defining error covariance matrix as

$$\mathbf{P} = E\left[(\mathbf{s}_i - \hat{\mathbf{s}}_i)(\mathbf{s}_i - \hat{\mathbf{s}}_i)^{\mathbf{H}}\right] \quad (38)$$

For the ZF case

$$\mathbf{P} = E\left[(\mathbf{s}_i - \mathbf{s}_i - \mathbf{H}^{-1}\mathbf{n}_i)(\mathbf{s}_i - \mathbf{s}_i - \mathbf{n}_i^{\mathbf{H}}\mathbf{H}^{-\mathbf{H}})\right] = \sigma_n^2(\mathbf{H}^{\mathbf{H}}\mathbf{H})^{-1} \quad (39)$$

The WGN noise amount in the symbol vector estimate will be amplified by small eigenvalues, $(\mathbf{H}^{\mathbf{H}}\mathbf{H})^{-1}$ that occur when the channel is faded or ill conditioned. It was shown in [25-27] that ZF detection with Bit Interleaved Coded Modulation (BICM) can asymptotically achieve ML performance as the number of antennas grows to infinity.

2. MMSE criteria [24]: Here the error metric is defined as

$$\varepsilon = E \left[\left| \mathbf{s}_i - \hat{\mathbf{s}}_i \right|^2 \right] \quad (40)$$

After presenting the symbol vector estimate $\hat{\mathbf{s}}_i$ as a linear combination of the received signal vector \mathbf{y}_i , error ε can be minimised in the linear sense

$$\varepsilon_{\min} = \arg \min_{\mathbf{A} \in \mathbb{R}^{M \times 1}} E \left[\left| \mathbf{s}_i - \mathbf{A}^H \mathbf{y}_i \right|^2 \right] \quad (41)$$

The optimum (in linear MMSE sense) \mathbf{A}_{opt} that corresponds to minimum error can be derived as

$$\begin{aligned} \mathbf{A}_{opt} &= E \left[\mathbf{y}_i \mathbf{y}_i^H \right]^{-1} E \left[\mathbf{y}_i \mathbf{s}_i^H \right]; \\ \mathbf{A}_{opt} &= \left(\sigma_n^2 \mathbf{I}_{N \times N} + \sigma_s^2 \mathbf{H} \mathbf{H}^H \right)^{-1} \mathbf{H} \end{aligned} \quad (42)$$

where σ_s^2 is a signal power.

The error covariance matrix is obtained as follows [28]

$$\begin{aligned} P &= E \left[(\mathbf{s} - \hat{\mathbf{s}})(\mathbf{s} - \hat{\mathbf{s}})^H \right]; \\ P &= \sigma_n^2 \left(\sigma_n^2 \mathbf{I}_{M \times M} + \mathbf{H}^H \mathbf{H} \right)^{-1} \end{aligned} \quad (43)$$

where the signal is assumed to have a unit power.

Since the noise power is included in the inversion term, small eigenvalues of $\mathbf{H}^H \mathbf{H}$ will not result in large noise amplification in the symbol vector estimate. MMSE detection in MIMO is used in [29, 30].

Importantly, for both ZF and MMSE methods the amount of noise amplification in the symbol vector estimate will be dominated by the smallest eigenvalue in $(\mathbf{H}^H \mathbf{H})$ and $(\sigma_n^2 \mathbf{I}_{M \times M} + \mathbf{H}^H \mathbf{H})$ respectively.

4.2.2.2 *Non-linear detectors*

There are suboptimum detection algorithms that try to capture an optimum ML solution at a fraction of the complexity of MLSD. The Sphere Detector [31-35] is one such algorithm and the Space Alternating Generalised Expectation maximisation is another [36].

VBLAST is an adaptation of the ordered Successive Interference Canceller (SIC), which is well known in the Multi-User Detection area for MIMO detection [37]. Both terms VBLAST and SIC will refer to the algorithm throughout this section. Unlike ZF and MMSE detectors, where all the symbols are recovered simultaneously, VBLAST detects symbols iteratively, one by one. $N \geq M$ is the condition to be satisfied for VBLAST to work. The algorithm consists of two parts: Nulling and Cancellation.

1. The row with the smallest norm of inverted H is chosen (nulling vector for ZF case) and the corresponding symbol is recovered. This is a nulling step;
2. The corresponding column of H is erased and the symbol, multiplied by this column vector, is subtracted from the received signal y . This is a cancellation step of the algorithm.

The described process is repeated with deflated H until all the symbols (or layers) have been recovered. The excellent, detailed explanation of VBLAST is provided in [38]. Authors of the original paper have reported a complexity of $O(M^4)$, which is considerably smaller than that of the MLSD algorithm.

The iterative structure of VBLAST increases the magnitude of the smallest row in H on every iteration. Choosing the row with the smallest norm results in the least number of detection errors compared to other possible choices. As the author in [38] has shown, this order of choice is the global optimum. Ordering and repetitive pseudo inverses of deflated H are the main contributors

to the algorithm complexity. In fact, as Hassibi in [28] reported, both of these procedures take up to 90% of the overall algorithm processing power.

Wubben in [39] has shown that cancellation of the detected symbol provides an increase in diversity order for the remaining symbols. This is the main strength of the VBLAST algorithm, compared to the ZF and MMSE algorithms, which provide no diversity gain. The choice of the nulling vector in step 1 corresponds to the ZF criteria. It suppresses the interference from the other antennas, but results in noise enhancement. The nulling vector can also be chosen according to MMSE criteria [40], which will result in a smaller noise enhancement compared to the ZF principle.

4.2.2.3 Simulations and discussions

Figure 17 shows a BER comparison for MLSD, ZF, MMSE, VBLAST ZF and VBLAST MMSE systems.

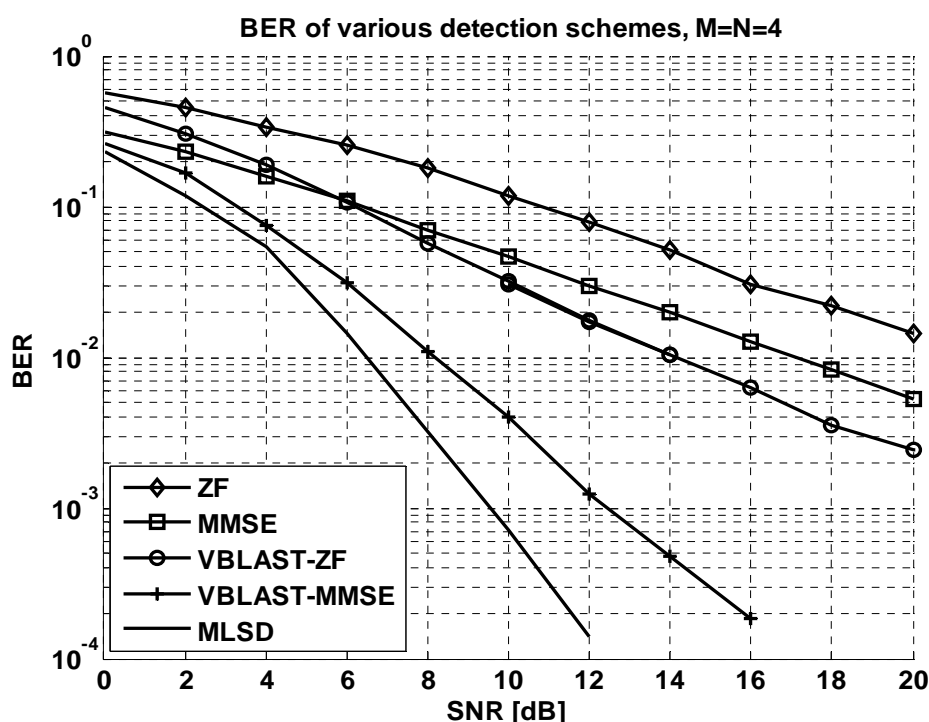


Figure 17. BER comparison, 4X4 system with channel known at the receiver and QPSK modulation.

MLSD has the best BER performance followed by VBLAST-MMSE. VBLAST-ZF outperforms MMSE for $\text{SNR} > 5\text{dB}$. The reason for this is the diversity gain provided by VBLAST. Finally, ZF exhibits the worst performance of all five schemes, as it does not provide any diversity gain and causes considerable noise enhancements.

VBLAST-type algorithms are considered a good choice for implementation due to their relatively low complexity and good BER performance. There was an extensive research into further complexity reduction of VBLAST algorithms. Hassibi in [28] has proposed to iteratively update the error covariance matrix (required for MMSE nulling) instead of repetitive inversion. The complexity of the algorithm has been reduced to $O(M^3)$.

VBLAST can also be restated in terms of the QR decomposition (QRD) [39]. QRD factors H into unitary matrix Q and upper triangular matrix R . Transmitted symbols then can be recovered via the back substitution method. A hard decision is performed on every recovered symbol, before feeding it to higher rows for the next step of the back substitution. The procedure is equivalent to the SIC method used in VBLAST [39] and repetitive channel inversions are avoided. Ordering, however, increases the complexity of the QRD-based algorithm [40], because $O(N^2/2)$ QRDs are required to check all the possible orderings to find the best one. Bohnke [40] has proposed a suboptimal Sorted QRD (SQRD) algorithm that performs sorting at each step of QRD. The algorithm is based on the modified Gramm Schmidt orthogonalisation procedure [41]. The complexity of the algorithm is $O(M^3)$.

4.2.3 Review of existing MIMO channel-tracking schemes

4.2.3.1 Motivation for tracking

In wireless packet data transmission systems it is necessary to reduce the packet size when the Doppler on the channel increases. This is because the training header containing the channel estimation information becomes outdated sooner. Unfortunately, short packets have reduced throughput because of the higher relative overheads associated with training, acknowledgements and inter-frame spacing. MIMO schemes such as VBLAST have to estimate many channels and so their training headers are generally very long. Therefore they are particularly vulnerable to Doppler-induced channel changes. A possible solution to this problem is to employ channel tracking, so that the equaliser in the receiver can be continually updated.

A generic data transmission frame structure is shown in figure 18 below. The first few symbols are dedicated pilots for channel estimation. The following symbols contain the data payload.

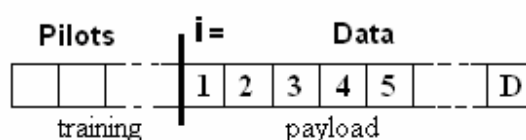


Figure 18. A generic frame structure consisting of a training preamble and D payload data symbols

The receiver acquires the channel estimate during the training session, then applies it to recover the D following transmitted data symbols, contained in a payload section of the frame. For the continuously fading channel scenarios, the actual channel value experienced by the i^{th} data symbol will be different from the measured channel estimate. The error, caused by the time

difference, will grow, since the measured channel estimate will become more outdated with time. Decreasing the time between successive training periods can reduce the error.

Hassibi et al in [42] has shown that the optimum number of training symbols in a preamble is equal to the number of transmitting antennas. Qifang et al in [43] have performed simulations using MIMO Jakes flat fading channel model at 2GHz carrier frequency and 41usec symbol time to show that the reduction of the training interval will reduce the throughput of the MIMO system. The amount of reduction is dependent on the number of antennas used and the fading rate of the channel. The paper also shows that employing channel tracking between successive training periods increases the training interval and improves the throughput of the system. However, these benefits of the channel tracking come at the expense of the increased complexity associated with the tracking algorithm implementation.

The growth of the Mean Squared Error (MSE) due to the use of the outdated fixed channel estimate at i^{th} instance can be defined as

$$MSE(\mathbf{e}_{\mathbf{H}}) = \frac{1}{LMN} * \sum_{k=1}^L \left| \mathbf{e}_{\mathbf{H}(i)k} \right|_F^2 \quad (44)$$

where $\mathbf{e}_{\mathbf{H}(i)}$ is the difference between the actual channel matrix at the time of the i^{th} symbol arrival and the initial channel estimate matrix obtained during the training session; $\left| \cdot \right|_F$ is a Frobenious norm; L is the number of ensemble repetitions; k is an ensemble index, and M and N are the number of transmit and receive antennas respectively.

Figure 19 plots a $MSE(\mathbf{e}_{\mathbf{H}})$ (in dB, relative to the normalised average channel power) of the 802.11n channels B, C, D, E and F in the 2X2 MIMO system.

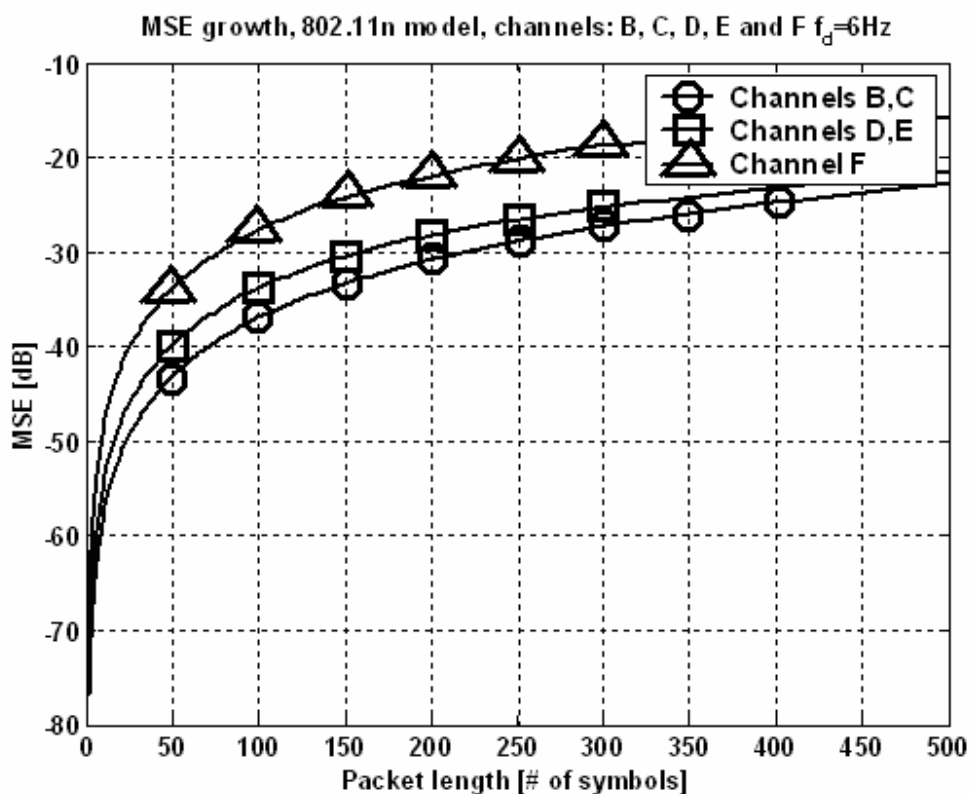


Figure 19. Channel MSE vs Time (symbols after training). Doppler as for 802.11n channels. The symbol period is $4\mu\text{s}$.

The D and E channels take into account fluorescent light. Their MSE, then, grows more quickly compared to the B and C channels. Channel F has a fast-moving component (40km/h) and has the worst performance of all the channel types.

Figure 19 can be used to estimate the number of data symbols between successive training periods. MSE should remain below the noise floor in the system before any additional training is needed. For the noise floor of -30dB , channels B and C can have packet lengths of up to 200 symbols. For the OFDM system (part of the 802.11n standard) with the symbol time of $4\mu\text{sec}$ it is equal to $800\mu\text{sec}$. Channels D and E would be able to tolerate 150 symbols (or $600\mu\text{sec}$ given the symbol time of $4\mu\text{sec}$) in the packet before MSE exceeds the -30dB threshold. Finally, channel F

can only have up to 75 symbols (or 300usec, given OFDM symbol time). Channel tracking can be employed to increase the packet length (and hence throughput of the system). The work in section 4.3 considers employing channel tracking for the F channel case. In the rest of the section, various existing tracking algorithms employed in MIMO are reviewed.

4.2.3.2 *Existing algorithms that employ MIMO channel tracking*

Decision Feedback Equalisation (DFE) is one popular approach employed for channel tracking and equalisation [1, 44-49]. The Equaliser coefficients are adjusted directly by the tracking algorithm. This approach is used in SISO systems to remove ISI effects caused by wideband multipath channels. The Feed Forward Filter (FFF) removes channel effects on the current symbol, while the Feed Back Filter (FBF) suppresses ISI effects from the previously detected symbols. Effectively the DFE tracks the channel inverse, H^{-1} . Figure 20 depicts the autocorrelation of the inverse channel and also the autocorrelation of the channel, H . A Jakes channel model is used in the simulation and elements of the MIMO channel matrices are independent identically distributed (iid).

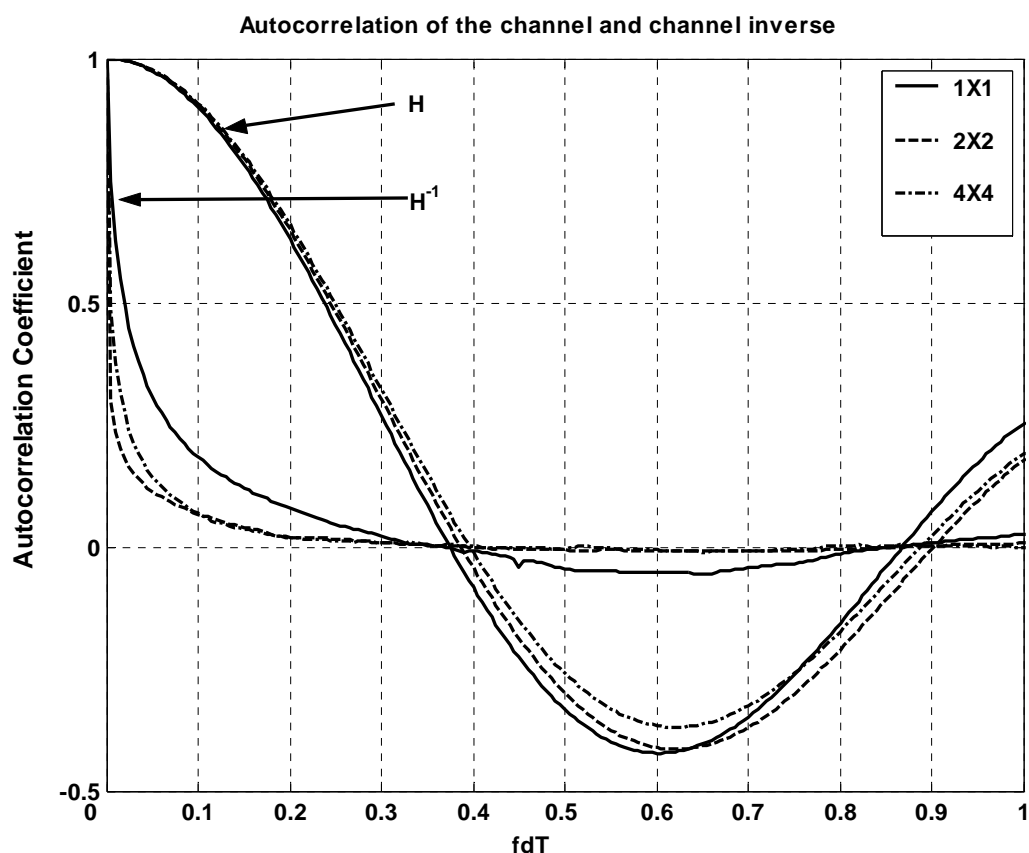


Figure 20. Autocorrelation of the channel and channel inverse for SISO, 2X2 MIMO and 4X4 MIMO channels

The peaky shape of the autocorrelation function of the H^{-1} in Figure 20 indicates high frequency content in the Power Spectral Density (PSD) of the inverse channel. It can be concluded, then that in SISO and MIMO systems the inverse channel exhibits dynamic variations far higher than the (non-inverted) channel. Therefore fast tracking algorithms such as the computationally intensive RLS or Kalman algorithms are generally needed [50]. The DFE can be used in MIMO systems not only to cancel ISI, but also to remove the interference from adjacent antennas. Komninakis, et al [51] presented one such scheme that uses the Kalman tracking algorithm to update

FFF and FBF coefficients. More details on using DFE in MIMO can be found in [52] and references therein. It was also shown in [53] that VBLAST can be reformulated as DFE.

Using this relation Choi et al [1] built a low complexity MIMO DFE algorithm for the flat fading MIMO channel, which removes concurrent interference from neighbouring antennas by applying SIC. The tracking of the feed forward coefficients is performed using the Sequential RLS (S-RLS) algorithm. The Feed Forward Filter (FFF) coefficients eliminate the channel effect (Nulling procedure in VBLAST) and the Feed Back Filter (FBF) coefficients suppress the interference from layers with already detected symbols (Cancellation procedure in VBLAST). VBLAST requires a pseudo-inverse calculation after each successive deflation of the channel to get the best filter coefficients for nulling. Choi, however, proposes to calculate the filter coefficients via an Order RLS (O-RLS) procedure [54]. The performance has also been compared to other existing SIC-MMSE algorithms and has provided superior BER results in a slow changing environment as well as in a channel with higher Doppler spread.

Alternatively the channel can be tracked and then the equaliser coefficients can be derived from the channel estimate. Some of the published work in the area is as follows.

- Sun Q., et al [43] used a high-order interpolation algorithm for channel tracking. Channel estimates were then used in a VBLAST equaliser.
- Roman T., et al [55] used the Kalman algorithm to track the channel in the MIMO OFDM system. The tracking is performed in the time domain and channel estimates are then converted into the frequency domain, where equaliser coefficients are calculated and equalisation is performed.
- Tong J., et al [56] used the LMS algorithm to track the time-varying channel for the space-frequency coded MIMO-OFDM system. The initial training sequence is used to obtain the

noisy channel estimate via Least Squares approximation of the known pilot symbols to the received data. Then this channel estimate is used to initialise the LMS tracking algorithm. P reference sub-carriers are included in each OFDM symbol. The LMS then iterates along these P sub-carriers to converge to the best channel estimate (in the MSE sense) at the current time instant.

There is a host of other MIMO tracking algorithms worth looking at [57-66].

When tracking is used with QRD-based detection algorithms, QRD can be performed every time a new channel estimate becomes available. This however will result in a high complexity per symbol, since QRD is a computationally expensive process ($O(M^3)$). The cost further increases in SIC systems, where the optimum detection order is required.

In this chapter we investigate the performance of decision-directed (DD) MIMO systems with two LMS based tracking strategies.

- The first strategy continuously tracks the channel matrix, H , but reduces the frequency of the QR decompositions. The Q and R matrices are then held fixed between successive updates. This will result in a complexity reduction at the expense of a growing error in channel estimate caused by the obsolete Q and R .
- The second strategy involves tracking the upper triangular matrix, R , rather than the channel matrix H , while holding the unitary matrix Q fixed between successive updates. The R matrix loses its upper triangular form with time because of the fixed Q .

Here, we assume no errors on the feedback path into the tracking algorithm for either strategy. The second strategy will result in a slower equalisation error growth, allowing a further decrease in frequency of the QR decompositions. In addition, the number of micro-rotations of the CORDIC algorithm can be reduced by taking the QRD of the tracked R matrix (which is nearly

upper triangular), rather than the H Matrix. This is due to the smaller average phase angles of the complex elements and column vectors.

Further, we compare the proposed strategies with MIMO-RLS-DFE scheme of [1], to see whether the benefit of the simpler and slower LMS algorithm outweighs the additional need for channel inversion. We show that despite the errors on the feedback path to the tracking algorithm, the second strategy still provides a superior effective channel. Unfortunately this fails to translate into better BER performance because of the errors on the first detection layer.

4.3 Using Upper Triangular Matrix Tracking to Reduce Complexity per Symbol in a Linear ZF MIMO System

4.3.1 System model

A simplified 2X2 base-band model of the MIMO-OFDM structure with QR detection and channel tracking is shown in figure 21.

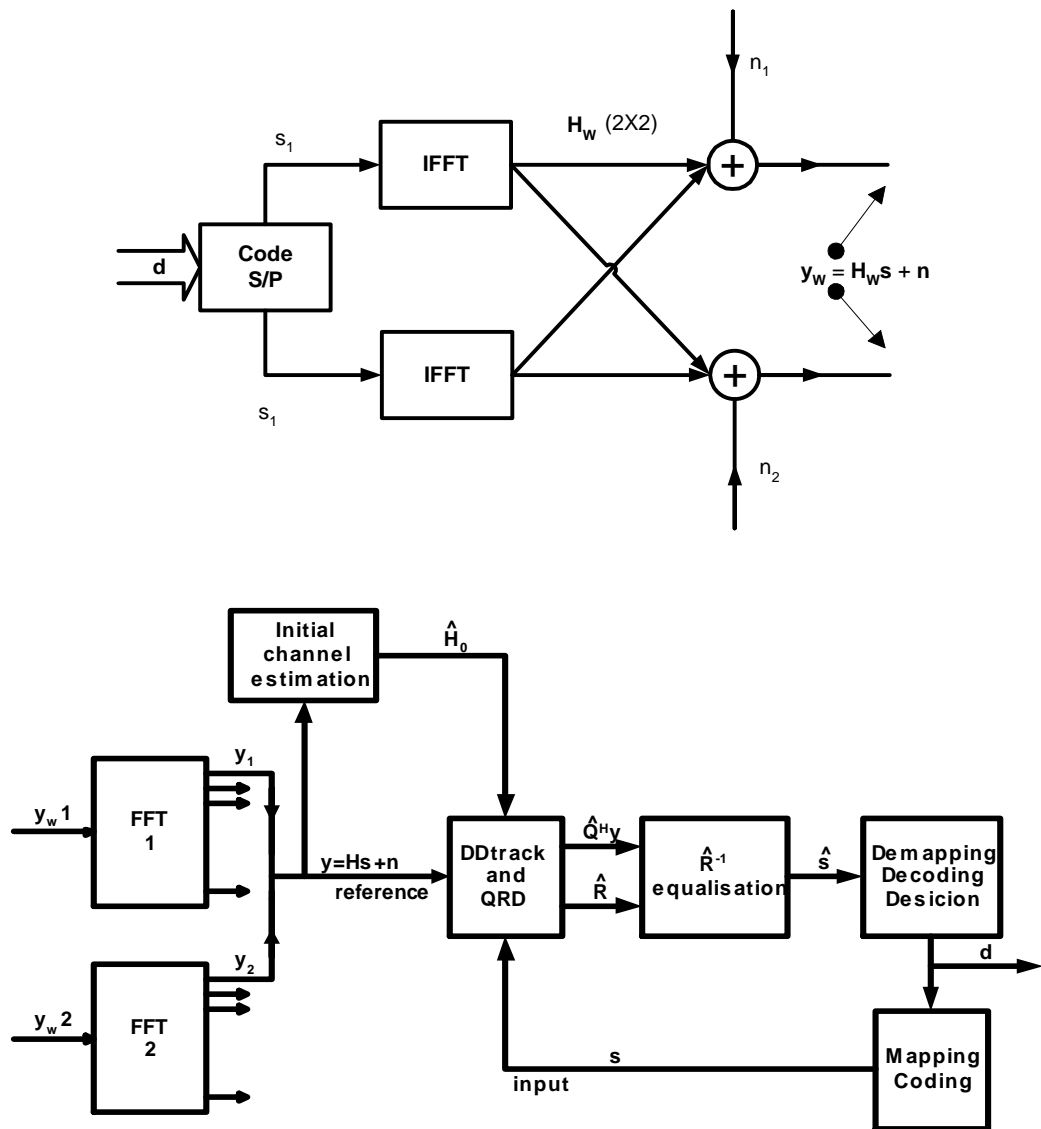


Figure 21. MIMO-OFDM structure with QR detection and channel tracking, initial channel estimates are obtained during the training session

The serial input data d is channel coded, interleaved and then converted to parallel streams s_1 and s_2 . After IFFTs, a wideband channel H_w corrupts the data and WGN is added at the receiver. The received wideband signal is represented by y_w . An N-point FFT at each receiver transforms the wideband channel, H_w , into N groups of 2X2 narrowband flat fading channels, H . $y = \begin{bmatrix} y1 \\ y2 \end{bmatrix}$ is the output signal of one such group.

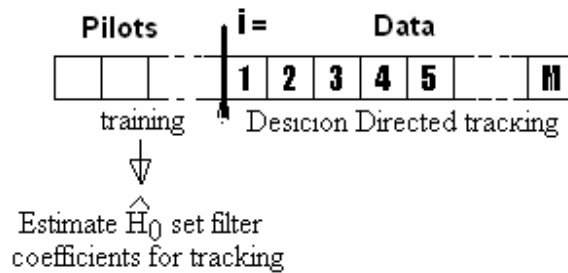


Figure 22. General packet structure employed in wireless LANs

The data transmission packet consists of a header of known training symbols followed by a data payload of M MIMO encoded symbols (figure 22). The training symbols are used for channel estimation and setting the initial conditions of the tracking adaptive filter. A decision-directed algorithm then takes over and tracks the channel, using y as its reference signal. This is performed in the “DD track and QRD” block of figure 21. The LMS algorithm used in this work performs well in a slow-changing environment. It has low complexity and is robust. The decision-directed structure eliminates the need for *a priori* information. After the channel has been estimated in this way, the $\hat{\mathbf{Q}}$ and $\hat{\mathbf{R}}$ matrices are obtained through QR decomposition and then used to equalise the channel for the received data symbols, y . QR equalisation is based on the following identity

$$\hat{\mathbf{Q}}^H * \mathbf{y} = \hat{\mathbf{R}} * \hat{\mathbf{s}} \quad (45)$$

Since $\hat{\mathbf{R}}$ is an upper triangular matrix, symbol recovery of the symbol estimate, $\hat{\mathbf{s}}$ is possible via back substitution in (45). Finally, de-interleaving, decoding and decision are performed to get the original data, \mathbf{d} . The data is re-coded for the feedback path and then used as an input, \mathbf{s} , to the LMS channel-tracking algorithm.

In this work we will consider low Doppler channels as specified for wireless local area networks (WLAN). These channels generally assume stationary terminals but moving scatterers. The new 802.11n standard has specified six such channels. The most aggressive of these, in terms of Doppler, is channel F, which assumes scatter velocities of 1.2km/hr for all scatterers except for one, which moves at 40km/hr. This channel will be used for this work. A complete list of the simulation parameters is shown below:

- The IEEE 802.11n type F channel model @ 5.27GHz
- A 4 μ sec OFDM symbol period (3.2usec with a cyclic prefix of 0.8usec)
- The number of sub-carriers, N=64
- A 20MHz system bandwidth
- QPSK modulation
- No hardware imperfections, perfect synchronisation and no frequency offset

All the variables with ' $\hat{\cdot}$ ' denote the estimated parameters. Also \mathbf{R} denotes the strictly upper triangular matrix while \mathbf{A}_R (used from section 4.3.2.2 onwards) represents an upper triangular matrix that loses its upper triangular structure in the course of tracking.

4.3.2 Evaluation of tracking schemes

4.3.2.1 Tracking the channel matrix H

An expansion of the "DD track and QRD" block of figure 21 is shown in figure 23 for the channel-tracking case. The LMS algorithm uses a decision-directed structure to track the channel matrix \mathbf{H} . The recoded and remapped signal s forms the input to the LMS and the received signal y (appropriately delayed) is used as reference. The LMS then adjusts the coefficients of $\hat{\mathbf{H}}$ to

minimise the error signal $\left| y - \hat{\mathbf{H}}^* s \right|$.

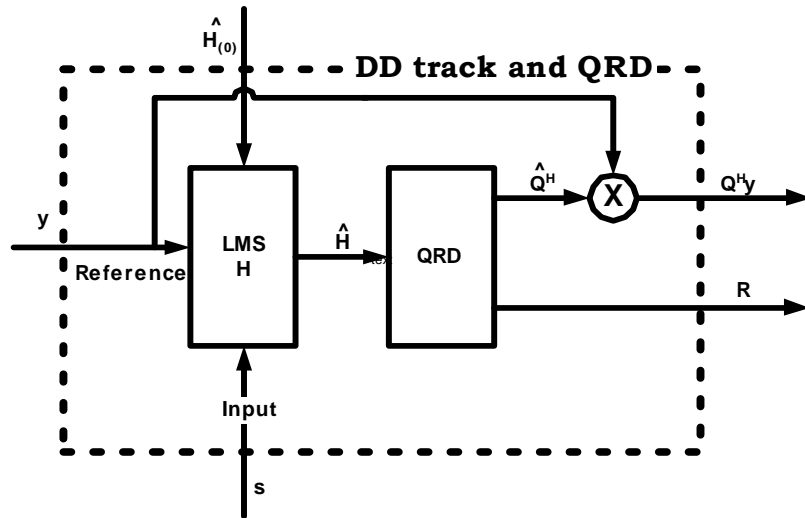


Figure 23. Decision-directed tracking and QR decomposition for the channel-tracking case

The matrix $\hat{\mathbf{H}}(\mathbf{i})$ represents the channel estimate matrix at the i^{th} time instance. It can be decomposed,

$$\hat{\mathbf{H}}(\mathbf{i}) = \hat{\mathbf{Q}}(\mathbf{i})^* \hat{\mathbf{R}}(\mathbf{i}) \quad (46)$$

from which the term $\hat{\mathbf{Q}}^H \mathbf{y}$ can be obtained. If the QR decomposition is not performed at every time instance to reduce complexity, the matrices $\hat{\mathbf{Q}}$ and $\hat{\mathbf{R}}$ become outdated. Outdated $\hat{\mathbf{Q}}$ and $\hat{\mathbf{R}}$ values will cause an error in the equalisation that increases, as the estimates gets older. The error matrix, $\mathbf{er}_{\mathbf{H}(i)}$, can be written as follows

$$\mathbf{er}_{\mathbf{H}(i)} = \mathbf{H}_{(i)} - \hat{\mathbf{Q}}_{(i-n)}^* \hat{\mathbf{R}}_{(i-n)} \quad (47)$$

Here $\mathbf{H}_{(i)}$ is the actual channel matrix at the time instance, i , while $\hat{\mathbf{Q}}_{(i-n)}$ and $\hat{\mathbf{R}}_{(i-n)}$ are unitary and upper triangular matrices obtained n time instances earlier, from the LMS estimate $\hat{\mathbf{H}}_{(i-n)}$. Obviously, when $n = 0$ (QR decomposition is performed at every time instance) $\mathbf{er}_{\mathbf{H}(i)}$ will represent the tracking error of the LMS algorithm. When $n=(i-1)$ the QR decomposition is performed only once, directly after the training sequence, and so $\mathbf{er}_{\mathbf{H}(i)}$ will represent the error due to Doppler variations in the channel. The average error power per element of this matrix is described by (44).

The diagrammatical representation of the indexing is shown below

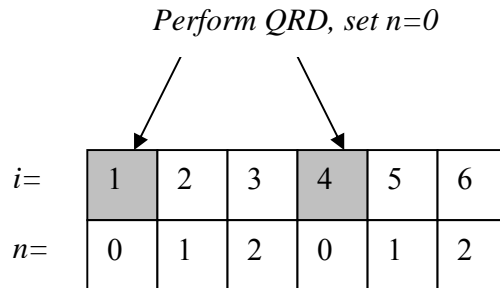


Figure 24. An example of the indexing, QRD performed every 3rd symbol.

4.3.2.2 Tracking the upper triangular matrix

The expansion of the "DD track and QRD" block in figure 21 for the upper triangular matrix-tracking scenario is shown in figure 25.

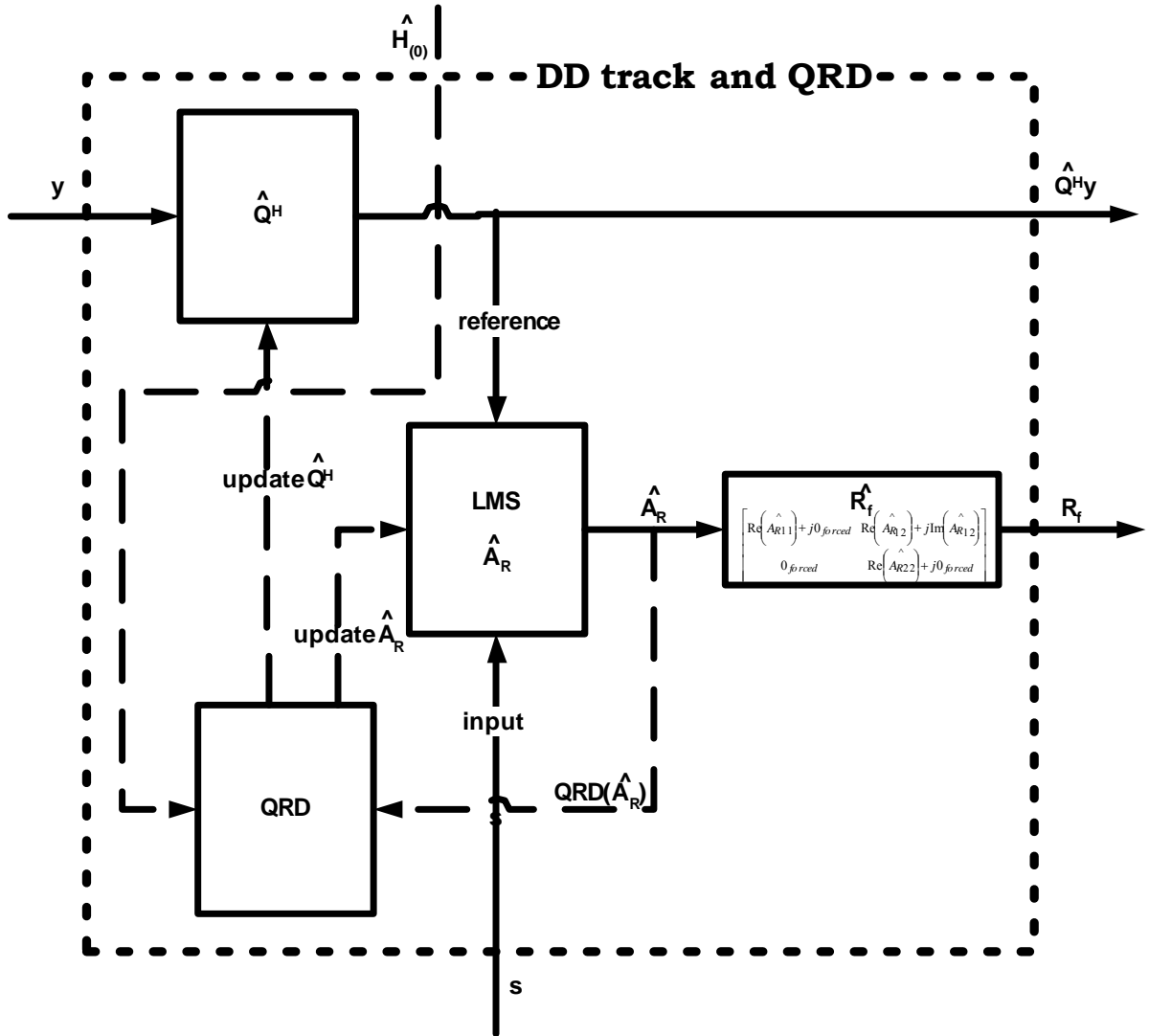


Figure 25. Decision-directed tracking and QR decomposition for the upper triangular matrix-tracking scenario

The channel matrix $\hat{\mathbf{H}}_{(0)}$ is obtained immediately after the initial training period, and the QR decomposition is performed to initialise the $\hat{\mathbf{Q}}^H$ and $\hat{\mathbf{A}}_{\mathbf{R}}$ blocks. In this scenario, the LMS algorithm tracks the $\mathbf{A}_{\mathbf{R}}$ matrix only. (Note, the \mathbf{Q} matrix is held fixed until it is updated by the next QR decomposition). At any time instance the channel matrix \mathbf{H} can be presented as

$$\mathbf{H}_{(i)} = \mathbf{Q}_{(i-n)} * \mathbf{A}_{\mathbf{R}(i)} \quad (48)$$

Here $\mathbf{H}_{(i)}$ is the actual channel matrix at the i^{th} time instance, $\mathbf{Q}_{(i-n)}$ is a unitary matrix obtained n time instances ago (from $\mathbf{H}_{(i-n)}$), and $\mathbf{A}_{\mathbf{R}(i)}$ is generally a non-upper triangular matrix. $\mathbf{A}_{\mathbf{R}(i)}$ has the upper triangular form when $n=0$, immediately after a QR decomposition. As n increases $\mathbf{Q}_{(i-n)}$ becomes more outdated, hence $\mathbf{A}_{\mathbf{R}(i)}$ has to change to compensate for the changing channel. As a result $\mathbf{A}_{\mathbf{R}(i)}$ has non-zero components introduced below the main diagonal as well as non-real components on the main diagonal.

The LMS tracking configuration is shown in figure 26. The key difference between this and the previous sub-section (4.3.2.1) is that the reference signal for the LMS algorithm is now taken after the $\hat{\mathbf{Q}}^H$ processing block.

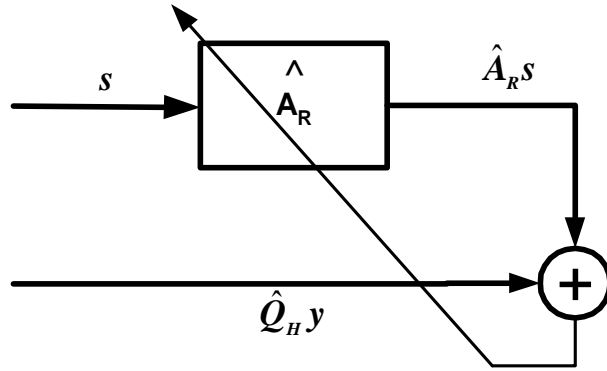


Figure 26. LMS configuration for tracking the \mathbf{A}_R matrix

If $\hat{\mathbf{A}}_{R(i)}$ is an estimate of an upper triangular matrix \mathbf{A}_R at the time instance i , then the error $\mathbf{er}_{(i)}$ due to tracking and noise can be expressed as

$$\mathbf{er}_{(i)} = \mathbf{Q}_{(i-n)}^H * \mathbf{y}_{(i)} - \hat{\mathbf{A}}_{R(i)} * \mathbf{s}_{(i)} \quad (49)$$

substituting from equation 49

$$\begin{aligned} \mathbf{er}_{(i)} &= \mathbf{Q}_{(i-n)}^H * \mathbf{Q}_{(i-n)} * \mathbf{A}_{R(i)} * \mathbf{s}_i - \hat{\mathbf{A}}_{R(i)} * \mathbf{s}_{(i)} + \mathbf{Q}_{(i-n)}^H * \mathbf{n}_{(i)} \\ \mathbf{er}_{(i)} &= \left(\mathbf{Q}_{(i-n)}^H * \mathbf{Q}_{(i-n)} * \mathbf{A}_{R(i)} - \hat{\mathbf{A}}_{R(i)} \right) * \mathbf{s}_{(i)} + \mathbf{Q}_{(i-n)}^H * \mathbf{n}_{(i)} \end{aligned} \quad (50)$$

This error signal is used to update the LMS tracking algorithm [67].

The non-upper triangular $\hat{\mathbf{A}}_{R(i)}$ matrix is not suitable for the back substitution process used in the \mathbf{R}^{-1} equalisation block of figure 21. A modified copy of $\hat{\mathbf{A}}_{R(i)}$ is needed. In this modification all the non-zero imaginary elements on the main diagonal and all the elements below the main

diagonal are set to zero. The created upper triangular matrix $\hat{\mathbf{R}}_f$ is used for back substitution in figure 25. The forcing to zero operation, however, creates an additional error.

The effective channel estimate, $\hat{\mathbf{H}}_{f(i)}$ with all errors included (zero-forcing and tracking) is defined as

$$\hat{\mathbf{H}}_{f(i)} = \hat{\mathbf{Q}}_{(i-n)} * \hat{\mathbf{R}}_{f(i)} \quad (51)$$

The new error matrix becomes

$$\mathbf{er}_{R(i)} = \mathbf{H}_{(i)} - \hat{\mathbf{H}}_{f(i)} \quad (52)$$

Expanding (52) using equation (51) gives

$$\mathbf{er}_{R(i)} = \mathbf{Q}_{(i-n)} * \mathbf{A}_{R(i)} - \hat{\mathbf{Q}}_{(i-n)} * \hat{\mathbf{R}}_{f(i)} \quad (53)$$

When the power of this error grows beyond a threshold, set by the designer, the QR decomposition (QRD block in figure 25) can be performed on $\hat{\mathbf{A}}_{R(i)}$ to bring it back to upper triangular form and update the unitary matrix \mathbf{Q} , as shown below

$$\hat{\mathbf{H}}_{(i)} = \hat{\mathbf{Q}}_{(i-n)} * \hat{\mathbf{A}}_{R(i)} = \hat{\mathbf{Q}}_{(i-n)} * \mathbf{QRD} \left(\hat{\mathbf{A}}_{R(i)} \right) = \hat{\mathbf{Q}}_{(i-n)} * \mathbf{Q}_{(i)}' * \mathbf{R}_{(i)}' \quad (54)$$

In (55) $\hat{\mathbf{Q}}_{(i-n)} * \mathbf{Q}_{(i)}'$ forms a new unitary matrix and $\mathbf{R}_{(i)}'$ is the new upper triangular matrix that updates the $\hat{\mathbf{A}}_R$ value in the LMS tracking block of figure 25.

4.3.2.3 Simulation results

Figure 27 depicts the MSE performance of the two tracking scenarios as a function of the number of data symbols in a packet. Two conditions are shown for each scenario: with QR

decomposition performed on every symbol, and with QR decomposition performed on the initial channel estimate $\hat{\mathbf{H}}_{(0)}$ only. A 2X2 normalised channel matrix is used, at a Doppler frequency of 48Hz. Such a high Doppler frequency is chosen to show the asymptotic behaviour of the curves. There is no noise in the system.

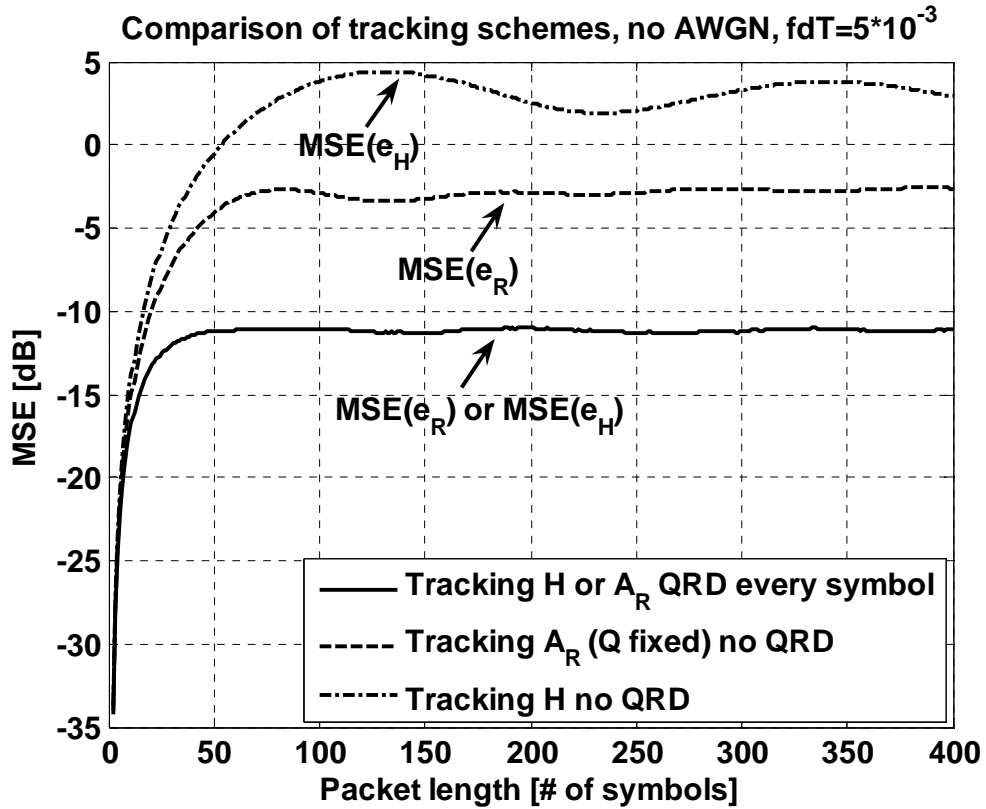


Figure 27. Comparison of tracking performance, perfect channel estimation and hence perfect Q and R is assumed at the first symbol.

Some important observations can be made based on this figure. Both tracking schemes H and A_R perform equally when QR decomposition is performed at every time instance (bottom line). In both cases the error floor is due to the tracking and misadjustment of the LMS algorithm. To show the equivalence, we can write

$$\mathbf{A}_R = \mathbf{Q}^H * \mathbf{H} \quad (55)$$

Taking the Frobenious norm of both sides gives

$$|\mathbf{A}_R|_F = |\mathbf{Q}^H * \mathbf{H}|_F \quad (56)$$

Here \mathbf{Q} is a unitary matrix, so the magnitudes of \mathbf{H} and \mathbf{A}_R are equal.

The error growth in the \mathbf{A}_R tracking case (second line from the bottom, figure 27) is solely due to

the conversion of $\hat{\mathbf{A}}_R$ to $\hat{\mathbf{R}}_f$ for equalisation using back substitution. For the case of a 2X2 matrix:

$$\hat{\mathbf{A}}_R = \begin{bmatrix} r_{11r} + jr_{11i} & r_{12r} + jr_{12i} \\ r_{21r} + jr_{21i} & r_{22r} + jr_{22i} \end{bmatrix} \text{ and } \hat{\mathbf{R}}_f = \begin{bmatrix} r_{11r} + j0 & r_{12r} + jr_{12i} \\ 0 + j0 & r_{22r} + j0 \end{bmatrix} \quad (57)$$

Then the instantaneous error matrix due to introducing zeros in $\hat{\mathbf{A}}_R$ can be written

$$\left(\hat{\mathbf{A}}_R - \hat{\mathbf{R}}_f \right) = \begin{bmatrix} jr_{11i} & 0 \\ r_{21r} + jr_{21i} & jr_{22i} \end{bmatrix} \quad (58)$$

The elements in (59) are reset to zero every time QR decomposition is performed on $\hat{\mathbf{A}}_R$.

Given that $\hat{\mathbf{A}}_R$ is normalised to have an average total power of unity (equivalent to the channel), it can be easily shown that the maximum average power of this error matrix reaches -3dB of the normalised power. This is indeed the upper bound for the second line from the bottom in figure 27.

The top line in Figure 27 shows the difference between the current channel estimate, $\hat{\mathbf{H}}_{(i)}$, and the original current estimate, $\hat{\mathbf{H}}_{(i-n)}$ taken n instances earlier. The error matrix can be presented

as

$$\mathbf{e}_{\mathbf{H}(n)} = \hat{\mathbf{H}}_{(i)} - \hat{\mathbf{H}}_{(i-n)} = \begin{bmatrix} d\mathbf{h}_{11r} + j d\mathbf{h}_{11i} & d\mathbf{h}_{21r} + j d\mathbf{h}_{21i} \\ d\mathbf{h}_{12r} + j d\mathbf{h}_{12i} & d\mathbf{h}_{22r} + j d\mathbf{h}_{22i} \end{bmatrix}$$

Where

$$d\mathbf{h}_{ij} = (\mathbf{h}_{ij(i)} - \mathbf{h}_{ij(i-n)})$$

(59)

Here, h_{ij} can be either real or an imaginary and $1 \leq i \leq 2$, $1 \leq j \leq 2$

Assuming all four complex coefficients of (60) have identical statistics and the channel matrix is again normalised to have an average power of unity, it can be shown that the average power per element in $\mathbf{e}_{\mathbf{H}(n)}$ is given by:

$$\lim_{n \rightarrow \infty} E \left[\left(\mathbf{e}_{\mathbf{H}(n)} \right)^2 \right] = 3dB \text{ of the normalised power} \quad (60)$$

This is the upper bound for the top line in figure 27.

4.3.3 Saving power through QR decomposition repetition rate reduction

Figure 28 depicts a channel-tracking model where the frequency of QR decompositions is adjusted to maintain the average MSE below a set threshold. This will minimise the power consumption.

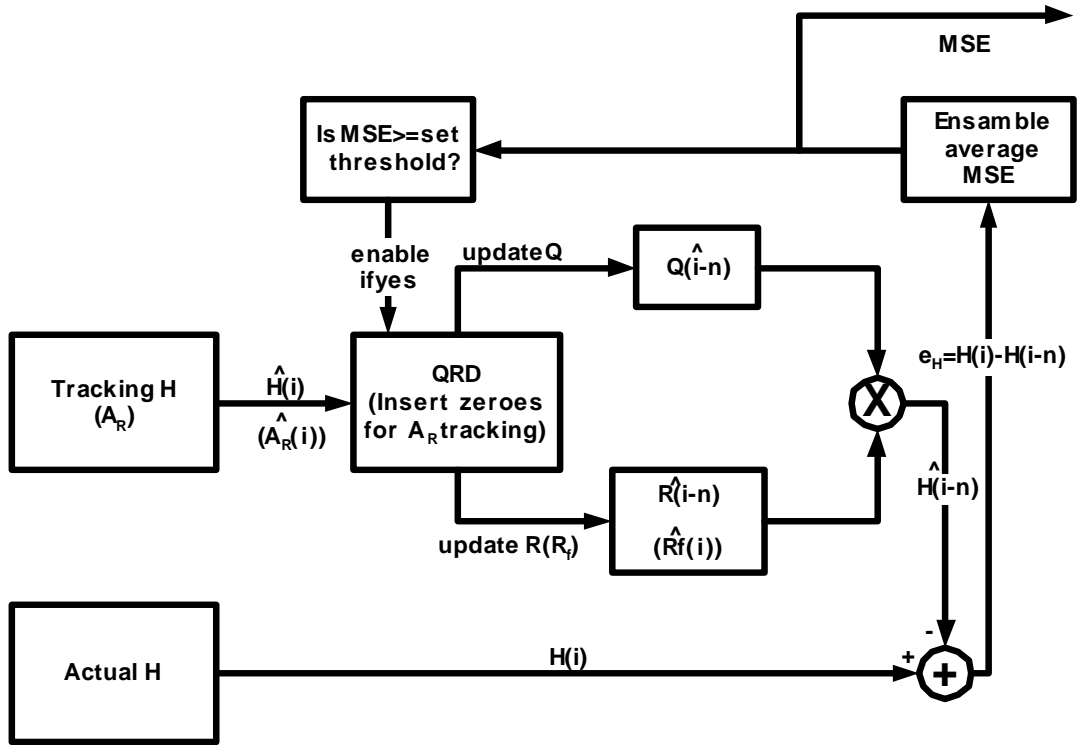


Figure 28. The system model used to evaluate the channel or upper triangular matrix-tracking schemes

The QRD block is invoked and n set equal to i , when the MSE exceeds a set threshold; otherwise the outdated $\hat{\mathbf{Q}}_{(i-n)}$ and $\hat{\mathbf{R}}_{(i-n)}$ values are used. In the simulations the above model will be used to generate three MSE curves representing different scenarios.

In the first scenario the QRD block is used once only; immediately after the training session. In the second scenario, the threshold for invoking a QRD is set at 6dB below the operating noise power level, N_o . This means that the implementation loss associated with channel estimation errors

$$\text{is bounded at } -10 * \log_{10} \frac{N_o}{N_o + \frac{N_o}{4}} \approx 1\text{dB}.$$

And finally in the last scenario QR decomposition is performed on every single channel estimate. This curve represents the tracking floor of the LMS algorithm (assuming negligible QR decomposition errors). There is some compromise here, since the LMS feedback coefficient, μ , can be adjusted to lower this floor, but at the expense of slower convergence. The value of $\mu = 0.1$ chosen in this simulation takes 8 symbols to bring the MSE below the (No-6dB) threshold.

The same system model is used for the upper triangular matrix tracking (figure 28), except the variables in parentheses are now used. Two additional scenarios are considered. The fourth scenario only performs one QR decomposition after training. In this case $\hat{\mathbf{R}}_{\mathbf{f}(i)}$ is obtained through inserting zeros into the tracked matrix $\hat{\mathbf{A}}_{\mathbf{R}(i)}$. The fifth scenario performs the QRD when the MSE is above the set threshold. The update of $\hat{\mathbf{A}}_{\mathbf{R}(i)}$ and $\hat{\mathbf{Q}}_{(i)}$ is performed according to (55).

Figure 29 presents MSE comparisons of the five scenarios for both tracking schemes in the presence of additive white Gaussian noise of -30dB . The pilots have the same SNR as the data and the environment is slowly changing with a Doppler frequency of 6Hz, as specified in the channel model [22].

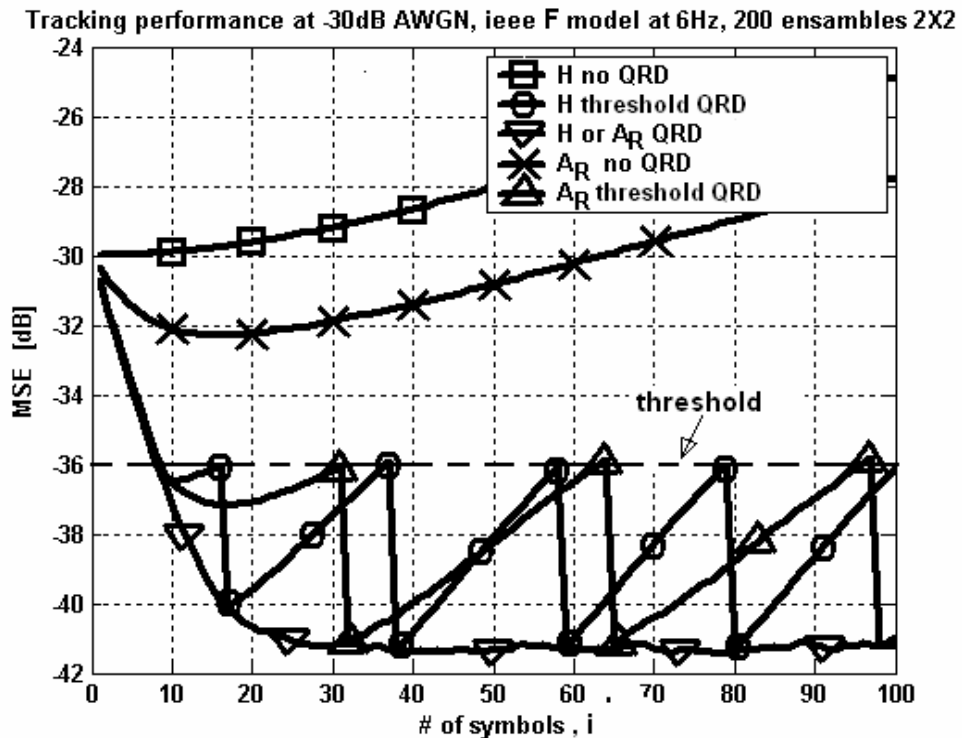


Figure 29. MSE vs. packet length comparison of various scenarios in the presence of AWGN and $f_d=6\text{Hz}$

A QRD is taken immediately after training for all curves. The top curve “H no QRD” has no further updates of the Q and R matrices, and so the MSE (48) steadily increases with time. The second curve from the top “ A_R no QRD” also does no further QRDs, but the partial tracking of the \mathbf{R} Matrix initially improves the MSE for the first 15 data symbols, before the error growth in the zeroed elements (59) starts to dominate. The best results come from when the QRD is executed after every symbol “H or A_R QRD” and this forms a lower bound to the MSE. These three lines are identical to the curves in figure 27, except for the more realistic lower Doppler frequency suggested by the IEEE802.11n channel model. The last two curves show the threshold mode of operation. Savings in QRDs occurs after MSE drops below the threshold of -36dB. The oscillatory motion is constrained between the threshold and lower MSE bound. It can be observed that after the LMS algorithm has converged, it takes about 10 symbols longer for the “ A_R threshold QRD” line to reach

the error threshold than for the “H threshold QRD” line. The slower divergence of A_R allows a reduced number of operations per symbol without additional sacrifice in the performance.

If the A_R tracking and H tracking scenarios require n and m symbols respectively to degrade to a given MSE, the ratio $\frac{m}{n}$ will express the complexity gain of the A_R tracking scheme over the channel-tracking scheme. Table 1 presents the gain in the complexity of the A_R tracking scheme for the various SNR cases. The IEEE 802.11n channel “F” model is used.

SNR [dB]	Target MSE [dB]	Symbols between QR		Ratio A_R/H [m/n]
		Tracking H [n]	Tracking A_R [m]	
20	-26	97	140	1.44
22	-28	74	108	1.46
24	-30	56	82	1.46
26	-32	43	64	1.49
28	-34	32	48	1.5
30	-36	24	36	1.5

Table 1 Number of symbols between QR decompositions during which the target MSE is reached for both tracking schemes at various SNR levels

The first column of table 1 gives the SNR level, and the target MSE is shown in the second column. The last column shows the gain in the complexity that can be achieved by tracking the upper triangular matrix. It is possible to have up to 1.5 times fewer operations per symbol without sacrificing performance.

4.3.4 Threshold detection in a practical system

Threshold detection forms an important component of the computation-saving techniques proposed in this work. Errors described by (47) and (53) are used to calculate Mean Squared Error

needed for the threshold calculations. For simulation purposes, the actual channel is used as a reference in these equations (also depicted in figure 28).

In the practical case the actual channel value is not available. However, it is possible to obtain the required error, using $\hat{\mathbf{H}}$ or $\hat{\mathbf{A}}_{\mathbf{R}}$ (depending on the tracking scheme chosen) as a reference. The next two subsections show how the error is obtained for the channel-tracking case and for the $A_{\mathbf{R}}$ tracking case respectively.

4.3.4.1 Channel tracking with threshold detection

For the channel-tracking case the error $er_{H(i)}$ in (47) can be rewritten as

$$\mathbf{er}_{\mathbf{H}(i)} = \mathbf{H}(i) - \hat{\mathbf{H}}(i-n) = \left[\left(\mathbf{H}(i) - \hat{\mathbf{H}}(i) \right) + \left(\hat{\mathbf{H}}(i) - \hat{\mathbf{H}}(i-n) \right) \right] \quad (61)$$

Mean Squared Error of (61) is then

$$MSE_{H(i)} = E \left[\left[\left(\mathbf{H}(i) - \hat{\mathbf{H}}(i) \right) + \left(\hat{\mathbf{H}}(i) - \hat{\mathbf{H}}(i-n) \right) \right]^2 \right] \quad (62)$$

where $E \left[\square^2 \right]$ denotes an ensemble average per matrix element.

Assuming that the two different components in (62) are uncorrelated

$$MSE_{H(i)} = E \left[\left| \mathbf{H}(i) - \hat{\mathbf{H}}(i) \right|^2 \right] + E \left[\left| \hat{\mathbf{H}}(i) - \hat{\mathbf{H}}(i-n) \right|^2 \right] \quad (63)$$

The first part of (63) can be obtained from the LMS tracking error

$$\begin{aligned}
er_{LMS}(i) &= \mathbf{y}(i) - \hat{\mathbf{H}}(i) * \mathbf{s}(i) = \mathbf{H}(i) * \mathbf{s}(i) + \mathbf{n}(i) - \hat{\mathbf{H}}(i) * \mathbf{s}(i); \\
er_{LMS}(i) &= \left(\mathbf{H}(i) - \hat{\mathbf{H}}(i) \right) * \mathbf{s}(i) + \mathbf{n}(i)
\end{aligned} \tag{64}$$

With normalised signal power the expected value of er_{LMS} is

$$MSE_{LMS}(i) = E \left[\left| \mathbf{H}(i) - \hat{\mathbf{H}}(i) \right|^2 \right] + E \left[|\mathbf{n}|^2 \right] \tag{65}$$

After subtracting the biasing term $E \left[|\mathbf{n}|^2 \right]$ from the derived MSE, the expression can be used in (63).

The second part of (63) is calculated from readily available $\hat{\mathbf{H}}_{(i-n)}$ (saved every time QR decomposition is performed) and $\hat{\mathbf{H}}(i)$, the LMS channel estimate.

4.3.4.2 Upper triangular matrix tracking with threshold detection

In the upper triangular matrix-tracking case:

$$MSE_{R(i)} = E \left[\left| \mathbf{Q}_{(i-n)} * \mathbf{A}_{\mathbf{R}(i)} - \hat{\mathbf{Q}}_{(i-n)} * \hat{\mathbf{R}}_{\mathbf{f}(i)} \right|^2 \right] \tag{66}$$

Since $\mathbf{Q}_{(i-n)}$ and $\hat{\mathbf{Q}}_{(i-n)}$ are unitary (66) can be rewritten

$$MSE_{R(i)} = E \left[\left| \mathbf{A}_{\mathbf{R}(i)} - \hat{\mathbf{R}}_{\mathbf{f}(i)} \right|^2 \right] \tag{67}$$

Equation (67) can be expanded into

$$MSE_{R(i)} = E \left[\left[\left(\mathbf{A}_{R(i)} - \hat{\mathbf{A}}_{R(i)} \right) + \left(\hat{\mathbf{A}}_{R(i)} - \hat{\mathbf{R}}_{f(i)} \right) \right]^2 \right] \quad (68)$$

Then, assuming the two parts in (68) are uncorrelated

$$MSE_{R(i)} = E \left[\left| \mathbf{A}_{R(i)} - \hat{\mathbf{A}}_{R(i)} \right|^2 \right] + E \left[\left| \hat{\mathbf{A}}_{R(i)} - \hat{\mathbf{R}}_{f(i)} \right|^2 \right] \quad (69)$$

Following the same approach as in the channel-tracking case, it is easy to show that the first part of (69) is actually the LMS tracking error without biasing noise term and the difference in the second part of (69) is evaluated from the available $\hat{\mathbf{A}}_{R(i)}$ and $\hat{\mathbf{R}}_{f(i)}$.

4.3.4.3 Block diagram and evaluation of the threshold detector

The block diagram of a threshold detector is presented in figure 30

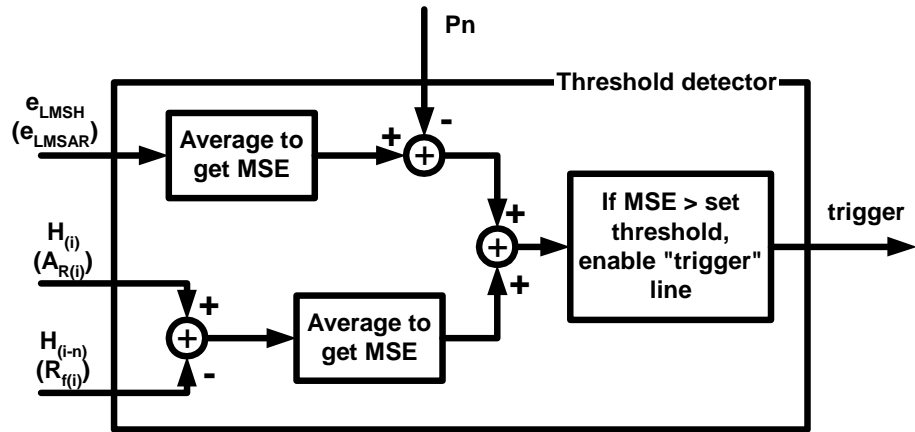


Figure 30. Threshold detector block diagram

The values in brackets on the input lines to the threshold detector apply for the upper triangular matrix-tracking case. P_n is the noise power (a biasing term). The trigger line is connected to the QR decomposition blocks in figures 23 and 25.

Figure 31 shows the performance of most of the scenarios described in the previous section with identical conditions. For clarity of presentation, the channel-tracking case is excluded. Instead, the MSE of the threshold detector in the A_R tracking case is shown.

Tracking performance at -30dB AWGN, IEEE F model at 6Hz, 200 ensembles 2X2

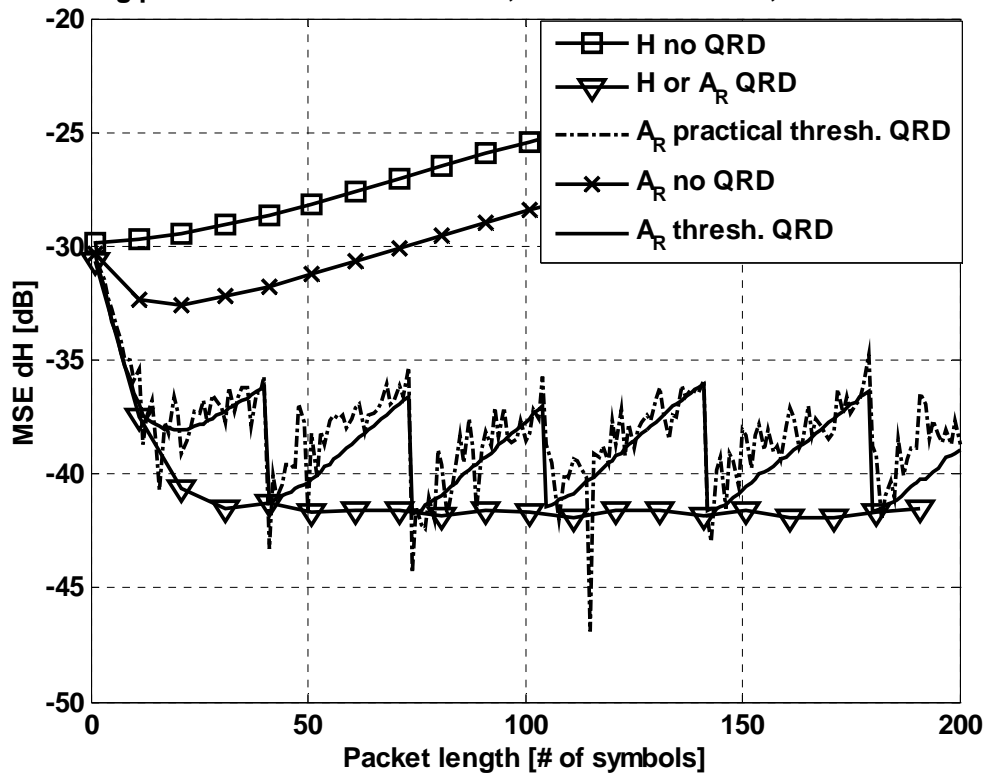


Figure 31. MSE vs. packet length comparison using threshold detector

The " A_R practical thresh. QRD" line has fluctuations due to the noisy LMS error. Using more samples for averaging can reduce the power of these fluctuations. In practice, averaging causes a time delay that has to be accommodated in the system.

4.3.5 CORDIC-based QR decomposition

QR decomposition using the Givens rotation method is commonly based on the CORDIC algorithm. The latter performs a fixed number of micro-rotations. For the A_R tracking case, however, the initial angles by which complex elements and column vectors of \mathbf{A}_R are rotated are often small. This section presents and explains the necessary CORDIC algorithm modifications to take advantage of these smaller angles.

4.3.5.1 Using CORDIC to perform QR decomposition

The Vectoring and rotation modes of the CORDIC operation are of interest [68].

In the vectoring mode an arbitrary vector $\mathbf{v} = \begin{bmatrix} x \\ y \end{bmatrix}$ with $\tan(\alpha) = \frac{y}{x}$ is rotated towards the x-axis

using a set of rotation matrices, called micro-rotations. The algorithm is presented in (70)

$$\mathbf{q}_m = \frac{1}{\sqrt{1+2^{-2s*m}}} \begin{bmatrix} 1 & d*2^{-m} \\ -d*2^{-m} & 1 \end{bmatrix} \quad 0 \leq m \leq K, \quad m \in \mathbb{N}$$

$$d = \text{sign}(x_m) * \text{sign}(y_m) \quad (70)$$

$$\mathbf{v}_{m+1} = \mathbf{q}_m * \mathbf{v}_m$$

x_m and y_m are x and y components of \mathbf{v} at the m^{th} iteration and \mathbf{v}_m is vector \mathbf{v} at m^{th} iteration; \mathbf{q}_m is an orthogonal matrix that rotates the vector \mathbf{v}_m by $\tan^{-1}(2^{-m})$ angle. Since 2^{-m} , $0 \leq m \leq K$, $m \in \mathbb{N}$ is a converging sequence, \mathbf{v}_m is bound to align with the x-axis to within a 'set angular tolerance' given by $\tan^{-1}(2^{-K})$. After K micro-rotations, the algorithm is stopped. Symbol d in (71) indicates the direction of the next micro-rotation. The square root term in front of the matrix in (71) is known as the scaling factor. It quickly converges to 1.0 and there is no need to calculate it after $n_b/2$ iterations, where n_b is the processing wordlength, since the value of 2^{-2s*m} drops below the

quantisation noise floor. The product of all the scaling factors is normally pre-calculated, stored, and applied only once after the final iteration.

In the rotational mode the vector \mathbf{v} is rotated by a preset angle.

$$\begin{aligned}
 q_m &= \frac{1}{\sqrt{1+2^{-2s^*m}}} \begin{bmatrix} 1 & d * 2^{-m} \\ -d * 2^{-m} & 1 \end{bmatrix} \quad 0 \leq m \leq K, \quad m \in \mathbb{N} \\
 d &= \text{sign}(z_m) \\
 z_{m+1} &= z_m - d * \alpha_m, \quad \alpha_m = \tan^{-1}(2^{-m}) \\
 v_{m+1} &= q_m * v_m
 \end{aligned} \tag{71}$$

$z=z_0$ is the preset angle. In (71), z_{m+1} contains the residual angle that must be driven to zero, and d indicates the direction of the next micro-rotation. When z_{m+1} reaches a ‘set angular tolerance’ of $\tan^{-1}(2^{-K})$, the algorithm is stopped.

4.3.5.2 QR decomposition using Givens Rotations

Givens rotations are used in this work to perform QR decomposition [41]. We consider the 2X2 real matrix

$$\mathbf{H} = \begin{bmatrix} h_{11} & h_{12} \\ h_{21} & h_{22} \end{bmatrix} = \begin{bmatrix} | & | \\ \mathbf{H}_1 & \mathbf{H}_2 \\ | & | \end{bmatrix} \tag{72}$$

The idea is to find such a unitary rotation matrix \mathbf{Q} so that when it multiplies column vector \mathbf{H}_1 it rotates it in the following way.

$$\mathbf{R}_1 = \mathbf{Q} * \mathbf{H}_1 = \begin{bmatrix} |\mathbf{H}_1| \\ 0 \end{bmatrix} \tag{73}$$

Multiplying \mathbf{H} by \mathbf{Q}

$$\mathbf{R} = \mathbf{Q}^* \mathbf{H} = \begin{bmatrix} |\mathbf{H}_1| & h_{12}' \\ 0 & h_{22}' \end{bmatrix} \quad (74)$$

In (74) \mathbf{R} is an upper triangular matrix with \mathbf{Q} as its unitary basis. The CORDIC-based QR decomposition of a 2X2 complex matrix is shown below as an example.

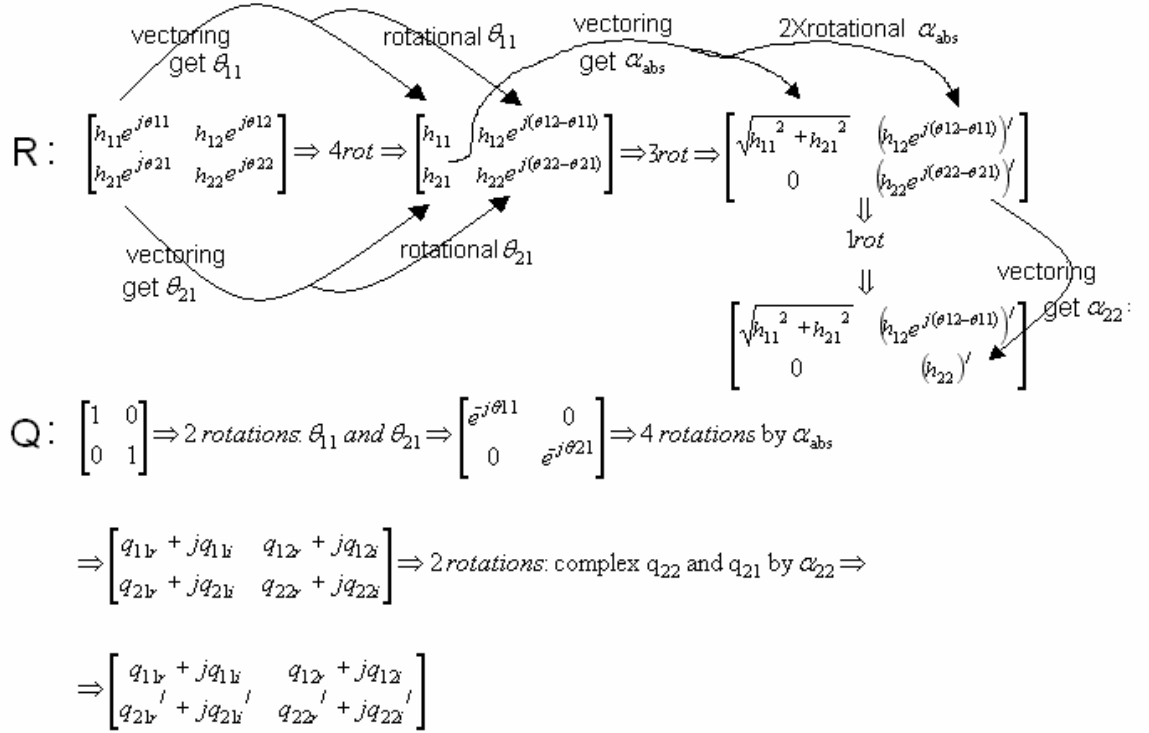


Figure 32. Using CORDIC to obtain upper triangular matrix \mathbf{R} and unitary \mathbf{Q} of a 2X2 complex matrix.

At the end of the procedure shown in figure 32, \mathbf{R} and \mathbf{Q} are obtained. Since \mathbf{R} is a complex matrix there are a total of 8 rotations needed to obtain the upper triangular matrix, with half of them in the vectoring mode. There are four rotations to generate real coefficients in the first column, three to perform Givens rotations and a final rotation to make the diagonal real. There are 8 additional rotations required to obtain \mathbf{Q} with all of these rotations performed by the CORDIC in a rotational mode.

For the CORDIC-based QR decomposition, the vectoring mode of CORDIC is used to introduce zeros in appropriate places while creating \mathbf{R} , as shown in figure 32. The Rotational mode of the CORDIC is used to update the rest of the vectors. If the sequence of the signs used during the vectoring mode is saved, it then can be used in (71) for the CORDIC in rotational mode to update the vector (updating $r_{12}e^{j(\theta_{12})}$ to $r_{12}e^{j(\theta_{12}-\theta_{11})}$, for instance). The middle two steps of (71) are not needed, hence reducing algorithm complexity.

4.3.5.3 Complexity of QR decomposition based on CORDIC

Two additions and two shifts are required to implement a micro-rotation by the orthonormal matrix in the first line of (70) and (71). The total scaling factor resulting from the multiplication of individual scaling factors is stored separately. Vector v is multiplied by K orthogonal matrices and then by the stored scaling coefficient.

For the CORDIC that uses K micro-rotations, it takes $8*2*K$ shifts + $8*2*K$ additions to form \mathbf{R} and the same number of shifts and additions to form \mathbf{Q} . The CORDIC in our work needed $K=11$ micro-rotations to reach the -41dB tracking error bound of figure 28. Two multiplications are required for the scaling coefficient at the end of each of the 16 rotations. Hence there are 352 shifts and 352 additions and 32 multiplications needed to perform the QR decomposition of a complex 2X2 matrix.

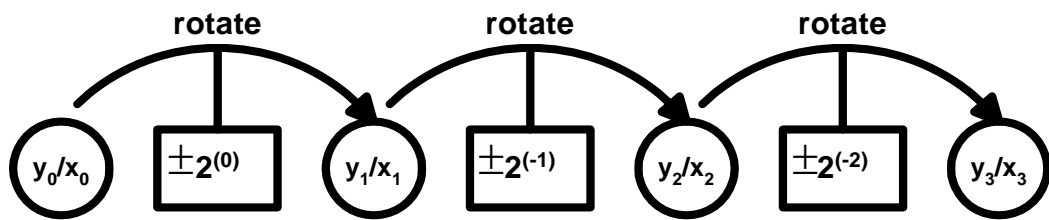
4.3.5.4 Modified CORDIC

When tracking the upper triangular matrix, the interference elements below the main diagonal and imaginary elements on the main diagonal start from zero.

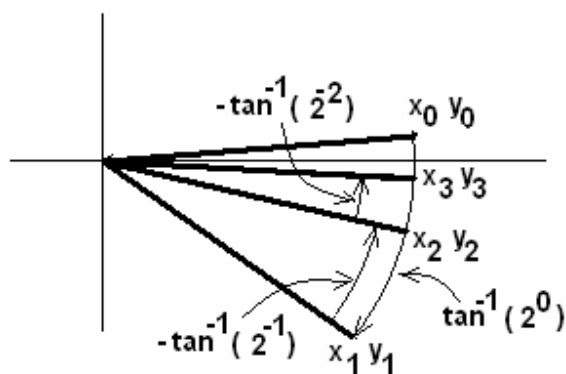
$$\hat{A}_R = \begin{bmatrix} r_{11r} + j0 & r_{12r} + jr_{12i} \\ 0 + j0 & r_{22r} + j0 \end{bmatrix} \quad (75)$$

The first complex element r_{11} will have a very small phase angle at the beginning. The second complex element r_{21} will have both elements very small at the beginning, with a uniformly distributed phase angle between 0° to 360° . The initial angle between the vector $\begin{bmatrix} r_{11} \\ r_{21} \end{bmatrix}$ and the x-axes is also likely to be very small. Since the QR decomposition is performed on this nearly upper triangular matrix, as explained in section 4.3.2.2 of this work, it makes sense to modify the CORDIC so that it uses a smaller number of micro-rotations for the smaller angles.

For an input vector defined as $\begin{bmatrix} x \\ y \end{bmatrix}$, $\tan(\alpha) = \frac{y}{x}$, operation of the conventional CORDIC algorithm can be presented as in figure 33.



(a)



(b)

Figure 33. (a) Conventional CORDIC with three micro-rotations. The micro-rotation angle is approximately halved for each consecutive iteration (b) CORDIC becomes inefficient when the input angle is small

The conventional CORDIC will go through a set number of micro-rotations (figure 33a) irrespective of the input angle. The direction of the next micro-rotation is always towards the positive x-axis. The CORDIC becomes inefficient when the input angle is small (figure 33b), since the first micro-rotation causes a large overshoot in the phase, which requires a number of iterations to correct. Processing power is wasted. The number of micro-rotations can be reduced by considering all possible micro-rotations and choosing the one that gives the smallest residual angle. Figure 34 conceptually describes the idea. The Number of micro-rotations has been reduced from three to only one.

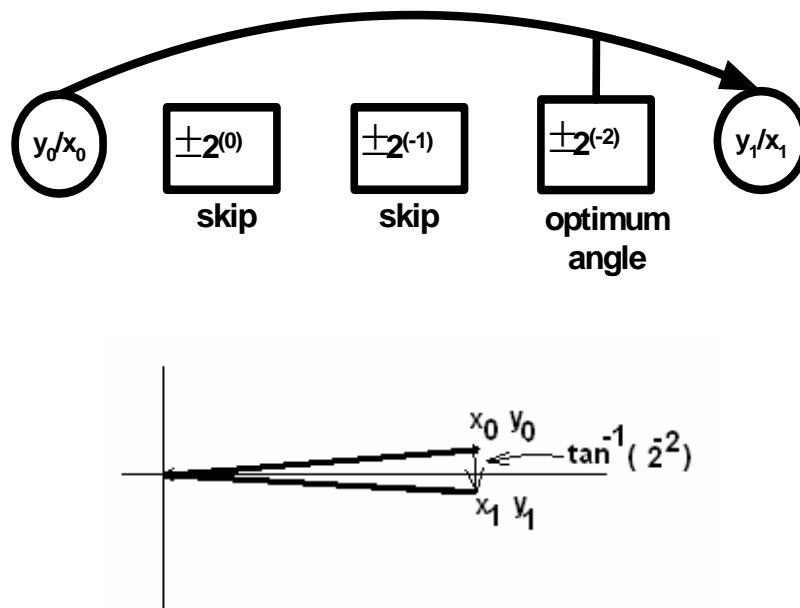


Figure 34. Reducing the number of micro-rotations to one, by considering all possible micro-rotations at each iteration

One way to find the optimum angle is to use a method of approximate rotations suggested first by Gotze et al in 1996 [69, 70]. This method is used here to reduce the number of iterations for the small angles of the $\hat{\mathbf{A}}_{\mathbf{R}}$ matrix. The technique is explained below.

Representing $\tan(\alpha)$ in the floating point binary format

$$\tan(\alpha) = \frac{M_y * 2^{e_y}}{M_x * 2^{e_x}} = \frac{M_y}{M_x} * 2^{(e_y - e_x)} \quad (76)$$

Where M_y and M_x are mantissas and e_y and e_x are the exponents of y and x respectively.

Since $1 \leq M_y \leq 2$, $1 \leq M_x \leq 2$ then

$$2^{-1} \leq \frac{M_y}{M_x} \leq 2^1 \quad (77)$$

With $2^a = 2^{(e_y - e_x)}$, used as an approximate rotation and taking (77) into account, the set of possible choices is narrowed down to

$$\left[2^{(a-1)}, 2^{(a)}, 2^{(a+1)} \right] \quad (78)$$

Dickson [71] used two additional rotations to find the closest value among the three options in (78). To avoid this additional complexity we suggest using the middle of the three options $2^{(a)}$, regardless of which of the three choices is closer to $\frac{y}{x}$. Statistically, the probability that this is the correct choice is 50%. For the other 50% of occurrences the system still converges, but in the worst case will activate all the following available micro-rotations.

In this work the value of y_i rather than the ‘set angular tolerance’ is used to terminate the rotating process of the vectoring CORDIC. This will tend to equalise the residual errors in the $\mathbf{A}_{\mathbf{R}}$ matrix coefficients after the QRD has been completed. It will also eliminate unnecessary rotations.

The modified vectoring mode algorithm will now be described in pseudo-code.

1. *Move the input vector, $\begin{bmatrix} x_i \\ y_i \end{bmatrix}$, into the first octant by inverting signs and flipping the x and y magnitudes as appropriate*
2. *Obtain the exponent difference $(e_y - e_x) = a$*

Refer to Appendix 1 for details

3. *Rotate with 2^a to perform the approximate micro-rotation*

$$\begin{bmatrix} x_{i+1} \\ y_{i+1} \end{bmatrix} = \begin{bmatrix} 1 & d * 2^a \\ -d * 2^a & 1 \end{bmatrix} * \begin{bmatrix} x_i \\ y_i \end{bmatrix}$$

4. *Check the stop condition. If $(y_i < \text{accuracy floor})$ Apply scaling factor from LUT, re-adjust signs and stop. Else next iteration (go to 2)*

The sign and flipping information, the sequence of a's and the scaling factor are used in the rotational part of the modified CORDIC to update the other vectors.

Figure 35 depicts the number of micro-rotations needed to obtain an angular accuracy of $\alpha < \tan^{-1}(2^{-9})$ for the modified CORDIC. The average number of micro-rotations is 4.3 which is significantly below the fixed set of 10 micro-rotations, required by a conventional CORDIC with the same accuracy. The average is further reduced when angles are small. Note angles in the range of $\tan(\alpha) \leq 0.02$ are common in the upper triangular matrix tracking scheme of sub-section 4.3.2.

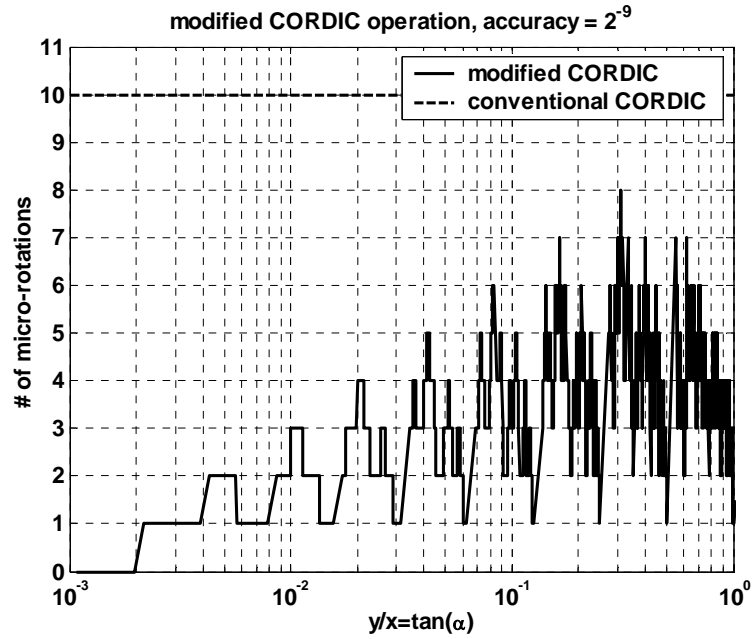


Figure 35. The number of microrotations vs $\frac{y}{x}$ ($= \tan(\alpha)$). Zero corresponds to $\alpha=0$ degrees and 1 corresponds to $\alpha=45$ degrees.

There is an additional computational overhead in the proposed algorithm. It is associated with obtaining the exponential difference (step 2) when the algorithm is implemented on fixed-point hardware. Also, a LUT containing all possible combinations of the scaling factors is needed, since the rotational sequence is no longer fixed. The number of scaling factors (equal to $2^{nb/2}$) determines the LUT size. When QR decomposition is performed some vectors are rotated by the sequence obtained earlier from the vectoring mode, as shown in figure 32. The described computational overheads do not exist for the CORDIC in the rotational mode.

4.3.5.5 Complexity of QRD based on the modified CORDIC

N micro-rotations require the complexity of $2*N$ additions + $2*N$ shifts in the vectoring mode algorithm. The function that finds the exponent difference adds an overhead complexity of P comparisons and additions, and S shifts. The values of P and S depend on the way the function is

realised. Appendix 1 demonstrates the realisation of the function used in this work. Defining the complexity of the vectoring CORDIC as C_V :

$$C_V = (2*N+P) \text{ additions} + (2*N+S) \text{ shifts} \quad (79)$$

Here, comparisons are assumed to have an equivalent complexity to additions. The rotational CORDIC has only the complexity of N micro-rotations. Defining its complexity as C_R , then

$$C_R = 2*N \text{ additions} + 2*N \text{ shifts} \quad (80)$$

This is much less than the vectoring CORDIC because it does not include the overhead of estimating the approximate angle.

The total complexity of the QR decomposition of a 2×2 complex matrix is

$$C_{2 \times 2} = (4*C_V + 4*C_R) + 10*C_R \quad (81)$$



R matrix

Q matrix

For the case of an n by n full-rank matrix this can be generalised to

$$C_{n \times n} = n^2 * C_V + \left(\frac{1}{2} * n^3 + \frac{11}{2} * n^2 - 5 * n - 2^{3-n} * (n^2 - n) \right) * C_R \quad (82)$$

The rotational complexity (second term) grows much more quickly than the vectoring complexity (first term).

4.3.6 Simulation results

Table 2 shows a comparison in the complexity of the conventional and modified CORDIC algorithms. It was found that the conventional CORDIC required 11 micro-rotations to guarantee convergence to the LMS tracking floor in figure 29. Similarly, the modified CORDIC was required to meet $y_i < 2^{-9}$ before termination. The modified algorithm is data dependent and so the average number of operations was obtained from uniformly distributed values of x and y between 0 and 1.

Complexity CORDIC	Shifts	Additions
Standard vectoring or rotational mode	22	22
Modified, Vectoring mode (C_V)	27.29	22.18
Modified, Rotational mode (C_R)	6.43	6.43

Table 2 Complexity comparison between standard CORDIC of 11 micro-rotations and Modified CORDIC with termination condition $|y_i| < 2^{-9}$

It can be observed from table 2 that the overhead increases the complexity of the modified CORDIC in the vectoring mode, but reduces the complexity in the rotational mode. However, there is a net complexity reduction when the modified CORDIC is used to perform QR decomposition. Substituting table 2 values into (82) for the 2x2 case gives 0.53 times the number of shifts and 0.47 times the number of additions compared to the conventional CORDIC. The performance savings improve as the matrix size increases.

For the \mathbf{A}_R tracking scenario there will be even larger savings as the angles on average are smaller, resulting in fewer micro-rotations. Figure 36 plots the complexity of the \mathbf{A}_R tracking scenario based on the *modified* CORDIC as the fraction of the complexity of the H tracking case based on the *conventional* CORDIC.

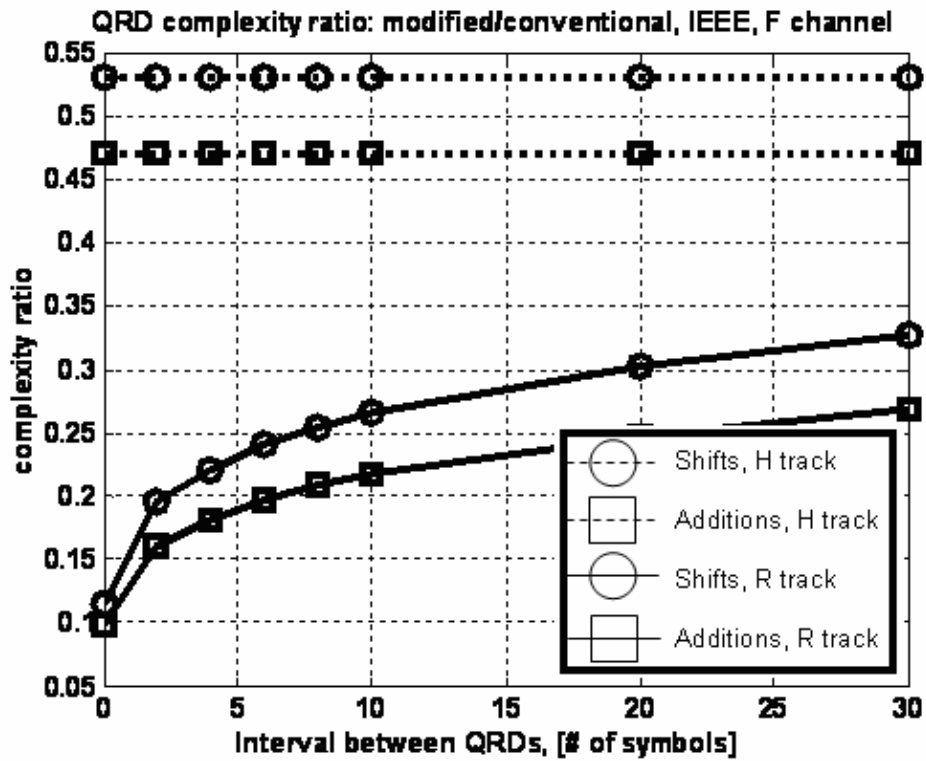


Figure 36. Complexity savings of the A_R tracking with modified CORDIC over the H tracking with the conventional CORDIC in 2X2 system

For a small number of symbols between consecutive QR decompositions, there are large savings in the number of shifts and additions per symbol. The savings are less as the QR decomposition frequency decreases, asymptotically reaching their respective upper bounds. However, savings are still worthwhile at the repetition rates suggested by figure 29 (20 to 30 symbols).

At diminished signal-to-noise ratios the LMS tracking floor (figure 28) rises, reducing the accuracy requirements on the QR decomposition and allowing a larger terminating value for y_i and so a lower number of micro-rotations. Table 3 shows the required y_i termination levels for the modified CORDIC, as well as the number of micro-rotations for the conventional CORDIC for various SNRs.

SNR [dB]	10	12	14	16	18	20	22	24	26	28	30
Term. y_i	2^{-5}	2^{-5}	2^{-6}	2^{-6}	2^{-6}	2^{-7}	2^{-7}	2^{-7}	2^{-8}	2^{-8}	2^{-9}
Rotation number	7	7	8	8	8	9	9	9	10	10	11

Table 3 Termination y_i value for various operating SNR

Finally, table 4 demonstrates the complexity savings for various SNR with MSE thresholds set proportionally lower for higher SNR values.

SNR [dB]	Target [dB]	A_R/H shifts	A_R/H add
20	-26	0.23	0.196
22	-28	0.21	0.188
24	-30	0.19	0.162
26	-32	0.22	0.183
28	-34	0.2	0.165
30	-36	0.22	0.184

Table 4 Complexity comparisons for various SNR

Table 4 shows that the proposed modifications to the CORDIC reduce the complexity of the A_R tracking scheme even further compared to the results reported in Table 1. The complexity of the A_R tracking scenario is now reduced to 20% of the shifts and about 18% of the additions compared to the original channel-tracking scenario.

All the results described until now have been obtained under the assumption of the error free detection. The following section will consider the more practical case of VBLAST-MMSE detection and compares both developed LMS strategies to the RLS-DFE scheme of [1].

4.4 Evaluation of the two proposed strategies with VBLAST-MMSE detection and comparison with RLS based DFE scheme.

4.4.1 Introduction

MSE of the channel estimate was used as a performance metric in the previous section. In this section, however, we wish to use more realistic BER metric for performance evaluation of both tracking schemes. VBLAST-MMSE achieves the closest performance to optimum MLS detection, while ZF has the worst performance, according to figure 17. For this reason we have chosen to implement both tracking scenarios with the VBLAST-MMSE detection algorithm. We evaluate the accuracy of the channel estimation as well as BER performance.

The major modification to the system model described in figures 21,23 and 25 is the use of the extended channel matrix, required for MMSE detection [28, 40]. It is defined as $\hat{\mathbf{H}} = \begin{bmatrix} \hat{\mathbf{H}} \\ \sigma_n \mathbf{I}_{M \times M} \end{bmatrix}$

$\hat{\mathbf{H}}$ can be written as a product of two matrices:

$$\hat{\mathbf{H}} = \begin{bmatrix} \hat{\mathbf{Q}}_1 & \hat{\mathbf{Q}}_2 \end{bmatrix} * \begin{bmatrix} \hat{\mathbf{R}} \\ \mathbf{0}_{N \times M} \end{bmatrix} \quad (83)$$

where $\hat{\mathbf{Q}}_1 \in C^{(N+M) \times M}$, $\hat{\mathbf{Q}}_2 \in C^{(N+M) \times N}$ and $\hat{\mathbf{R}} \in C^{M \times M}$. $\hat{\mathbf{Q}}_1$ spans orthogonal subspace of $\hat{\mathbf{H}}$; and $\hat{\mathbf{Q}}_2$ is an orthogonal basis for the null-space of the Hermitian of $\hat{\mathbf{H}}$.

The $\hat{\mathbf{Q}} = \begin{bmatrix} \hat{\mathbf{Q}}_1 & \hat{\mathbf{Q}}_2 \end{bmatrix}$ and $\hat{\mathbf{R}}$ matrices are obtained through QR decomposition and then used to equalise the channel for the received data symbols y . QR equalisation is based on the following identity

$$\hat{\mathbf{Q}}^H * \mathbf{y} = \hat{\mathbf{R}} * \mathbf{s} \quad (84)$$

Since $\hat{\mathbf{R}}$ is an upper triangular matrix, symbol recovery is possible via SIC. The data is remapped for the feedback path and then used as an input, $\hat{\mathbf{s}}$, to the LMS channel-tracking algorithm.

\mathbf{R} denotes the strictly upper triangular matrix while \mathbf{A}_R (used from section 4.4.2.2 onwards) represents an upper triangular matrix $\mathbf{A}_R = \begin{bmatrix} \mathbf{R} \\ \mathbf{0}_{N \times M} \end{bmatrix}$ that loses its upper triangular structure in the course of tracking. In this section Jakes model describes the Doppler effect of the non-stationary channel.

4.4.2 Evaluation of tracking schemes

The two LMS tracking strategies presented in this sub-section aim to reduce the computational complexity per symbol in QR detection based receivers. They both achieve this goal by reducing the recurrence rate of QR decompositions, exploiting the better correlation properties of the channel compared to the inverse channel. Here, we evaluate the complexities of these tracking schemes with MMSE detection and compare them with the algorithm in [1]

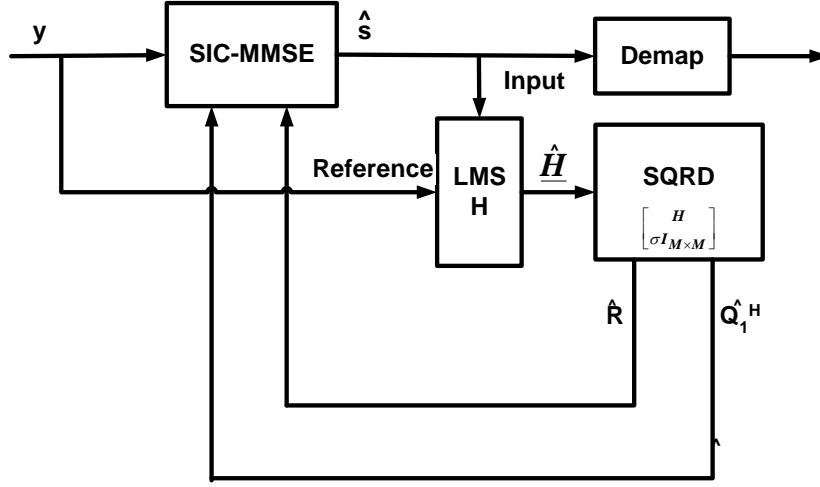
4.4.2.1 Tracking the channel matrix H 

Figure 37. Decision-directed tracking and Sorted QR decomposition (SQRD) for the channel-tracking case.

The re-mapped symbol, \hat{s} from the MMSE detector (Fig. 37) forms the input to the LMS and the received signal y is used as reference. The LMS then adjusts the coefficients of \hat{H} to minimise the error signal $|y - \hat{H} * \hat{s}|$.

The low-complexity Sorted QR Decomposition (SQRD) developed in [39] is used to obtain suboptimal ordering and QR decomposition. The matrix $\hat{H}_{(i)}$ represents the extended channel estimate matrix at the i^{th} time instant. SQRD decomposes it as

$$\hat{H}_{(i)} = \hat{Q}_{1(i)} * \hat{R}_{(i)} \quad (85)$$

from which the term $\hat{Q}_1^H * y$ can be obtained. \hat{Q}_2 is not required in this tracking scenario, since it multiplies the last N rows of zeros in $\begin{bmatrix} \hat{R} \\ \mathbf{0}_{N \times M} \end{bmatrix}$. If the SQRD is not performed every symbol time

instant, the complexity per symbol in the system is reduced but the matrices \hat{Q}_1 and \hat{R} become

obsolete. Obsolete $\hat{\mathbf{Q}}_1$ and $\hat{\mathbf{R}}$ values will cause an error in the equalisation that increases as the estimates get older. The error matrix, $\mathbf{er}_{\mathbf{H}(i)}$ represents the instantaneous deviation of the channel estimate by the LMS tracking algorithm from the actual channel matrix

$$\mathbf{er}_{\mathbf{H}(i)} = \mathbf{H}_{(i)} - \hat{\mathbf{Q}}_{1(n)} * \hat{\mathbf{R}}_{(n)} \quad (86)$$

Here $\mathbf{H}_{(i)}$ is the actual channel matrix at the time instant, i , while $\hat{\mathbf{Q}}_{1(n)}$ and $\hat{\mathbf{R}}_{(n)}$ are unitary and upper triangular matrices obtained at the n^{th} instant ($(i - n)$ time instances earlier), from the LMS estimate $\hat{\mathbf{H}}_{(n)}$. Whenever a SQRD is performed, n is set to be equal to i . With γ defined as the maximum interval between consecutive SQRDs, we can calculate the total complexity of the algorithm as

$$C_H = \frac{1}{\gamma} * \left(8M^3 + \frac{13}{2}M^2 - \frac{1}{2}M \right) + \frac{\gamma-1}{\gamma} * \left(\frac{13}{2}M^2 - \frac{1}{2}M \right) \quad (87)$$

4.4.2.2 Tracking the upper triangular matrix

The growth in equalisation error can be reduced by tracking the upper triangular matrix. This is because some of the tracked elements can be used immediately in the equalisation process.

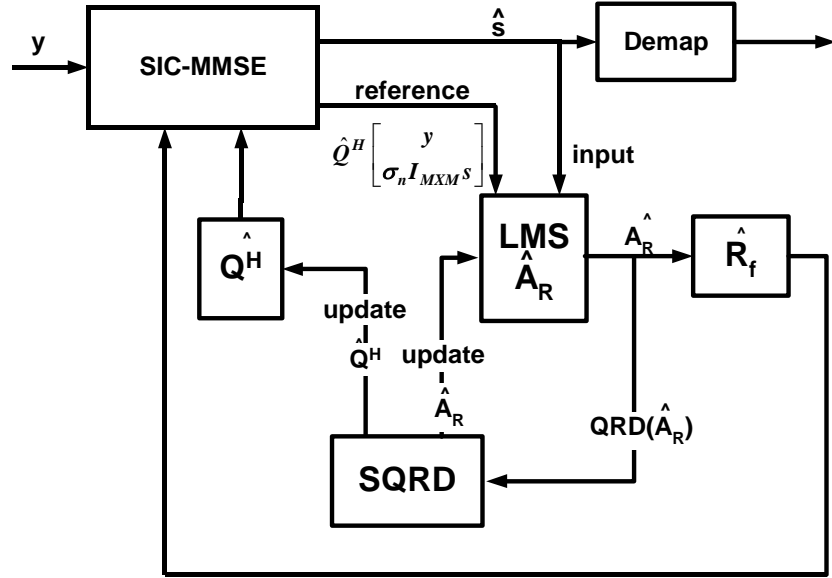


Figure 38. Decision-directed tracking and SQRD for the upper triangular matrix-tracking scenario

In this scenario (figure 38), the LMS algorithm tracks the \mathbf{A}_R matrix (the \mathbf{R} matrix that loses its non-upper triangular form), while the \mathbf{Q} matrix is held fixed until it is updated by the next QR decomposition. At any time instant the channel matrix \mathbf{H} can be presented as

$$\underline{\mathbf{H}}(i) = \mathbf{Q}(n) * \mathbf{A}_{R(i)} \quad (88)$$

Here $\underline{\mathbf{H}}(i)$ is the actual extended channel matrix at the i^{th} time instant, $\mathbf{Q}(n)$ is a unitary matrix obtained $(i - n)$ time instances ago (from $\hat{\mathbf{H}}(n)$), and $\mathbf{A}_{R(i)}$ is generally a non-upper triangular matrix. $\mathbf{A}_{R(i)}$ has the upper triangular form when $n = i$, immediately after a QR decomposition. As $(i - n)$ increases, $\mathbf{Q}(n)$ becomes more obsolete, hence $\mathbf{A}_{R(i)}$ has to change to compensate for the

changing channel. As a result, $\mathbf{A}_{\mathbf{R}(i)}$ has non-zero components introduced below the main diagonal as well as non-real components on the main diagonal.

The non-upper triangular $\hat{\mathbf{A}}_{\mathbf{R}(i)}$ matrix (an estimate of $\mathbf{A}_{\mathbf{R}(i)}$ produced by the LMS tracking algorithm) is not suitable for the back substitution process used in the SIC block of figure 38. A modified copy of $\hat{\mathbf{A}}_{\mathbf{R}(i)}$ is needed. In this modification all the non-zero imaginary elements on the main diagonal and all the elements below the main diagonal are set to zero. The created upper triangular matrix $\hat{\mathbf{R}}_{\mathbf{f}}$ can then be used for equalisation. The forcing-to-zero operation, however, creates an additional error.

For the case of a 4X2 matrix, the additional error is given by

$$\left(\hat{\mathbf{A}}_{\mathbf{R}} - \hat{\mathbf{R}}_{\mathbf{f}} \right) = \begin{bmatrix} jr_{11i} & 0 \\ r_{21r} + jr_{21i} & jr_{22i} \\ r_{31r} + jr_{31i} & r_{32r} + jr_{32i} \\ r_{41r} + jr_{41i} & r_{42r} + jr_{42i} \end{bmatrix} \quad (89)$$

Every time QR decomposition is performed on $\hat{\mathbf{A}}_{\mathbf{R}}$ it resets the error matrix in (89) to zero.

The overall error includes tracking inaccuracies as well as error caused by creating $\hat{\mathbf{R}}_{\mathbf{f}}$. It is defined as

$$er_{R(i)} = \mathbf{Q}_{(n)} * \mathbf{A}_{\mathbf{R}(i)} - \hat{\mathbf{Q}}_{(n)} * \hat{\mathbf{R}}_{\mathbf{f}(i)} \quad (90)$$

The first product in (90) forms the ideal channel matrix \mathbf{H} , while the second product term defines the channel matrix used in the SIC-MMSE equaliser.

The average power per element of the error matrices $\mathbf{er}_{\mathbf{H}(i)}$ and $\mathbf{er}_{\mathbf{R}(i)}$ is used as a MSE metric for simulation comparisons in this work.

SQRD can be performed on $\hat{\mathbf{A}}_{\mathbf{R}(i)}$ at any time to bring it back to upper triangular form, and update the order and the unitary matrix \mathbf{Q} , as shown below

$$\hat{\mathbf{H}}_{(i)} = \hat{\mathbf{Q}}_{(n)} * \text{SQRD}(\hat{\mathbf{A}}_{\mathbf{R}(i)}) = \hat{\mathbf{Q}}_{(n)} * \hat{\mathbf{Q}}_{(i)}' * \hat{\mathbf{R}}_{(i)}' \quad (91)$$

In (91) $\hat{\mathbf{Q}}_{(n)} * \hat{\mathbf{Q}}_{(i)}'$ forms a new unitary matrix and $\hat{\mathbf{R}}_{(i)}'$ is the new upper triangular matrix that updates the $\hat{\mathbf{A}}_{\mathbf{R}}$ value in the LMS tracking block of figure 35. This algorithm has two additional complexity factors compared to the H tracking algorithm (section 4.4.2.1).

- The LMS will now track $(N+M)M$ elements compared to NM elements in the H tracking algorithm
- The SQRD, which is based on the modified Gramm Schmidt algorithm, can only provide $\hat{\mathbf{Q}}_1$. The null space of $\hat{\mathbf{H}}$ is calculated and orthogonalised to obtain $\hat{\mathbf{Q}}_2$.

The total complexity of this algorithm is

$$C_R = \frac{1}{\gamma} * \left(17M^3 + \frac{7}{2}M^2 - \frac{3}{2}M \right) + \frac{\gamma-1}{\gamma} * \left(\frac{17}{2}M^2 - \frac{1}{2}M \right) \quad (92)$$

The complexity per symbol of the algorithm in [1], along with the complexities of the two proposed strategies, is shown in figure 39.

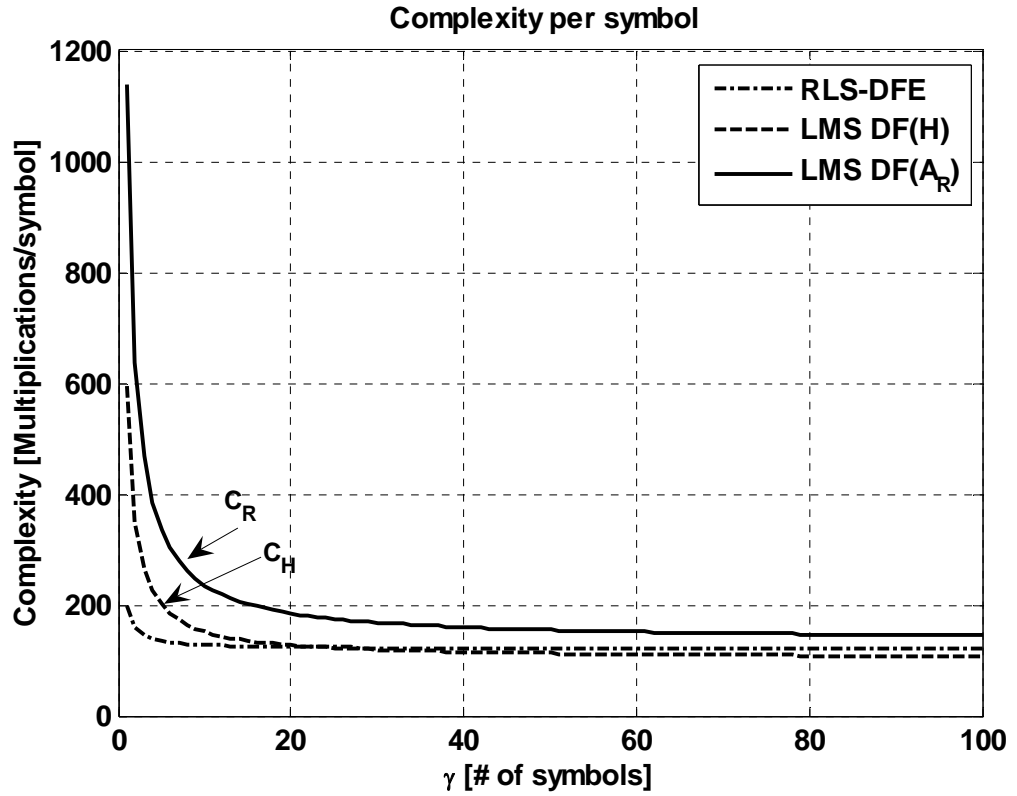


Figure 39. Complexity per symbol vs QR (order) update time

Along the horizontal axis, γ defines a number of symbols between successive order updates for the algorithm in [1] or number of symbols between successive SQRDs for channel tracking and upper triangular matrix tracking (or A_R tracking) scenarios. The RLS scheme of [1] is surprisingly competitive. The LMS channel-tracking schemes have the additional complexity overhead of performing a SQRD, which results in large complexities with small γ ('LMS DF(H)' line). The cost is even higher for the A_R tracking algorithm ('LMS DF(A_R)' line), where calculation of \hat{Q}_2 is required.

As γ increases, however, the complexity per symbol drops, and reaches asymptotically the complexity of the LMS algorithm, which is inherently lower than the complexity of the RLS algorithm. This is why the complexity per symbol for the channel-tracking scenario drops below the complexity of the RLS-based algorithm (for $\gamma > 24$). The LMS of the A_R tracking algorithm ('LMS

DF(\mathbf{A}_R)' line), however, has to track more coefficients than the other two algorithms, resulting in higher complexity (17% more expensive as γ approaches 100).

However, tracking the \mathbf{A}_R upper triangular matrix results in a more accurate channel estimate, as shown in the next section.

4.4.2.3 *Simulation results*

Complexity analysis in the previous section has shown that while the channel tracking scheme can compete with the one proposed by Choi et al in [1], the upper triangular matrix scheme fails to do so, because of the additional complexity overhead in tracking the nullspace of the extended channel matrix. This section presents performance comparisons of these three tracking schemes in stationary as well as non-stationary environment. Figure 40 depicts the BER performance comparisons of the proposed LMS tracking schemes with [1]. Only the performance of the \mathbf{A}_R tracking algorithm is shown on the figure; however, since the channel is stationary, there is no difference between the BER performances of the two LMS tracking algorithms. VBLAST-ZF and VBLAST-MMSE are shown as reference curves.

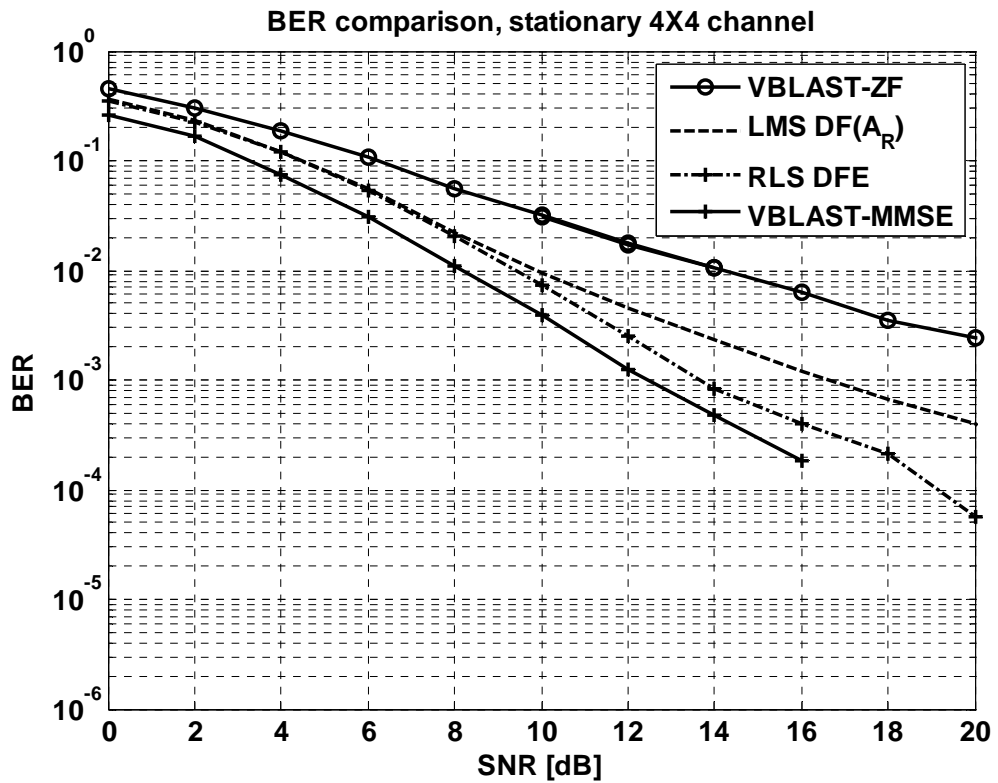


Figure 40. BER comparison for the stationary channel

Tracking error of the RLS algorithm in [1] ('RLS DFE' curve) causes about 1dB of consistent difference in performance compared to VBLAST-MMSE with known channel ('VBLAST-MMSE' curve). The proposed algorithm ('LMS DF(A_R)') has a performance identical to that of the RLS-based system up to SNR of 8dB. Deterioration of performance for the higher SNRs is caused by suboptimum ordering of the SQRD [40].

Figure 41 depicts MSE in the channel estimate of both tracking schemes. The initial training of 40 symbols reduces the MSE in the channel estimate to -28dB.

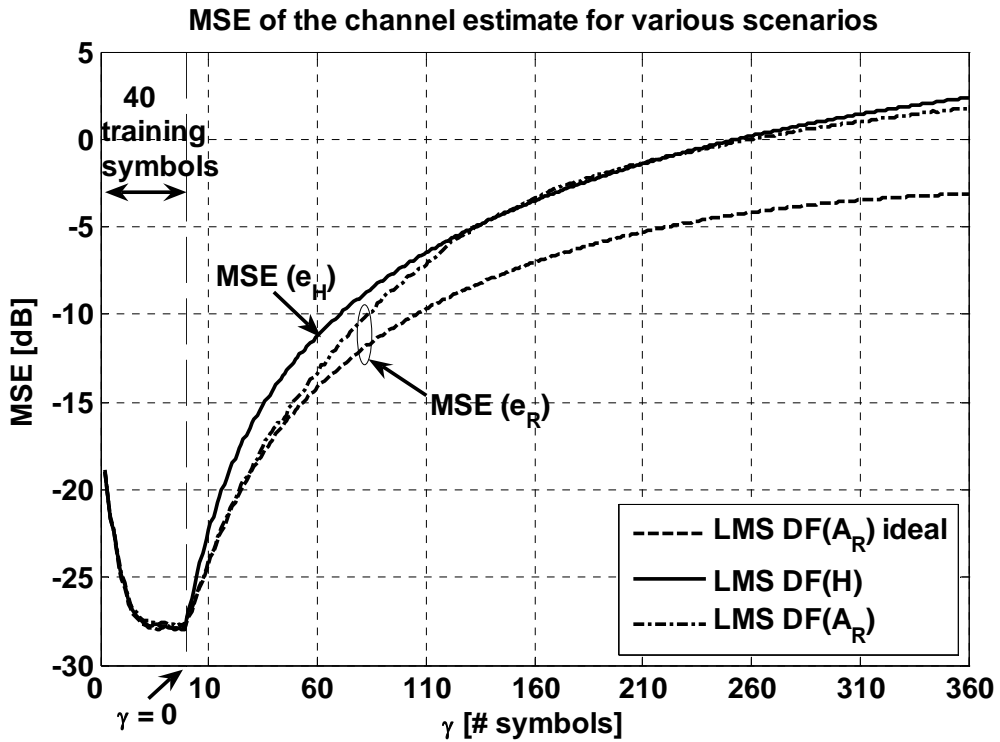


Figure 41. Channel MSE for A_R and H tracking strategies, SNR=20dB, $fdT=1*10^{-3}$

The ‘LMS DF(H)’ line shows the growth in mean squared of er_H as γ increases. The ‘LMS DF(A_R) ideal’ line depicts the growth in mean squared of er_R when A_R tracking is performed *without* symbol errors on the feedback path to the LMS routine. This scenario has slower MSE growth because some of the elements of \hat{R}_f are being tracked. When the data stream on the feedback path to the LMS *includes* symbol errors caused by the SIC-MMSE detection block (‘LMS DF(A_R)’ line), the advantage of slower MSE growth is retained until γ reaches about 120 symbols.

The BER performance of the SIC MMSE vs. γ with both tracking schemes is shown in Fig. 42. Gamma values up to 40 are shown, and in this region A_R tracking outperforms the H tracking scheme in an MSE sense, but the top two curves do not show this. Clearly the SIC detection errors eliminate the advantage of the LMS DF(A_R) scheme. When the same setup was repeated without the detection errors on the first layer, but with errors still on the feedback path to the channel

tracking, the resulting two dashed curves ('LMS DF(H) no detect error' and 'LMS DF(A_R) no detect error' lines) have shown a near order of magnitude improvement. The clear superiority of A_R tracking over H tracking scenario is also observed. Error propagation from the first detected layer to the higher layers is therefore the dominant source of performance loss.

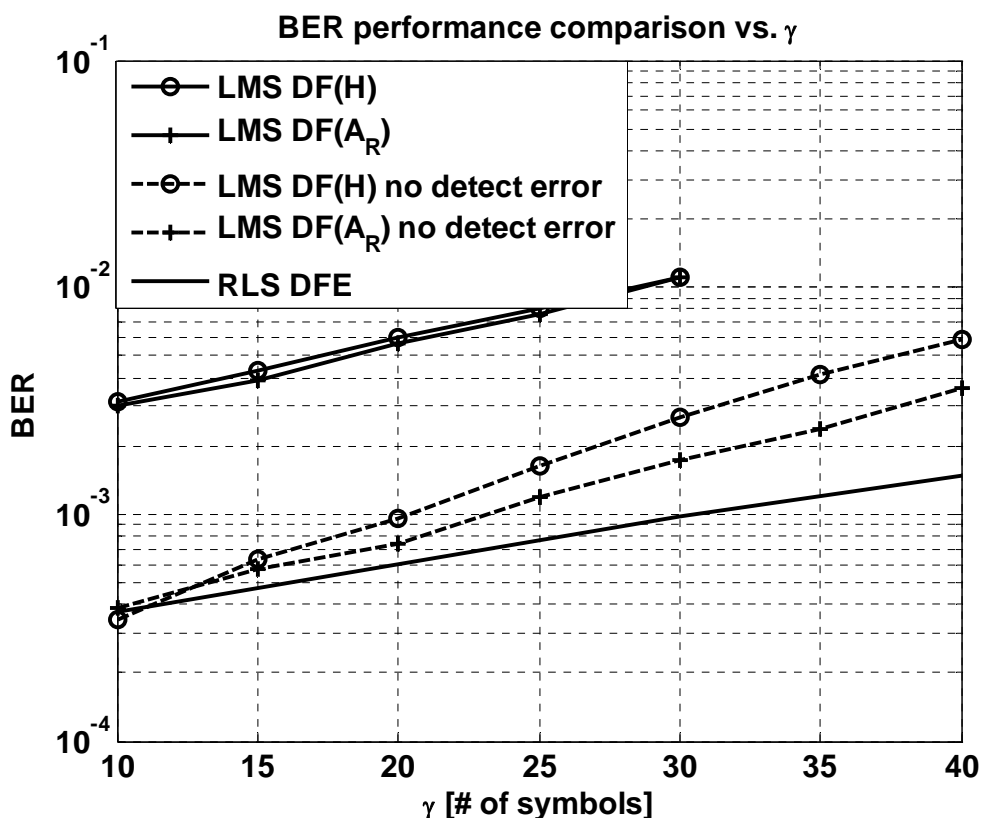


Figure 42. A_R and H tracking BER results, as well as the BER result from [1], SNR=20dB, $fdT=1 \cdot 10^{-3}$

The bottom line "RLS-DFE" represents the BER of the scheme proposed in [1]. It clearly has the superior performance to both of the proposed tracking schemes 'LMS DF(A_R)' and 'LMS DF(H)', even though it is tracking a more dynamic environment.

4.5 Conclusions

When channel tracking is employed, QR decomposition can be performed on every symbol. Reducing the frequency of QR decompositions and using fixed Q and R matrices between successive QR decompositions will reduce computational complexity per symbol at the expense of the increased estimation error. It was shown in this work that tracking the upper triangular matrix instead of the channel matrix would reduce computational complexity per symbol by about 1.5 times without introducing any additional estimation error into the system. However the implementation of QR decomposition may require special hardware, in which case there are no cost savings in reducing the QR decomposition frequency. The main benefit is in the reduction of power consumption for this computationally intensive process.

Tracking the upper triangular matrix \mathbf{A}_R will introduce cross-talk components below its main diagonal. QRD, based on the CORDIC algorithm, is then applied to \mathbf{A}_R . It rotates column vectors so that cross-talk components are eliminated. Initially, the rotation angles will be small, hence the CORDIC algorithm was modified to take advantage of these smaller angles to reduce the number of iterations. It was shown that this modification, when used with upper triangular matrix tracking, resulted in a further complexity reduction compared to the channel-tracking scenario. A total saving by a factor of between 2 and 10 in a Wireless LAN environment was obtained.

VBLAST-MMSE was used with the two tracking strategies to obtain BER performance comparisons. A low-complexity SQRD algorithm was employed for detection ordering, as well as to perform the QRD. The \mathbf{A}_R tracking strategy initially yielded better channel estimates at an SNR of 20dB. With time, however, this advantage was eliminated by the errors in the data stream fed back into the tracking algorithm. Further, it was found that better channel estimates did not translate into superior BER results due to the propagation error of the first layer in the detection algorithm.

Both strategies were compared in complexity and performance to the RLS-based algorithm in [1]. The complexity of the LMS-based channel-tracking scheme dropped below the RLS-based system after the distance between adjacent SQRDs exceeded 24 symbols ($\gamma > 24$). In the \mathbf{A}_R tracking scenario, however, a nullspace of the channel matrix had to be calculated and tracked. This additional overhead kept the complexity of the upper triangular matrix scheme 17% higher compared to the complexity of the RLS-based system after $\gamma = 100$ symbols. The BER performance of both strategies was found to be inferior to the RLS-based system in a stationary as well as a non-stationary environment. This is due to the suboptimum orderings obtained by the SQRD algorithm. Overall, the DFE approach, adopted by Choi et al in [1] outperformed the two LMS based channel tracking strategies, indicating that the RLS tracking scheme more than compensates for the faster moving characteristics of the inverse channel.

ACKNOWLEDGMENT

The WLAN channel models used in the Matlab[®] simulations were developed by the IST research project IST-2000-30148 I-METRA.

5 Conclusions

The thesis focused on the implementation issues of MIMO algorithms. Two problems were investigated:

- The effect of ADC-induced clipping on the performance of Alamouti STBC system
- The performance of low complexity channel tracking and equalisation schemes .

The first part, described in chapter 3, considers the practical implementation issue of the popular Alamouti STBC algorithm. Choosing an ADC with a smaller dynamic range and reduced voltage supply rails can save the power consumption of the circuitry. This, however, will result in an increased clipping distortion of the signal, which can adversely affect the overall performance of the system. It was found that clipping breaks the orthogonality of the STBC, making it more sensitive to clipping than uncoded single antenna systems. It is further established in Chapter 3 that STBC QPSK modulation requires an extra 7 dB back-off into the ADC, while 16QAM modulation only requires 1dB. Two receiver structures for implementing the STBC system were considered in this chapter: Direct Conversion (DC) receiver structures that impose square clipping on the signal, and Log-Polar receiver structures that induce circular clipping. The Log-Polar receiver structure is best suited for M-PSK modulated signals, since the magnitude distortion caused by the logarithmic amplifiers does not affect system performance. Log-Polar receivers were found to be clipping

insensitive at the given SER target of 10^{-3} . This makes Log-Polar receivers an obvious choice when M-PSK modulation is employed.

QR detection is frequently used as a faster alternative to a channel inversion in a MIMO scheme. A computationally intensive QR decomposition algorithm is used to obtain R and Q matrices employed by a QR equaliser. When channel tracking is used, the QR decomposition has to be performed at every instance a new channel estimate is obtained. This will result in a high computational complexity per symbol. We have proposed in chapter 4 to reduce the rate of QR decomposition while continuing to track the channel. This will reduce the complexity per symbol at the expense of the increasing error from using an outdated unitary Q and upper triangular R matrices. We have also shown that by tracking directly the upper triangular matrix, a further 33% reduction in complexity per symbol is possible.

QR decomposition is often based on a CORDIC algorithm that performs the rotations needed to obtain the Q and R matrices. CORDIC obtains the desired angle by using a fixed number of iterations. We have demonstrated that by tracking the upper triangular matrix and allowing a variable number of iterations for the CORDIC algorithm it is possible to reduce the complexity of QR decomposition by factor of between 2 and 10.

Both channel tracking and upper triangular matrix tracking strategies were implemented with the VBLAST-MMSE detection algorithm to obtain the MSE performances. Upper triangular matrix tracking has a consistent performance advantage over channel tracking. However in the more practical case, with detection errors allowed in the feed-back stream, this MSE advantage was wiped out after 120 Symbols.

Unfortunately, any MSE advantage due to upper triangular matrix tracking, does not translate into a BER improvement when layered detection is used. This is because the MSE of the first detection layer is not improved and so error propagation dominates the performance. We

hypothesise that soft detection followed by error correction decoding would reclaim the MSE advantage.

Both strategies were compared in complexity and performance to the RLS DFE-based scheme in [1] (which essentially tracks a highly dynamic inverse channel matrix) , to see whether the benefit of tracking a slower changing matrix with the simpler algorithm outweighs the additional need for occasional channel inversions. The upper triangular matrix-tracking scheme is required to track the nullspace of the extended channel matrix. This overhead significantly increases the complexity of the system. The overall complexity per symbol then was $\sim 17\%$ higher than that of the RLS-based system when the distance between adjacent QRDs was 100 symbols ($\gamma=100$ symbols). The complexity of the channel-tracking scheme, on the other hand, dropped below the complexity of RLS DFE for $\gamma > 24$ symbols. Both LMS strategies had an inferior BER performance compared to the DFE RLS-based system of [1], and surprisingly the LMS schemes showed no significant complexity improvement.

5.1 Future work

Chapter 3 investigated only a clipping effect. The next important step is to include a quantisation noise effect. Then as the voltage supply rails are increased for the given number of bits, the quantisation noise will increase, affecting the performance of the system. Hence there is an obvious trade off between the clipping noise and quantisation noise. Future work would use this trade off to find the point where the error due to these two effects is minimum, enabling ADC optimisation for a target SER.

The promising approach to low-complexity upper triangular matrix tracking in chapter 4 could not be realised with VBLAST-MMSE detection. Future work would employ ZF detection and bit-interleaved channel coding and modulation (BICM) with upper triangular matrix tracking as an alternative approach. ZF, performed via QR equalisation, does not impose any overheads on the

tracking algorithm, unlike MMSE, which requires tracking the nullspace. This leads to a reduction in complexity and all indications show that there will be little loss of performance since ZF with BICM has almost the same performance as MMSE with BICM [26]. In addition, the BICM approach does not require any ordering, which was a cause of performance loss in this work.

OFDM is a very effective technique against multipath distortion in wideband channels. The algorithm, developed in Chapter 4, can be adopted to work with OFDM. A straightforward but high complexity approach would use multiple copies of the algorithm - one for each sub-carrier. Alternatively, correlation between sub-carriers could be exploited to simplify or reduce the number of algorithm copies.

The algorithm in Chapter 4 can also be adjusted to work in high Doppler environments. The LMS algorithm, used for channel tracking, does not perform well in a fast changing environment. More powerful, high complexity tracking algorithm like RLS or Kalman could be employed to track fast channel variations.

Appendix: Realization of Exponent Difference

This appendix presents the algorithm that finds the exponent difference between two positive fixed-point numbers, $0 < A < 1$ and $0 < B < 1$. The output exponent difference 'dif' is given by $\text{dif} = \exp(B) - \exp(A)$ and evaluated in Figure A1.

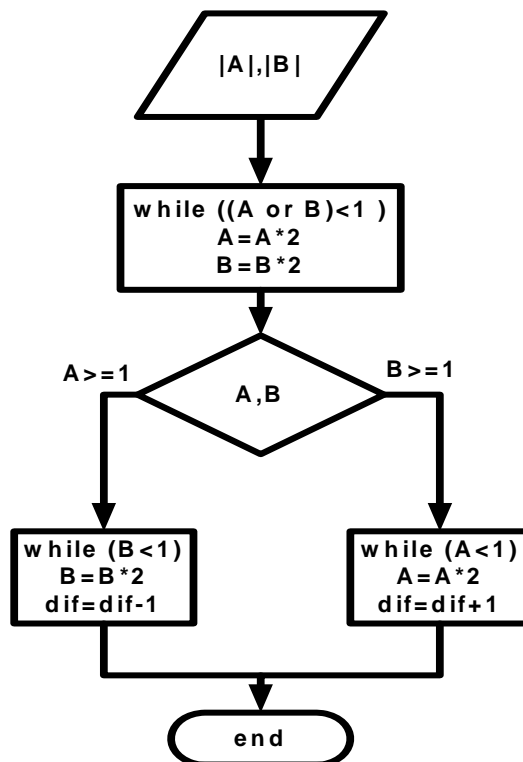


Figure A1 Algorithm that finds the exponent difference of two fixed-point numbers

Bibliography

- [1] Choi.J., Y. Heejung, and Y. H. Lee, "Adaptive MIMO decision feedback equalization for receivers in time varying channels," *IEEE Transactions on Signal Processing*, vol. 53, pp. 4295-4303, 2005.
- [2] P. Budde, "2006 Global Wireless Broadband - Moving into New Business Models," 2006.
- [3] S. Alamouti, "A simple transmit diversity technique for wireless communications," *IEEE journal on selected areas in communciations*, vol. 16, pp. 1451-1458, 1998.
- [4] T. S. Rappaport, *Wireless communications : principles and practice*, 2nd ed. Upper Saddle River, N.J.: Prentice Hall PTR, 2002.
- [5] B. Sklar, "Rayleigh Fading Channels in Mobile Digital Communication Systems Part I " *Communications Magazine*, vol. 35, pp. 90-100, 1997.
- [6] J. G. Proakis, *Digital communications*, 4th ed. Boston: McGraw-Hill, 2000.
- [7] P. Karttunen, K. Kalliola, T. Laakso, and P. Vainikainen, "Measurement analysis of spatial and temporal correlation in wideband radio channels with adaptive antenna array," in *International Conference on Universal Personal Communications* vol. 1, 1998, pp. 671-675.
- [8] K. F. Lee and D. B. Williams, "A space-frequency transmitter diversity technique for OFDM systems," presented at Global Telecommunications Conference, vol. 3, pp. 1473 - 1477, 2000
- [9] A. Papoulis and S. U. Pillai, "Entropy," in *Probability, random variables, and stochastic processes* 4th ed. Boston: McGraw-Hill, 2002, pp. 629-673.
- [10] T. M. Cover and J. A. Thomas, *Elements of information theory*. New York: Wiley, 1991.
- [11] C. Shannon, "A mathematical theory of communication," *The Bell System Technical Journal*, vol. 27, pp. 379-423, 1948.

- [12] D. Gesbert, M. Shafi, D.-s. Shiu, P. J. Smith, and A. Naguib, "From theory to practice: an overview of MIMO space-time coded wireless systems," *Journal on Selected Areas in Communications, IEEE* vol. 21, pp. 281-302, 2003.
- [13] Teltar.E, "Capacity of Multi-antenna Gaussian Channels," *European Transactions on Telecommunications*, vol. 10, pp. 585-595, 1999.
- [14] L. Grokop and D. Tse, "*Diversity/multiplexing tradeoff in ISI channels*," presented at International Symposium on Information Theory pp. 97, 2004
- [15] V. Tarokh, N. Seshadri, and A. R. Calderbank, "Space Time codes for high data rate wireless communication: performance criterion and code construction," *Transactions on Information Theory*, vol. 44, pp. 744-765, 1998.
- [16] 3GPP, "Group Services and System Aspects; 3GPP Systems to Wireless Local Area Network (WLAN) Interworking; System Description (Release 6)," *TS 23.234. v1.10.0*, 2003.
- [17] B. Lathi, *Modern Digital and Analog Communications systems*, third ed: Oxford press 1998.
- [18] ARRL, *The ARRL handbook for radio communications: The ARRL*, 2004.
- [19] P. Wilkinson, "Log-Polar signal processing," Ericsson, Ed. Sweden, 2001.
- [20] C. Shi, *Data Converters for Wireless Standards: Kluwer Academic Publishers*, 2001.
- [21] E. Ifeachor, *Digital Signal Processing, a practical approach: Addison-Wesley*, 1999.
- [22] V. e. a. Erceg, IEEE 802.11-03/940r4 "TGn Channel Models," 2004.
- [23] Kermoal.J.P, L. Schumacher, K. I. Pedersen, P. E. Mogensen, and F. Frederiksen, "A stochastic MIMO radio channel model with experimental validation," *Selected Areas in Communciations*, vol. 20, pp. 1211-1226, 2002.
- [24] A. J. Paulraj, D. A. Gore, R. U. Nabar, and H. Bolcskei, "An overview of MIMO communications - a key to gigabit wireless," *Proceedings of the IEEE* vol. 92, pp. 198 - 218 2004.
- [25] M. R. McKay and I. B. Collings, "Capacity and performance of MIMO-BICM with zero-forcing receivers," *IEEE Transactions on Communications* vol. 53, pp. 74 - 83 2005.
- [26] M. R. McKay and I. B. Collings, "*Performance bounds for MIMO bit-interleaved coded modulation with zero-forcing receivers*," presented at IEEE Global Telecommunications Conference, 2004
- [27] M. R. Mckay and I. B. Collings, "*Layered space-frequency bit-interleaved coded modulation for MIMO systems*," presented at IEEE 16th International Symposium on Personal, Indoor and Mobile Radio Communications, 2005

- [28] Hassibi.B, "An efficient square-root algorithm for BLAST," *Acoustics, Speech, and Signal Processing*, vol. 2, 2000.
- [29] K. Honjo and T. Ohtsuki, "*Computational complexity reduction of MLD based on SINR in MIMO spatial multiplexing systems*," presented at IEEE Vehicular Technology Conference 2004
- [30] Z. Luo, J. Liu, M. Zhao, B. Tang, and Y. Liu, "*Semi-blind MMSE detection for downlink MIMO-OFDM-CDMA systems*," presented at IEEE International Symposium on Communications and Information Technology 2005
- [31] E. Viterbo and J. Boutros, "A universal lattice code decoder for fading channels," *IEEE Transactions on Information Theory* vol. 45, pp. 1639 - 1642 1999.
- [32] B. Hassibi and H. Vikalo, "*On the expected complexity of sphere decoding*," presented at Asilomar Conference on Signals, Systems and Computers, vol. 2, pp. 1051-1055, 2001
- [33] U. Fincke and M. Pohst, "Improved vectors for calculating vectors of short length in a lattice including a complexity analysis," *Mathematics of Computation*, vol. 44, pp. 463-471, 1985.
- [34] O. Damen, A. Chkeif, and J.-C. Belfiore, "Lattice code decoder for space-time codes," *IEEE Communications Letters* vol. 4, pp. 161 - 163, 2000.
- [35] W. Xu, Y. Wang, Z. Zhou, and J. Wang, "*A computationally efficient exact ML sphere decoder*," presented at IEEE Global Telecommunications Conference vol. 4, pp. 2594-2598, 2004
- [36] Y. Xie, C. N. Georghiades, and Q. Li, "*A novel low complexity detector for MIMO system*," presented at Conference Record of the Thirty-Eighth Asilomar Conference on Signals, Systems and Computers 2004
- [37] V. Poor, "Multiuser detection," in *Advances in Statistical Signal Processing*, vol. 2: JAI Press 1993, pp. 369-409.
- [38] P. Wolniansky, Foschini, G, "V-Blast: An architecture for Realizing Very High Data Rates Over the Rich Scattering Wireless Channel," *Proceedings ISSE*, 1998.
- [39] J. Wubben and R. Bohnke, "*Efficient Algorithm for Detecting Layered Space-Time Codes*," presented at ITG, pp. 399-405, 2002
- [40] Bohnke.R, "Reduced complexity MMSE detection for BLAST architectures," *Global Telecommunications Conference*, vol. 4, pp. 2258-2262, 2003.
- [41] D. Watkins, "Fundamentals of matrix computations ". New York: Wiley, 1991, pp. 136-145.
- [42] B. Hassibi and B. M. Hochwald, "How much training is needed in multiple-antenna wireless links?," *IEEE Transactions on Information Theory*, vol. 49, pp. 951-963, 2003.

- [43] Q. Sun, D. C. Cox, and A. Lozano, "Training-based channel estimation for continuous flat fading BLAST" in *ICC*, 2002.
- [44] S. Yiu, R. Schober, and W. Gerstacker, "*Optimization of delay diversity for decision-feedback equalization*," presented at Personal, Indoor and Mobile Radio Communications, vol. 1, pp. 68-72, 2004
- [45] P. K. Shukla and L. F. Turner, "Channel-estimation-based adaptive DFE for fading multipath radiochannels," in *Communications, Speech and Vision*, vol. 138, 1991.
- [46] R. D. Lai-U Choi Murch, "A pre-BLAST-DFE technique for the downlink of frequency-selective fading MIMO channels," *IEEE Transactions on Communications* vol. 52, pp. 737-743, 2004.
- [47] W. Jiang, Y. Asai, T. Onizawa, and S. Aikawa, "*Fast Algorithm for Decision Feedback Equalization in Multiple Input Multiple Output Channel*," presented at Vehicular Technology Conference, vol. 5, pp. 2423-2428, 2006
- [48] J. Gomes and V. Barroso, "*MIMO decision-feedback equalization with direct channel estimation*," presented at Workshop on Signal Processing Advances in Wireless Communications pp. 419-423, 2004
- [49] Ginis.G, "Blind adaptive MIMO decision feedback equalization using Givens rotations," *ICC*, vol. 1, pp. 59-63, 2002.
- [50] S. A. Fechtel and H. Meyr, "*An investigation of channel estimation and equalization techniques for moderately rapid fading HF-channels*," presented at ICC, vol. 2, pp. 768-772, 1991
- [51] C. Komninakis, C. Fraquoli, A. H. Sayed, and R. D. Wesel, "Multi-input multi-output fading channel tracking and equalization using Kalman estimation," *IEEE Transactions on Signal Processing*, vol. 50, pp. 1065-1076, 2002.
- [52] N. Al-Dhahir and A. H. Sayed, "The finite-length multi-input multi-output MMSE-DFE," *IEEE Transactions on Signal Processing* vol. 48, pp. 2921 - 2936 2000.
- [53] G. Ginis and J. M. Cioffi, "On the relation between V-BLAST and the GDFE" *Communications Letters, IEEE*, vol. 5, pp. 364-366, 2001.
- [54] S. Kay, *Fundamentals of Statistical Signal Processing, Volume I: Estimation Theory* Prentice Hall PTR, 1993.
- [55] Roman.T, "Time domain method for tracking dispersive channels in MIMO OFDM systems," *ICASSP*, vol. 4, pp. IV-393-396, 2003.

- [56] Tong.J, "An adaptive channel tracking method for MIMO-OFDM systems," *ICCCAS*, vol. 1, pp. 354-358, 2004.
- [57] Zia.A, "Channel identification and tracking using alternating projections," *Statistical Signal Processing*, pp. 430-433, 2003.
- [58] A. Zia, J. P. Reilly, and S. Shirani, "An information geometric approach to channel identification," presented at IEEE International Conference on Acoustics, Speech, and Signal Processing, vol. 4, pp. 877-880, 2004
- [59] Schafhuber.D, "Kalman tracking of time varying channels in wireless MIMO-OFDM systems," *Signals, Systems and Computers*, vol. 2, pp. 1261-1265, 2003.
- [60] Oberli.C, "Maximum likelihood tracking algorithms for MIMO-OFDM," *Communications*, vol. 4, pp. 2468-2472, 2004.
- [61] K. Huber and S. Haykin, "Application of particle filters to MIMO wireless communications," presented at IEEE International Conference on Communications vol. 4, pp. 2311-2315, 2003
- [62] J. Du and Y. Li, "MIMO-OFDM channel estimation based on subspace tracking," presented at Vehicular Technology Conference vol. 2, pp. 1084-1088, 2003
- [63] W. H. Chin, D. B. Ward, and A. G. Constantinides, "Semi-blind MIMO channel tracking using auxiliary particle filtering," presented at IEEE Global Telecommunications Conference, vol. 1, pp. 322-325, 2002
- [64] C. H. Aldana and J. M. Cioffi, "Channel tracking for multiple input, single output systems using EM algorithm " presented at IEEE International Conference on Communications vol. 2, pp. 586-590, 2001
- [65] K. Deng, Q. Yin, and Y. Meng, "Blind symbol detection for multiple-input multiple-output systems via particle filtering," presented at IEEE International Conference on Acoustics, Speech, and Signal Processing, vol. 3, pp. 1041-1044, 2005
- [66] D. Zheng-Cong, T. Bin, and L. Ke, "MIMO time-varying channel tracking using annealed particle filtering," presented at International Conference on Communications, Circuits and Systems, vol. 1, pp. 219-222, 2005
- [67] B. Widrow and S. Stearns, *Adaptive Signal Processing* Prentice-Hall, Inc, 1985.
- [68] M. H. Dawid.H, "CORDIC Algorithms and Architectures," in *Digital Signal Processing for Multimedia Systems*, N. T. Parhi.K.K, Ed.: Marcel Dekker, 1999, pp. 623-655.
- [69] Gotze.J, "An Iterative Version of the QRD for Adaptive RLS Filtering " in *International Conference on Advanced Signal Processing*, 1994.

- [70] Gotze.J, "An efficient Jacobi-like algorithm for parallel eigenvalue computation," *Transactions on Computers*, vol. 42, pp. 1058-1065, 1993.
- [71] Dickson.K, "QRD and SVD processor design based on an approximate rotations algorithm," *SIPS, Signal Processing Systems*, pp. 42-47, 2004.
- [72] L. Gor and M. Faulkner, "*Power Reduction through Upper Triangular Matrix Tracking in QR Detection MIMO Receivers*," presented at Vehicular Technology Conference, Montreal, Canada, pp. 1-5, 2006